Three-dimensional Organization of Mineralized and Unmineralized Bone Tissues with Respect to the Lacuno-Canalicular Network Studied by Focused Ion Beam-Scanning Electron Microscopic Tomography

Vorgelegt von

M. Sc.

Mahdi Ayoubi

ORCID: 0000-0001-5359-3442

von der Fakultät III - Werkstoffwissenschaften und –technologien

der Technischen Universität Berlin

Zur Erlangung des akademischen Grades

Doktor der Ingenieurwissenschaften (Dr.-Ing.)

genehmigte Dissertation

Promotionsausschuss:

Vorsitzender: Prof. Dr. Dietmar Auhl

Gutachter: Prof. Dr. Peter Fratzl

Gutachterin: Prof. Dr. Claudia Fleck

Tag der wissenschaftlichen Aussprache: 17.09.2020

Berlin 2020

Acknowledgments

To begin, I would like to say that it was a great opportunity to spend a few years of my life holding this research position (2017-2020), which was generously funded by the Max Planck Institute of Colloids and Interfaces (MPICI). I am extremely grateful for the financial support and assistance in making my project come to life.

I would like to express my deepest gratitude to my advisor Prof. Dr. Peter Fratzl, for giving me the chance to do my Ph.D. under his supervision and for his continuous support and trust throughout the research. His immense knowledge, vision, motivation, and inspiring discussions provided me with new perspectives to develop my project step by step. I whole-heartedly appreciate him for giving me the encouragement, and for sharing insightful suggestions. Every meeting with him was a milestone in the completion of this project. Nevertheless, I do not have enough words to express my sincere feeling about his outstanding moral and scientific character.

I wish to express my profound gratitude to my supervisor Dr. Luca Bertinetti who guided me well throughout my research work, from the very beginning in data acquisition to the analysis of the results, especially with his expertise in electron microscopy. His scientific guidance, motivation, understanding, and patience gave me more energy and positive emotions in order for myself to excel in the research. I highly appreciate the independence he gave me to work in my own style, while at the same time, he was always available for scientific and technical discussions. His support also guided me to rectify numerous things that led to this dissertation.

Special thanks are given to Dr. Andreas Roschger for enlightening me in the beginnings of my research project with his precious scientific knowledge in bone, for endless constructive scientific discussions, and for his insightful comments. I specifically appreciate his extensive, valuable and professional feedback, and his provision. He played a major role in polishing my research writing skills. I am deeply grateful to him for doing his best to put me always on the right track.

I am particularly indebted to Alexander van Tol for his assistance with data analysis and image processing, as well as for the plentiful scientific discussions we had together. I would like to give credit to him for his excellent programming and analytical skills. His help and support throughout the challenges I encountered, made it possible to complete tasks before deadlines. I very much enjoyed the time we spent together in conferences, seminars, and workshops. Altogether, Alex was my “Scientific brother” who was always open to provide any help needed.

Conducting the academic study regarding such an interdisciplinary topic could not be as simple as the people mentioned above made for me. It would not have been possible to conduct this research without their precious support and professional expertise. Therefore, I am deeply indebted to all of them for their invaluable advice and intimate collaboration that gave me the confidence to attempt the impossible.

I would like to extend thanks to my supervisor at the Technical University of Berlin, Prof. Dr. Claudia Fleck, for the kind support and supervision throughout my Ph.D. In addition, I would like to thank Dr. Richard Weinkamer for the fruitful scientific meetings and discussions. Furthermore, special thanks are given to my colleagues, Dr. Zhaoyong Zou and Dr. Sanja Sviben, for numerous scientific discussions and for assistance with data acquisition, which was always performed with wide smiles.

My sincere thanks go to Dr. Mason Dean, Dr. Tengteng Tang, Dr. Daniel Chevrier, Dr. Hajar Razi, and Dr. Cathleen Oschatz for reviewing and proofreading my dissertation and giving me great remarks to finalize it. Their efforts really mean a lot to me.

I would like to pay my special regards to Prof. Dr. Paul Roschger from the Ludwig Boltzmann Institute and Prof. Dr. Andrea Berzlanovich from the Medical University of Vienna for providing the samples for this study, and I would like to thank the helpful technicians in MPICI, Heike Runge, Birgit Schonert, and Gabriele Wienskol, who assisted me in the preparation of samples for measurement.

I owe sincere thanks to Berlin-Brandenburg School for Regenerative Therapies (BSRT), in particular my supervisor at BSRT, Prof. Dr. George Duda, and Dr. Sabine Bartosch who gave me the opportunity to join the school that provided precious annual mentoring meetings, workshops, seminars, and courses. It also provided a great atmosphere for me to discuss with many researchers, which has opened a new window for me to be able to pursue my future career in regenerative medicine.

I am indebted to my friends with whom I had a great honor and pleasure of working during this research project, who made the work more enjoyable for me. I would also like to appreciate every member of the biomaterials department of MPICI for providing a friendly and scientific environment, and for the invaluable assistance during my study.

Last but not least, I would like to thank my parents who have always supported me spiritually and financially so that I only paid attention to the studies and achieving my objective without any obstacle throughout my life. They also gave me substantial motivation, encouragement, and moral support to accomplish my personal and scientific goals. Finally, I owe a huge debt of gratitude to my wife for her infinite support, love, and patience. I wish to give special thanks for her understanding and empathy during the last seven years of mutual life.

Kurzfassung

Knochen ist ein Nanokomposit-Biomaterial, das aus karbonisierten Hydroxylapatit-Nanokristallen und Kollagenfasern besteht. Es unterliegt ständigen Umwandlungsprozessen, um eine Struktur zu erhalten die optimiert ist den zyklischen mechanischen Belastungen standzuhalten und zur Mineralhomöostase beizutragen. Es wird angenommen, dass dieser Prozess von Osteozyten gesteuert wird, die die Knochenmatrix mit ihrem dichten Lacuno-canalicular Netzwerk (LCN) durchdringen. Das hohe Verhältnis von Oberfläche zu Volumen und die Fähigkeit, Mineralvorstufen zu transportieren und Proteine abzusondern, deuten zudem auf eine entscheidende Rolle dieses Netzwerks bei dem Mineralisierungsprozess hin. Für das Verständnis dieses Mineralisierungsprozesses sind daher Materialcharakterisierungen auf der Micro- und Nanoskala unter Berücksichtigung von biologischen/zellulären Aspekten entscheidend. Dies ist nur mit neuesten bildgebenden 3D Methoden möglich, die sowohl eine hohe Auflösung aufweisen sowie große Messregionen abbilden können.

Ziel dieser Studie war es, die Wechselwirkung des LCN und dem sich bildenden Knochengewebe zu untersuchen, um neue Erkenntnisse über das frühe Stadium der Mineralisierung im neugebildeten kortikalen Knochen zu gewinnen. Zunächst wurde ein Jod-Färbeprotokoll zur Untersuchung der nichtmineralisierten Matrix unter Verwendung von Umwelt-Rasterelektronenmikroskopie (ESEM) erstellt und weiter optimiert hinsichtlich der Einwirkzeit und der Menge an Jod. Zudem wurde konfokale Laser-Scanning-Mikroskopie (CLSM) verwendet, um eine 3D-Visualisierung des LCNs in geringer Vergrößerung darzustellen und Bereiche, in denen das LCN an die mineralisierende Matrix grenzt, zu identifizieren. Anschließend wurden hochauflösende Bilder dieser Regionen mit fokussierter Ionenstrahl-Rasterelektronenmikroskopie (FIB-SEM) erzeugt, um die Mineralisierung in der Nähe des LCNs sichtbar zu machen. Darüber hinaus wurden Analysewerkzeuge entwickelt, um die Korrelation zwischen Mineralisierungsgrad und Entfernung zum LCN zu ermitteln.

Die Beobachtungen und Analysen von den Oberschenkelschaften dreier Frauen ergaben, dass in allen neun untersuchten sich bildenden Osteonen, eine Mineralisationsfront an der Grenzfläche von nichtmineralisiertem und mineralisiertem Gewebe mit einer Breite von ~3.67 µm existiert. Diese Front besteht aus Mineralisierungsherden von nur ~50 nm Größe, die sich in einer charakteristischen Distanz zum Havers-Kanal bilden und mit fortschreitender Mineralisierung allmählich wachsen. Dies zeigte sich daran, dass mit steigender Entfernung zum Havers-Kanal immer größere Mineralisierungsherde gefunden wurden. Relativ zur Distanz zum nächsten Canaliculus war Größe und Grad der Mineralisierung allerdings nahezu konstant. In allen FIB-SEM Messungen konnte zudem ein dichtes LCN in der nicht-mineralisierten Matrix gefunden werden, welches von einer Seite mit dem Havers-Kanal verbunden ist und auf der anderen

Seite in die mineralisierte Matrix reicht. Überraschenderweise wurde an der Mineralisationsfront eine Region um die Canaliculi beobachtet, welche keine Mineralien enthält und erst mit Verzögerung mineralisiert.

Auf der Basis der beschriebenen Resultate wird die Hypothese aufgestellt, dass das LCN zusammen mit sekrierten nicht-Kollagenen Proteinen oder Proteoglykanen die als lokale Mineralisationsinhibitoren fungieren, eine entscheidende Rolle im Mineralisationsprozess spielt. Möglicherweise geschieht dies in der frühen Mineralisationsphase in der das LCN als Transportweg von Mineralisationsvorstufen oder Ionen zur Mineralisationsfront genutzt wird wodurch dort die Ionenkonzentration erhöht und so der Mineralisierungsprozess eingeleitet wird.

Zusammenfassend kann gesagt werden, dass unter Verwendung von 3D-Elektronenmikroskopie in Kombination mit einer optimierten Färbeprozedur und einer neu entwickelten Auswertesoftware neue Einblicke in die Mineralisierung während der Knochenbildung gewonnen wurden. Die Resultate tragen dazu bei bisher unbekannte Aspekte des intensiv diskutierten Mineralisierungsprozesses und der Rolle der Osteozyten darin aufzudecken.

Abstract

Bone is a nanocomposite biomaterial consisting of carbonated hydroxyapatite nanocrystals and collagen fibrils. It is regularly remodeled to keep the integrity of its well-organized structure to endure cyclic mechanical loads and contribute to mineral homeostasis. This remodeling process is thought to be orchestrated by osteocytes that pervade the bone matrix with their dense lacuno-canalicular network (LCN). The LCN might also play a critical role in the mineralization process thanks to its high surface to volume ratio and its ability for the transport of mineral precursors and protein secretion. However, this process is still poorly understood since it also involves the biological/cellular compartment and happens at both the micro- and nanoscale. Hence, only a few techniques can achieve 3D imaging with high enough resolution and large enough fields of view.

The aim of this work was to investigate the interaction of the LCN and the forming bone tissue to gain new insights into early-stage mineralization of human remodeled cortical bone. First, an iodine staining protocol was established to observe the unmineralized matrix. Next, it was optimized by adjusting the amount of iodine and staining time, and by checking the stained matrix using environmental scanning electron microscopy (ESEM). Confocal laser scanning microscopy (CLSM) was utilized to image large fields of view for 3D visualization of the LCN. This technique enabled the selection of regions of interest (ROIs), where an LCN exists at the mineralizing matrix. Afterward, focused ion beam-scanning electron microscopy (FIB-SEM) was employed to obtain high-resolution 3D image stacks of the selected ROIs and to visualize mineralization with respect to the LCN. Furthermore, an analytical tool was developed to provide a correlation between the degree of mineralization and the distance to the LCN.

After investigating post mortem samples from the femoral midshaft from three women exhibiting forming osteons, observations and analyses revealed that at the interface of unmineralized and mineralized matrices, a mineralization front characterized by a ~3.67 µm width exists. This front is composed of mineralization foci as small as ~50 nm, which form at a specific distance from the Haversian canal and gradually grow through the mineralization process. Therefore, an increase in the foci size was observed from the Haversian canal toward the mineralized matrix. However, the foci size, as well as the mineralization degree of foci, was almost constant with distance from the canaliculi. It was also found that in all FIB-SEM datasets, a dense LCN exists in the unmineralized matrix, which is connected to the Haversian canal from one side and extended to the mineralized matrix from the other side. Surprisingly, a free-of-mineral halo zone around the canaliculi was observed at the mineralization front that shrinks with the course of mineralization.

One hypothesis, which is formulated from results herein, is that the LCN potentially plays a crucial role in the mineralization, which might happen simultaneously with the secretion of non-collagenous proteins

(NCPs) or proteoglycans that locally inhibit mineralization. A possible scenario under which this can happen is that at the early stage of mineralization, the LCN is used to transport mineral precursors or ions to the mineralization front and increase the ion concentrations in the unmineralized matrix to facilitate mineralization.

In conclusion, the 3D electron microscopy approach combined with an optimized staining procedure and an in-house developed analytical tool revealed novel insight into the mineralization process with respect to the LCN. The observed mineral distribution suggests new hypotheses on the role of the osteocytes in the mineralization process.

Contents

Chapter 1

Introduction

For over three centuries, bone has been carefully studied to understand the relationship between its structure and properties [1]. Thanks to this long history, it is known that bone is a hierarchically structured nanobiomaterial [2] and provides various functions such as locomotion of the body, protection of the organs, and calcium homeostasis regulation. [3]. Some of these roles are due to its unique mechanical properties, which originate from a combination of collagenous matrix and minerals [4]. Bone is also a dynamic material since it is regularly remodeled to keep its integrity by removing microcracks created because of the cyclic loads [5]. In the remodeling process, old bone is resorbed by osteoclasts, and the new bone is deposited by osteoblasts [6]. The newly deposited bone (osteoid) is later mineralized to provide the desired mechanical properties and also to store the minerals for further uses in the body [3]. Remodeling also aids mineral homeostasis by releasing calcium and phosphate ions into the body fluid when it is needed for the other metabolic pathways in the body [3].

Bone is tissue and, as such, it accommodates cells that are fundamental to the material itself imparting properties such as self-healing and self-adaptation. [7]. Among all the cells found in bone, osteocytes are the most abundant ones, which are connected by the cell processes located inside small canals called canaliculi (~200-400 nm in diameter [8]). Recent studies show that osteocytes play different roles such as orchestration of bone remodeling, mechanosensing, and, most likely, they are involved in the mineralization process by directly interacting with the bone matrix to provide mineral homeostasis [6]. The osteocytes form a lacuno-canalicular network (LCN) with a density of 74 km/cm^3 in human osteons [9]) pervading the bone matrix and exhibiting a surface of ~215 m^2 in the human body [10]. Taking advantage of the high density and the large surface area, the osteocyte network potentially plays a pivotal role in the transportation of the mineral precursors [11]. The various purposes of osteocyte function and their collective interactions emphasize the role of bone as a highly dynamic and adaptive endocrine organ as well as a nanocomposite for mechanical support.

At the final stages of bone remodeling, i.e. after osteoid is deposited, the unmineralized collagenous matrix is mineralized. Mineralization is the process in which nanocrystals of carbonated hydroxyapatite ($Ca_{10}(PO_4)_6(OH)_2$) are formed from their ionic precursors found in the body fluid [12]. The plate-like minerals, with a maximum size of ~$7\times80\times200$ nm^3 [13], are deposited in the intrafibrillar and interfibrillar sites of collagen in the presence of non-collagenous proteins (NCPs) [14]. Hydroxyapatite crystals, however, do not precipitate directly from ions. It has been shown that, at first, precursor phases such as a polymer-induced liquid precursor (PILP) phase or amorphous calcium phosphate (ACP) are formed [15]. Afterward, these phases might undergo phase transformations to octacalcium phosphate ($Ca_8H_2(PO_4)_6.5H_2O$) and then to hydroxyapatite. It has been proposed that following these transformations, the activation energy barrier to hydroxyapatite is smaller than for its direct precipitation [16].

During bone remodeling, mineralization happens in a highly organized manner that starts with a fast primary stage in which bone reaches 70% of its mineral content in a few days, followed by a slow secondary stage where bone matures in a time scale of years [17]. The mechanisms underlying the primary stage of mineralization are still unclear and therefore are, to date, still highly debated. Mainly, this is because their investigation requires advanced imaging and sample preparation techniques that are needed to track the occurrence and the phase transformation of the mineral. In particular, understanding of the correlation between cells and mineralization foci (~50-600 nm in diameter), which form and grow at this stage [18], can only be achievable with high-resolution 3D imaging methods that provide large enough fields of view. Moreover, the early stage of mineralization is a dynamic process that needs to be spatially investigated from the early osteoid deposition to the final maturation. Recently, with the advent of cryo-microscopy, new players have been identified (such as vesicles), which are believed to play a role in the transport and deposition of minerals in forming bone [19, 20]. However, as these works are mostly 2D or *in vitro* studies on animal models, the mineralization process in human bone is not well understood.

In order to address the challenges mentioned above, in the presented work, the extracellular matrix in the vicinity of the LCN was characterized in three-dimensions using focused ion beam serial sectioning combined with scanning electron microscopy (FIB-SEM) and confocal laser scanning microscopy (CLSM) as well as energy-dispersive X-ray spectroscopy (EDX). The high spatial resolution up to 40 nm in the FIB-SEM combined with the large field of view of CLSM of ~500 µm provided a promising correlative approach to combine information from different length scales. Besides, an iodine staining protocol was established to facilitate imaging of the LCN in unmineralized bone and increase the soft-tissue contrast in the backscattered electron images. Thanks to the stained unmineralized matrix, 3D datasets were obtained in which the unmineralized matrix, the mineralized matrix, and the osteocyte network could be visualized and therefore analyzed to reveal the interaction between cells and the bone tissue. Additionally, a method was developed to correlate the mineralization degree with the distance to the LCN. With these microscopic and analytical tools, this study aimed at gaining new insights into the role of the LCN in the early stage of mineralization, addressing the following questions: Where are the first mineralization foci formed in the mineralization process? What are the mechanisms that lead to a fully mineralized matrix? What is the role of the osteocyte network in these mineralization mechanisms?

Chapter 2

State of the Art

Bone is known as a composite material with a variety of functions and properties [7]. On the one hand, from the biological point of view, bone stores minerals, secretes growth factors, and produces hormones. On the other hand, from an engineering perspective, bone supports and protects soft and vital organs, such as heart, and allows locomotion of the whole body thanks to its excellent mechanical properties, including high stiffness and toughness [3]. It is generally agreed that these properties originate from its structure at different length scales, the so-called "hierarchical structure" [2]. At the macro-scale, some regions are exhibiting a sponge-like structure (i.e., trabecular bone) while others are compact (i.e., cortical bone). At the micro-scale, bone is composed of different building blocks like bone packets and osteons. At the nanoscale, collagen fibrils and mineral platelets are the building components (Fig. 2.1).

More recent studies on the structure of bone have centered at the micro- and nanoscales (especially the latter) by virtue of the advances in imaging and characterization techniques [21]. The microstructure of bone has been studied with different imaging techniques, such as quantitative backscattered electron imaging (qBEI), which has provided insight into the mineralization process of bone (i.e., primary and secondary mineralization stages) [17]. At the nanoscale, many studies focused on mineral precursors transport to the sites of mineralization and their subsequent deposition within collagen fibrils [20]. The modern techniques, such as focused ion beam-scanning electron microscopy (FIB-SEM) and nano-computed tomography (nano-CT) have made a substantial contribution to this area of research, e.g., 3D visualization of the osteocyte lacuno-canalicular network (LCN) and evaluation of mineralization degree [22, 23]. Moreover, sample preparation under cryogenic conditions followed by cryo-imaging has the advantage of analyzing the near-native structure of biological samples [24]. In particular, cryo-preparation of biomineralized tissues can preserve the amorphous mineral phase found in matrix vesicles (MVs). These amorphous minerals can easily become crystalized if conventional sample preparation is used [25]. Along with these techniques, novel staining protocols have been established to gain more information such as collagen fibril orientation and intra/interfibrillar mineralization [8, 26]. Moreover, as many of the new techniques provide "3D information" of bone structure, new image processing methods have been developed to analyze these types of data [27, 28].

In this chapter, first, the recent studies on the bone micro- and nano-structure with a specific focus on the mineralization will be reviewed (2.1-2.4). Afterward, advanced imaging techniques, which have been recently employed for investigation of biological tissues, such as bone, will be introduced (2.5).

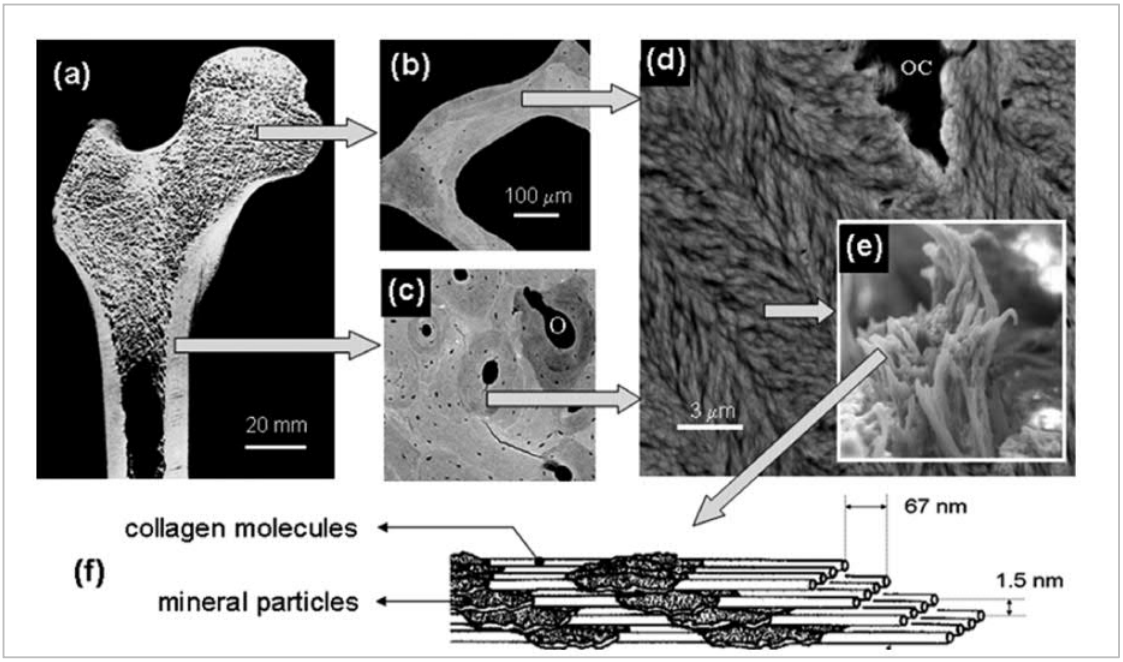

Fig. 2.1. Bone structure at various length scales. a) A longitudinal section of a proximal femur showing trabecular and cortical bone. b) and c), show the microstructure of these two types of bones, respectively. d) Backscattered electron image of a trabecula showing its lamellar structure. e) Electron microscopy image of mineralized collagen fibrils making a fibril bundle. f) Illustration of bone nanostructure showing collagen fibrils perfused with mineral particles made of hydroxyapatite. Reprinted with permission from [7].

2.1 Bone macro- and micro-structure, cells and remodeling

Bone has excellent mechanical properties, which derives directly from its structure [4]. While meeting the mechanical demand, trabecular bone keeps the overall weight of the skeleton as low as possible. In view of the orchestrated functions of different cells, bone is a dynamic biomaterial, which is always produced and maintained in a balanced manner [7]. In this regard, bone remodeling is the process in which bone renews itself not only to keep its mechanical properties but also to contribute to other biological processes such as mineral homeostasis [7]. Mineral homeostasis is particularly important because of the critical roles that calcium plays in the body, such as the transmission of nerve impulses, muscle contraction, and blood coagulation [3].

2.1.1 Cortical and trabecular bone

As it is visible to the naked eye (Fig. 2.1), bone is composed of two compartments with different architecture: cortical and trabecular bone. Cortical bone, with a dense microstructure and porosity of 6% [7], exhibits microchannels with 20-200 μm diameter as passageways for blood vessels and nerves. These canals are called Haversian canals, which are surrounded by layers of lamellae (together, they are called

osteons or Haversian systems) [3]. The lamellar architecture consists of a twisted plywood-like structure of collagen fibrils, which in turn toughens the bone by inhibiting crack propagation [29] and also enhances torsion resistance [3]. Another type of canal in this system, which is orientated at the right angle to the Haversian canal and connect the periosteum to the Haversian canal is Volkmann's canal [3] (Fig. 2.2). Trabecular bone, on the other hand, has a porous structure. Its porosity is usually more than 50% and is filled with marrow [30]. There are hardly any osteons in the trabecular bone, but it has its building blocks called bone packets [31]. Cells are present in the trabecular bone as well as the cortical bone to transport nutrients from the capillaries in the endosteum [3]. The trabeculae are believed to be aligned with the lines of external stress to optimally bear the load, which makes bone an adaptive material [7].

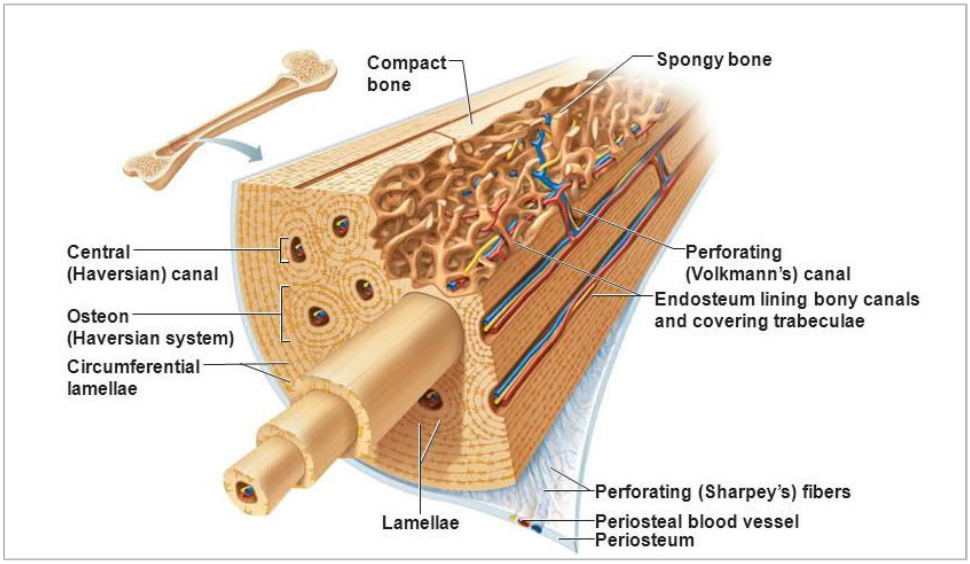

Fig. 2.2. Scheme of the microstructure of cortical and trabecular bone. Cortical bone is composed of osteons with Haversian canals that contain blood vessels and nerves. The trabecular core with high porosity is surrounded by the cortical shell and is in contact with endosteum and marrow. Adapted with permission from [3].

2.1.2 Bone cells

There are five different types of cells in bone with different functions: osteogenic cells, bone-lining cells, osteoblasts, osteocytes, and osteoclasts. Except for the osteoclasts, all cells are differentiated from mesenchymal stem cells (Fig. 2.3) [3]. Osteogenic (or osteoprogenitor) cells are mitotically active stem cells, which are found in flattened or squamous shape in growing bone, and some of them, differentiate to bone-lining cells or osteoblasts when stimulated [3]. Bone-lining cells, also called quiescent osteoblasts, are flat cells that exist at endosteum, periosteum, and blood channels. Bone linings cells can differentiate to osteoblasts when they are stimulated [32], and as well as other cells found on the non-remodeling bone

surface, form a “functional bone membrane” that controls ion exchange between the body and bone [33]. Osteoblasts are derived from mesenchymal stem cells and are responsible for the deposition of collagenous matrix and calcium-binding proteins [3]. Similar to fibroblasts and chondroblasts, osteoblasts are mitotically active cells. After the secretion of the matrix, some of the osteoblasts differentiate into bone lining cells or osteocytes. Otherwise, they undergo apoptosis (i.e., cell death). If osteoblasts became lining cells, they could differentiate back to osteoblasts [3]. Osteocytes are mature, dendritic cells which are located inside lacunae and are connected to each other with slender processes [6]. Cell processes occupy narrow canals with 200-300 nm diameter (i.e., canaliculi). Canaliculi are formed when osteoblasts become osteocytes and connect the cells to the Haversian canal [30]. During mineralization of the newly deposited bone matrix and maturation of cells, the projections, containing gap junctions of osteoblasts, elongate, and form canaliculi filled with fluid and cell processes [3]. Canaliculi provide communication between osteocytes and permit transportation of nutrients and wastes through a huge network as dense as 74 km/cm^3 of bone [9].

Osteoclasts, the multinucleated cells (Fig. 2.3), are derived from hematopoietic stem cells (the same stem cells that differentiate to macrophages). They are mobile cells; however, they are located at the resorption sites during bone resorption [3]. They exhibit a ruffled border in contact with bone, providing an increased surface area for enzymatic degradation of bone. Osteoclasts release hydrochloric acid to dissolve hydroxyapatite, and they secrete protease cathepsin K to break down collagen fibrils [34]. The debris of degradation (both organic and mineral) are packed in vesicles and dumped above the cells after passing through them [3, 30].

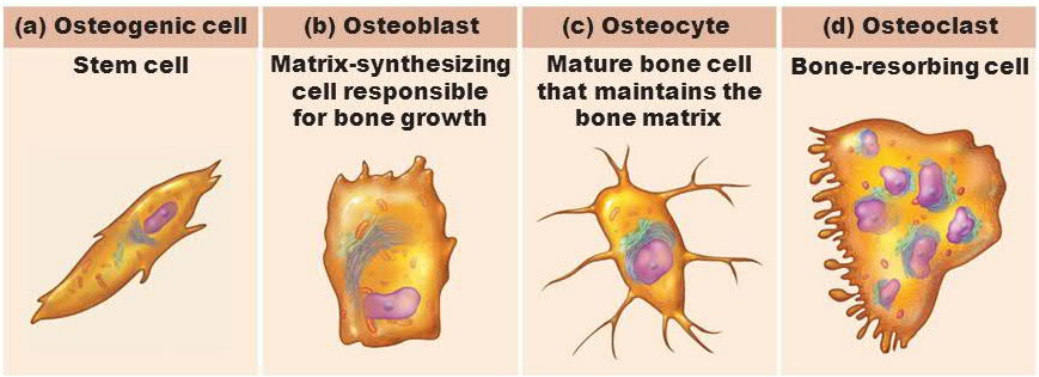

Fig. 2.3. Different types of cells that exist in bone. a) osteogenic cell, b) osteoblast, c) osteocyte, and d) osteoclast. Bone-lining cells are similar to the osteogenic cell in shape (not shown). Except for osteoclasts, which are derived from hematopoietic stem cells, all other cells are derived from mesenchymal stem cells. Reprinted with permission from [3].

2.1.3 Remodeling

Remodeling is the process in which bone is resorbed by osteoclasts, and new bone is formed by osteoblasts at both periosteal and endosteal surface as well as in osteons [31]. It is well accepted that remodeling is orchestrated by osteocytes, which produce receptor activator of RANKL and sclerostin to regulate differentiation of osteoclasts and osteoblasts [34]. In Haversian systems, the classic result of remodeling, resorption starts with forming a cutting cone by osteoclasts (Fig. 2.4.A) where they leave a cylindrical cavity with 200 μm diameter behind them [30]. Afterward, osteoblasts deposit an osteoid seam (an unmineralized collagen layer 10-12 μm wide) with a rate of 1 μm per day [30]. The osteoid seam is mineralized after maturation of the unmineralized matrix that takes about one week [3]. The calcifiable matrix deposited by osteoblasts contains, in addition to collagen, 10-15% of non-collagenous proteins (NCPs), including osteopontin, osteonectin, bone sialoprotein, and osteocalcin [35]. Following remodeling, osteoblasts become bone lining cells, osteocytes, or undergo apoptotic death [36, 37].

Remodeling does not happen homogeneously in bone. For instance, the distal part of the femur is replaced every five or six months while the shaft is substituted at a much lower rate [3]. In terms of trabecular and cortical bone, the former is replaced every three or four years, while the latter is altered about every ten years [3]. Bone must be remodeled to maintain its mechanical properties. Fatigue microcracks, which are formed in bone because of excessive loading cycles, are removed during remodeling [5].

Remodeling is controlled by hormonal loops and mechanical stress [3]. In the case of hormonal control, parathyroid hormone (PTH) is released when calcium concentration in the blood is low. PTH can stimulate osteoclasts to resorb bone and raise the calcium concentration back to the range of 9-11 mg per 100 ml [3]. With this control mechanism, the body seemingly does not consider the mechanical properties of bone. Osteoclasts resorb both new and old bone, and if calcium concentration in blood is too low, excessive resorption occurs, and large holes form in bone [3]. However, mechanical stress helps to guide the PTH to locate osteoclasts in low-stressed zones. One mechanism for the control of remodeling with mechanical stress might be electrical signaling as compressed and stretched regions are oppositely charged. Another mechanism is the detection of fluid flow within the canaliculi that provide stimuli for remodeling (see section 2.2.3) [38]. In general, hormonal feedback loops control whether and when remodeling is needed while mechanical stress determines where remodeling should happen.

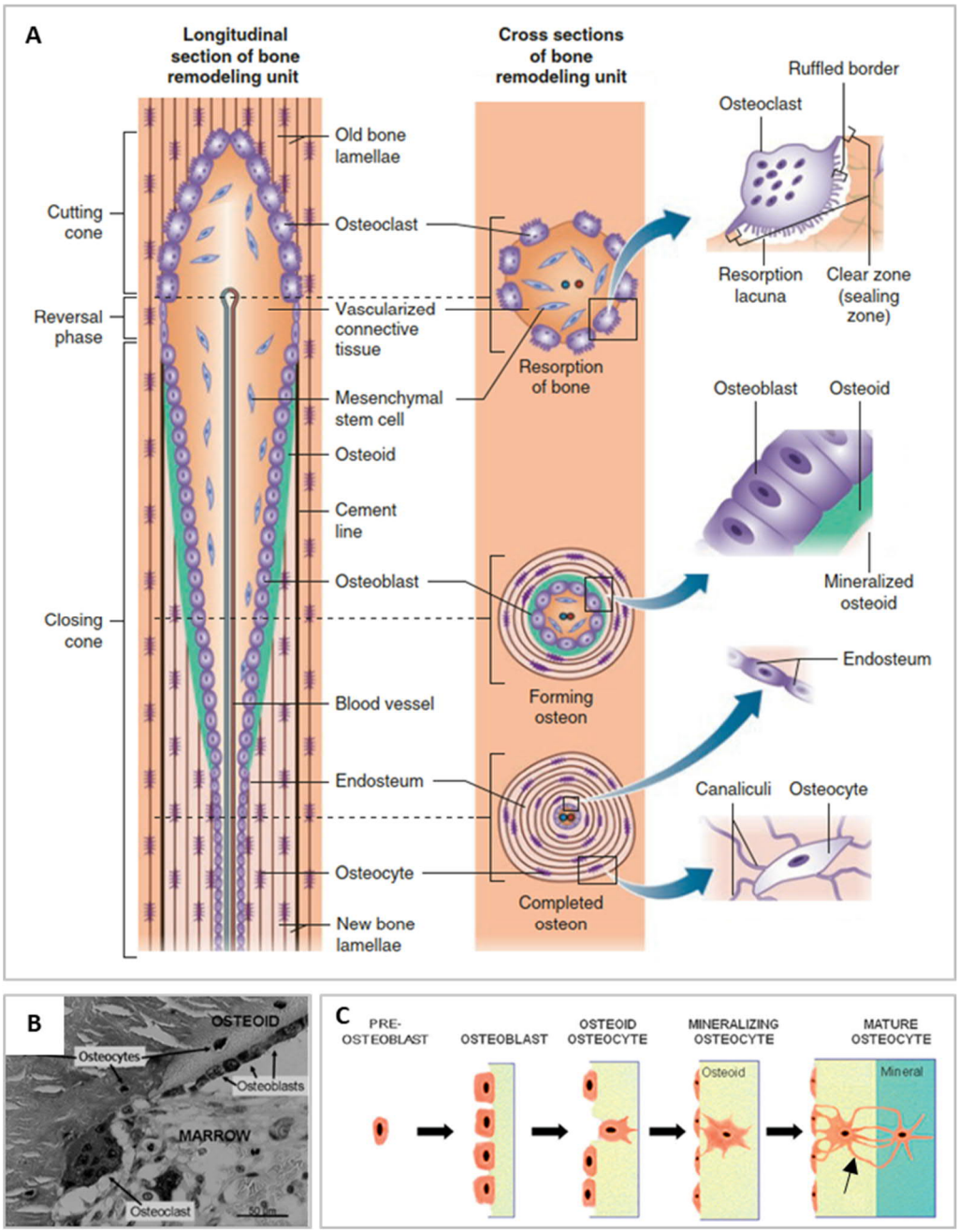

Fig. 2.4. A) Scheme of the Haversian system remodeling. Osteoclasts start resorption followed by bone deposition by osteoblasts. Reprinted with permission from [39]. B) Light micrograph of bone remodeling. The multi-nucleus osteoclasts resorb old bone, and afterward, osteoblasts deposit new matrix (osteoid). Osteoid is an unmineralized bone that is mineralized in a few weeks after deposition. Reprinted with permission from [7]. C) Differentiation of osteoblasts. Some of the osteoblasts differentiate into osteocytes buried within the osteoid. The osteocytes keep in contact with other cells with their slender processes passing through the canaliculi (the black arrow). Adapted with permission from [6].

2.2 Bone at the nanoscale

Studies of bone at the microscopic level have revealed some structure-function relationships [4]. More recently, it was discovered that some amazing properties of bone, such as high toughness and stiffness, are attributed to bone structure at the nanoscale [29]. Recent studies, with the help of advanced imaging techniques and novel sample preparation routines, have provided new insights into bone structure at the nanoscale. The main components at this scale are collagen fibrils (with the gap zone of 40 nm wide where minerals can nucleate) [13], mineral particles (~7×80×200 nm^3 in size) [13], osteocyte network (with canaliculi which are ~200-400 nm in diameter) [8, 9], and non-collagenous proteins (with a molecular weight of a few kDa), all of which play critical roles in bone mineralization [14].

2.2.1 Collagen

Collagen is a fibrous protein that provides various mechanical functions in the human body [40, 41]. Based on the structure and molecular organization, collagen is categorized into 28 types [42]. A novel type of collagen was discovered and called collagen type XXIX (type 29), but it has been shown that its gene is identical to the collagen type VI [43]. Five types of collagen, namely collagen types I, II, III, V, and XI, which are all fibrillar, form 80-90% of human collagen [44]. Among all, collagen type I is the most abundant one and typically found in bone, dentin, tendon, and skin. It has some significant mechanical properties, such as viscoelastic strength, torsional stiffness, and load-bearing capacity [45]. Collagen type I is composed of three procollagen chains (two α1 and one α2), which are folded to form a triple helix that contains about 1000 amino acids per each chain [45]. The chains contain a $(Gly\text{-}X\text{-}Y)_n$ repeating pattern, in which every third residue in each chain is glycine (Gly), and the other two residues are often proline (in X-position) and hydroxyproline (in Y-position) [40]. Glycine exists in all types of collagen, while the other two residues can vary in different types of collagen. In collagen type I, glycine residue is located in the center of the helix, followed by proline and hydroxyproline, which are at the surface of the helix and determine the functionality of the collagen, such as its rigidity [13]. Proline and hydroxyproline are secondary amines, and in addition, they contain a nitrogen atom that covalently binds the side chain to the backbone of the polypeptide (Fig. 2.5.A). The rings of the polypeptide chain reduce rotation of the side chain and limit the formation of hydrogen bonds that lead to the creation of an inflexible polypeptide [30].

The helical assembly of the collagen molecule is stabilized by the formation of hydrogen bonds between chains. For this, two criteria should be fulfilled [46]. First, the three chains must be shifted (~2.9 Å in the direction of the helical axis) by one residue with respect to each other. Second, every third residue in each chain must be located near the common helical axis to provide close packing of the three chains. This

second criterion explains why glycine exists in every third residue in each chain. The correct sequence of residues in the chains is so critical that a mutation in collagen molecules can cause severe diseases, such as osteogenesis imperfecta. The most common cause of this disease is the replacement of one glycine by another amino acid that interrupts the $(Gly\text{-}X\text{-}Y)_n$ repeating pattern and results in defective mineralization [47].

The *in vivo* synthesis of collagen is a complex, multistep process [47]. First, procollagen, which is the precursor form of collagen, is synthesized at the endoplasmic reticulum membrane. Procollagen contains N and C-terminal propeptides that prevent premature fibril assembly of collagen molecules. Second, collagen undergoes post-translational modifications in which hydroxylation of residues occur and disulfide bond forms. The next key step in collagen formation is the folding of the procollagen chains, in which the chains self-assemble into the triple helical structure. The folding nucleates at the C-terminus of the chain, and it is completed by cleavage of propeptides that prepare the collagen molecules to form collagen fibrils extracellularly. The telopeptides, which are located at the N- and C-termini of the triple helix, aid the assembly of the molecule and formation of covalent crosslinks [43, 47].

The extracellular attachment of the collagen molecules leads to the staggered packing of collagen fibrils introduced by Petruska *et al.* [48]. This packing occurs because two succeeding collagen molecules are located with a 40 nm distance between each other in a fibril, and they are staggered with respect to their neighboring molecules of 67 nm, i.e. D-period in the wet collagen (Fig. 2.5.B) [13]. The result of this stagger is the periodic gap ($G \approx 40$ nm) and overlap ($O \approx 27$ nm) regions where the former has 20% less packing density than the latter [43]. The D-period is reported to change to 64 nm in the dry collagen indicating the role of water in the collagen structure [40].

Besides collagen type I, which forms 95% of all collagen types in bone, collagen types II, III, VI, X, and XXVII are also found in bone [45]. Collagen types II and X were found at the growth plate and were suggested to be involved in bone formation, but they are mostly found in cartilage [49]. Collagen type III forms fibrils, which are less ordered and thinner in comparison to type I. Moreover, Collagen type III is always found in combination with other types of collagen [45]. Collagen type VI is a microfibrillar collagen that seemingly lines the matrix surrounding the osteocytes and the canaliculi [50]. Collagen type XXVII was also found in the transition from cartilage to bone, which might play a role in this transition [51].

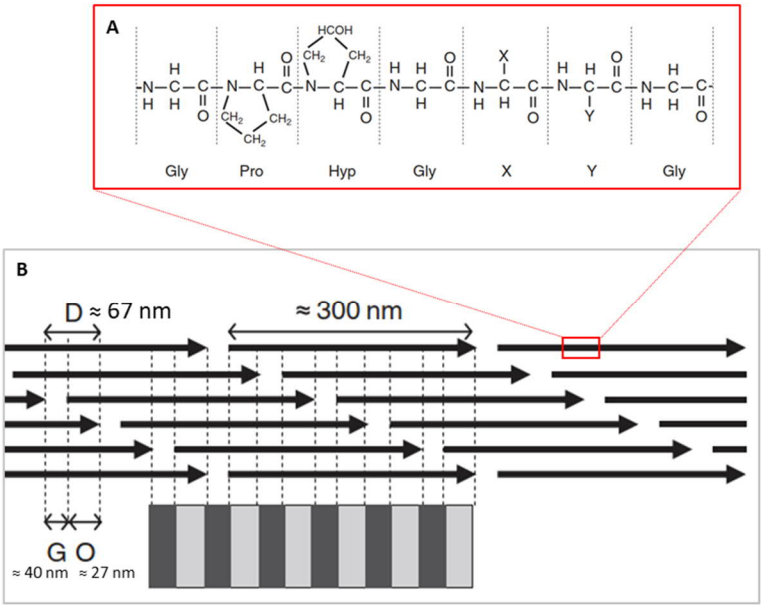

Fig. 2.5. A) A section of one procollagen chain containing three amino acids (glycine, proline, and hydroxyproline in collagen type I) that repeats and produces a triple helix molecule of collagen. B) Staggered packing of collagen fibrils introduced by Petruska *et al.* [48] that shows the banding pattern of overlap (O) and gap (G) regions. Adapted with permission from [13].

2.2.2 Minerals

Minerals are generally defined as the inorganic materials found both in geological and biological environments [52]. In the mineralized tissues of many vertebrates, minerals are calcium phosphate in the form of carbonated hydroxyapatite with the general formula of $Ca_{10-x}H_x(PO_4, CO_3)(OH)_{2-x}$ [12, 13]. The carbonated hydroxyapatite crystals, which are formed within collagen fibrils (Fig. 2.6), are among the smallest crystals found in biological tissues [13]. It is mostly agreed that they are plate-like shape, and their thickness, length, and width vary in the ranges of 2-7 nm, 15-200 nm, and 10-80 nm, respectively [13]. Their impurity and small size, which provides a high surface area to volume ratio, make them highly reactive [53]. After nucleation, bone mineral crystals seem to grow mainly in two dimensions (length and width and not thickness) to produce sword-shaped blades [30]. Minerals are crystalized in hexagonal unit cells, and their C-axis are aligned with collagen fibrils long axis in mineralization [54]. They are the main source of calcium in the human body, which contains 1.2-1.4 kg of calcium, more than 99% of which is found in bone minerals [3]. In vertebrates, different types of tissue exhibit a different content of mineral. The typical amount of minerals (%wt.) found in these tissues is as follows: enamel 95%, dentin 67%, fibrillar cementum 45-50%, and bone 60% [14]. Minerals are also composed of amorphous calcium phosphate (ACP) [55]. It has been observed that in the bone of zebrafish fin rays, ACP transforms into the crystalline phase within the collagen matrix [56]. Although ACP is generally known as a transient phase, there are indications that it exists in the mature bone as a hydrophilic coating on the carbonated hydroxyapatite crystals [57]. The interaction between minerals and collagen molecules is still not fully

understood, but van der Waals forces and ionic bonding might play a prominent role [30]. Electrostatic interactions between cationic and anionic sites are suggested as powerful interactions that can direct bond formation between mineral and collagen. Water has also been suggested to play a role in stabilizing the hydroxyapatite lattice and to couple the mineral crystals with the matrix. In general, it is widely accepted that there is a tight bonding between mineral and collagen [40].

In comparison to geological hydroxyapatite, the minerals found in bone are impure [58]. This is mainly due to the many ionic substitutions that can occur in biological apatite, which can happen at the calcium, phosphate, and hydroxide sites. The substitutions for calcium can be trivalent cations (such as rare element earth elements and actinides), other bivalent cations (such as magnesium), and monovalent cations (such as sodium and potassium). It has been reported that bone minerals contain a lower amount of calcium than stoichiometric hydroxyapatite, which can be explained by the presence of vacancy defects found in the place of calcium, as well as by the presence of substitute ions [59]. For phosphate substitution, tetravalent, trivalent, and bivalent ions are possible, and for hydroxide substitution, monovalent or bivalent ions are likely to replace the hydroxide ions [16].

The main substitute ion in hydroxyapatite crystals is carbonate. Crystals typically contain 4-8% carbonate, which replaces hydroxide (type-A carbonated apatite) or phosphates (type-B carbonated apatite) in the lattice sites [16] (especially near the vascular and marrow space [30]). The ratio of type-A to type-B is in the range of 0.7-0.9 [60], and older tissues represent a higher ratio. *In vitro* and *in vivo* tests have shown that the presence of type-B carbonate in the apatite lattice increases the solubility and decreases the crystallinity of mineral [61]. Type-A carbonated apatite has been reported to have a lower affinity for the osteoblasts in comparison to hydroxyapatite, which is the result of the decrease in the polar component of the surface of type-A carbonated apatite [62]. A third site has also been identified for carbonate ions, which is the hydrated surface layer of crystals [60]. The carbonate content has been studied by Raman spectroscopy, and it was observed that it depends on the type of tissue and increases from enamel to dentin and bone [63].

Hydrogen phosphate ions were also found in the phosphate sites. It has been shown that the presence of hydrogen phosphate and type-B carbonate in the phosphate site corresponds to calcium-deficient apatite, which is because of the maintenance of the electrical charge balance [16]. For instance, the substitution of one phosphate ion by a hydrogen phosphate ion or a carbonate ion can be compensated with the removal of one calcium ion and one hydroxide ion. Hydroxide ions are among the major ions in the stoichiometric apatite; however, its content in biological apatite is controversial, and it has been reported to vary between a few percents to 50% of the stoichiometric apatite hydroxide content [64]. This discrepancy has been attributed to the internal hydrolysis of water molecules that can increase hydroxide content [16]. It has also

been suggested that the hydroxide content decreases when the crystal strain increases, and the crystal size decreases [65]. It should be noted that bone mineral composition is affected by tissue aging. For instance, in the early stages of mineral formation, the hydrogen phosphate content is high, and the carbonate content is very low. This leads to a deficiency of calcium in the mineral [16]. However, by aging, the type-A carbonate content increases [66] that can cause an increase in calcium content to fulfill the charge balance.

In addition to calcium, phosphate, and carbonate (major ions), some of the typical ions found in biological apatite are as follows: magnesium, sodium (minor ions), fluoride, strontium, zinc, and lead (trace ions) [16, 67]. Minor and trace ions can also have significant effects on minerals. Magnesium has been reported to stabilize the hydrated layer of the minerals and retard the apatite domains formation [16]. It is also known that magnesium ions act as the stabilizer of the transient phases, such as amorphous calcium phosphate [68]. Sodium is another minor ion which has been found in minerals of periosteal and osteonal regions of bone. It has been observed that its concentration increases with the maturation of minerals, which might be accompanied by the substitution of type-B carbonate [69]. Fluoride is the most abundant trace ion, with a concentration between 0.05-0.1%. A higher amount of fluoride (above 0.3%) can cause fluorosis disease and bone fragility [70]. Fluoride ions decrease the apatite solubility, and they are found not to be easily eliminated from the mineral (half-life of about 20 years). Strontium, another trace ion, which is incorporated into the crystal during growth [71] (unlike ions such as magnesium which remains in the hydrated layer), has been found to increase the solubility of the mineral [16]. In general, the effect of different ions on the solubility of minerals is important as it can affect the recycling rate of ions [16].

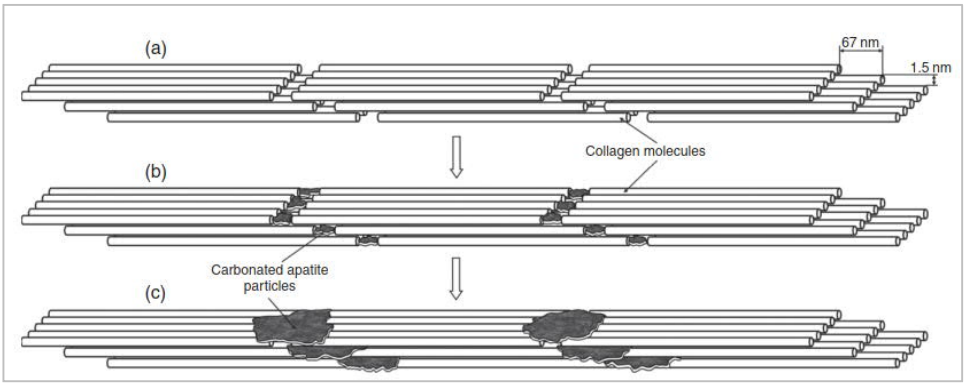

Fig. 2.6. Scheme of mineral crystals and their location within the collagen fibrils. The image shows the nucleation and growth of minerals in the gap zones of the fibrils. Reprinted with permission from [13].

2.2.3 Osteocyte network

Osteocytes constitute 90-95% of bone cells and form a dense network connected by dendritic processes [6] (Fig. 2.7). Using this network with great accessibility to the matrix [72], osteocytes have several functions such as mechanosensitivity [9], mineral transport [73], endocrine signaling [36], and mineral homeostasis [74]. In the context of mechanosensitivity, osteocytes respond to mechanical strains by sending resorption or formation signals [75]. There are several ways available for osteocytes to receive mechanical stimuli, including local matrix deformation, fluid flow shear stress, and electrical streaming potentials resulting from the flow of ions on the charged lacuno-canalicular walls [36]. Fluid flow in the LCN is determined initially by extravascular pressure and is altered by the mechanical stress on bone. It is suggested that the osteocyte itself, osteocyte processes, and hair-like projections (it is also called primary cilia at the time of differentiation) can be responsible for sensing the mechanical stimuli. Adhesion molecules, such as CD44, actin-bundling protein fibrin, and integrin that bind osteocytes and their processes to the LCN, also contribute to amplifying and sensing the mechanical stimuli. The mechanical signals are then transduced to biological output, like intercellular calcium increase that leads to the release of nitric oxide (NO), ATP, and prostaglandins [36].

One direct result of mechanosensitivity is the orchestration of bone remodeling that can be affected by both mechanical and hormonal signals [3]. There are several models describing the mechanosensitivity of the osteocytes. For instance, in bone resorption, one possible way of signaling by osteocytes is the expression of RANKL, which is primarily secreted by osteoblasts, along osteocytes processes to stimulate osteoclasts [6]. Another significant pathway is suggested to be osteocyte apoptosis. At sites of microcracks, osteocytes express pro-apoptotic molecules to mark the region for osteoclasts [76]. Interestingly, anti-apoptotic molecules are expressed further away from other osteocytes to protect from apoptosis. This path is a programmed cell death that can lead to resorption of bone in the desired regions. However, other conditions that cause not-programmed osteocyte death will lead to unnecessary resorption of bone where it is not desirable and causes pathological conditions, such as osteoporosis [6]. At sites of fracture damage, osteocytes are reported to secrete osteopontin, which may induce the migration of mesenchymal stem cells to form new bone [77].

Another function of the osteocyte network is osteocytic osteolysis that can contribute to mineral homeostasis besides bone remodeling [74, 78]. Thanks to the high surface to volume ratio of the LCN (400 fold higher than Haversian and Volkmann system), small changes in the mineral content of the perilacunar/canalicular matrix will cause substantial differences in the total amount of minerals released or absorbed in the body [74]. For instance, during lactation in a mouse model, a high amount of calcium is needed, and it is shown that the osteocytes can alter their perilacunar spaces to mobilize calcium and

phosphate to the fluid [36]. The osteocyte network can communicate with osteoclasts, which are a potential source of H+ ion for bone resorption [34]. The activity of tartrate-resistant acid phosphatase (TRAP), an osteoclast specific gene, was also observed in the osteocytes that causes resorption of the matrix in perilacunar regions [36].

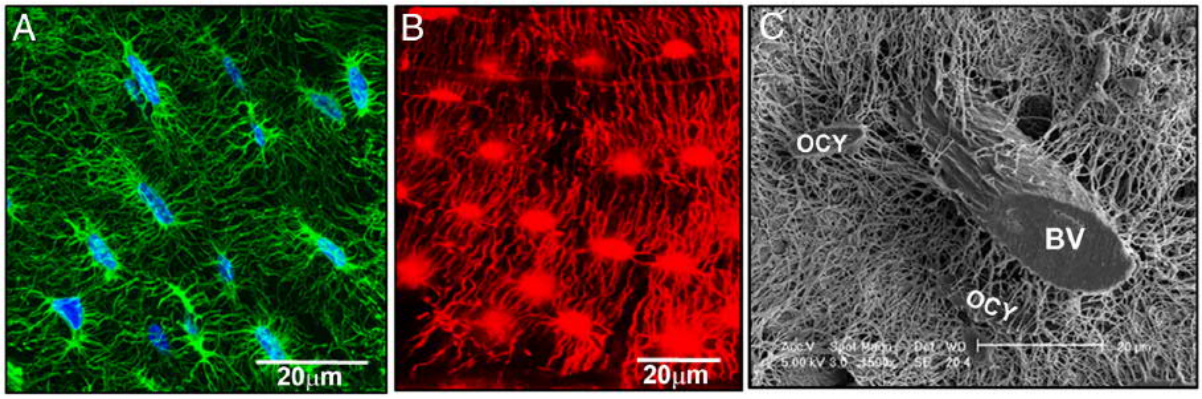

Fig. 2.7. Osteocyte network morphology. A) Confocal fluorescence image obtained with Alexa Fluor 488 phalloidin staining, visualizing osteocytes in the cortex of a mouse femur. B) Confocal fluorescence image of the osteocyte lacuno-canalicular network (LCN) acquired with procion red staining, demonstrating the dense network connecting osteocytes in mouse cortical bone. C) Scanning electron microscopy image of acid-etched mouse bone, showing the interconnection between osteocytes (OCY) and a blood vessel (BV). Reprinted with permission from [36].

2.2.4 Non-collagenous proteins (NCPs) and proteoglycans

Collagen is the major protein in bone (85-90 wt.%) [2]. The other proteins found in bone are called non-collagenous proteins (NCPs). They are known for the initiation and inhibition of mineralization, as well as for mineral-collagen binding [30]. Because of the charged carboxyl groups of their aspartic acid and glutamic acid residues, they have a high affinity for calcium ions [79]. Some of the NCPs are circulating proteins and exist in other places than bone [30]. The dominant group of NCPs, which are acidic and highly phosphorylated, are called small integrin-binding ligand N-glycosylation (SIBLING) proteins [80]. Dentin matrix protein 1 (DMP1), osteopontin, and bone sialoprotein are some examples of SIBLINGs that play crucial roles in bone mineralization. Non-SIBLING proteins, such as osteocalcin and osteonectin, are also crucial in mineralization, and their absence can cause alteration in bone geometry and reduction of bone mass [79]. Proteoglycans are other essential NCPs as they play a mechanical role in bone along with collagen [81]. Together with collagen, proteoglycans are the main components of the organic part of the matrix (osteoid) [3]. Proteoglycans are composed of a core protein and one or more sulfated glycosaminoglycan chains, comprising 5-7% of NCPs [82]. They are the major components of the material

surrounding osteocyte processes and might act as the tethering elements in canaliculi [83]. Moreover, glycosaminoglycan is a negatively charged chain, which might attract calcium ions. In contrast, phosphate ions are observed to be localized to collagen fibrils [84]. Therefore, it is suggested that proteoglycans can regulate the localization of ions in the supersaturated non-mineralized sites [84].

2.3 Mineralization of bone at the micro- and nanoscale

Mineralization of bone is the process in which hydroxyapatite crystals are formed within the collagenous matrix [53]. At the microscale, mineralization follows matrix deposition, where new packets of bone are formed (Fig. 2.8.A). This process happens in two steps, known as primary and secondary stages of mineralization. In the primary mineralization phase, about 70% of the total mineral content of bone is deposited within a few days, while the second stage takes months to deposit the remaining 30% of minerals [85, 86]. A well-known approach for the quantification of mineralization at the microscale is obtaining the bone mineral density distribution (BMDD). The BMDD graph is obtained from quantitative backscattered electron imaging (qBEI) that provides information such as calcium content frequency of the matrix [17]. With the BMDD, the kinetics of mineralization can also be extracted that is usually referred to as mineralization law. Fig. 2.8.B shows a typical BMDD graph of a healthy individual.

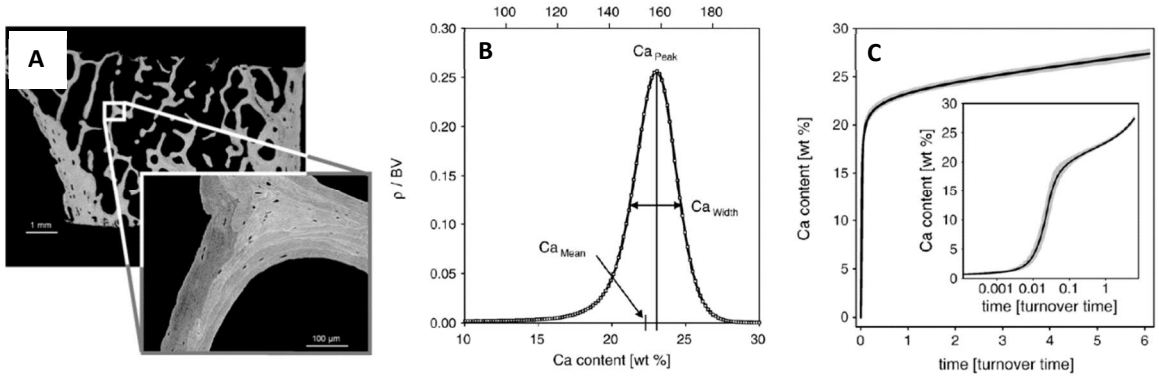

Fig. 2.8. A) Backscattered electron image of cortical and trabecular bone. The enlarged image shows individual bone packets that compose the trabecular bone. B) Corresponding BMDD graph, which reveals that calcium content for healthy individuals is between 0 to 30 weight percent regardless of age, sex, and ethnicity. C) The mineralization law that describes how mineral content changes with time at the early stage of mineralization. Adapted with permission from [85].

At the nanoscale and in vertebrates, mineralization starts with a nucleation phase, which is followed by a growth phase where ions are taken up from blood serum [87]. In bone, the vasculature is connected to capillaries, such as the Haversian canal and the LCN that can carry mineral precursors. Afterward, transport and deposition of minerals can happen by either cell-controlled or cell-independent routes [20]. At the mineralization sites, the tightly regulated interaction between many components, such as cells, NCPs, and collagen, leads to deposition of nano-sized minerals at specific sites, most likely in the gap regions of collagen within a relatively short time [14]. Abnormalities in each step of biomineralization can cause severe diseases, such as rickets and osteogenesis imperfecta. Moreover, it can cause ectopic (pathological) mineralization of soft tissues such as kidney and artery [88].

2.3.1 Thermodynamics and phase transformations in mineralization

In the classical models of mineralization, crystallization of hydroxyapatite can happen when calcium and phosphate ions are concentrated in a medium. In other words, when the ionic product of calcium and phosphate reaches a certain level, crystals are formed [84], which happens via nucleation and growth processes [87]. From a thermodynamic point of view, in the case of homogeneous nucleation, two opposing mechanisms play roles in the nucleation and growth of the minerals; the creation of a new surface that is accompanied by an increase in the free energy and the formation of the new clusters that decreases the free energy. By summing up these contributions, the total free energy associated with the formation of mineral particles is obtained (red curve in Fig. 2.9). The surface free energy is defined by $6\alpha n^{2/3}$ in which α is the interfacial energy per particle, and n is the number of the particles in the cluster. μ is the chemical potential per particle. The apex of the plot shows the energy barrier (ΔG^*) for nucleation of a new crystal, which is overcome by the accumulation of n^* of precursors. Therefore, a supersaturated solution is needed to provide a local accumulation of ions and further nucleation of crystals [87].

Mineralization can proceed through intermediate stages and not directly happen with nucleation and growth of hydroxyapatite crystals. These intermediate stages are critical in the biological environment as the energy barrier of nucleation must be overcome [16]. Amorphous phases were recently proposed as putative alternatives to the crystalline phases for the formation of minerals from liquid precursors since they are more soluble at equilibrium [89]. One intermediate phase that is vastly studied in mineralized tissues is amorphous calcium phosphate (ACP). ACP is more soluble than hydroxyapatite [15] and is similar to a dense liquid [90].

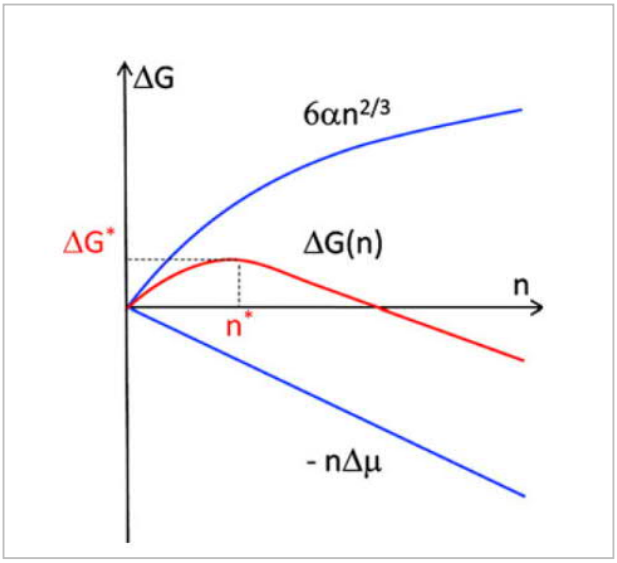

Fig. 2.9. Free energy of crystallization. The upper blue curve shows the change of the surface energy of the newly formed crystal, which is unfavorable because it contributes to increasing the total free energy. The lower blue line shows the change in the chemical potential of the crystal, which is favorable because it contributes to decreasing the total free energy, considering the negative sign. The red curve, which is the sum of the two blue curves, shows the changes in the total free energy of the crystal as a function of crystal size (n). n^* is the critical size of the crystal at which the nucleus is stable, and growth will happen spontaneously afterward. Reprinted with permission from [87].

ACP is not stable with conventional sample preparation methods and is prepared under cryo-conditions for cryo-electron microscopy [19]. ACP formation was observed in enamel prior to the crystallization of hydroxyapatite [91]. In a study of zebra fish bone, ACP was observed in the nanosphere subparticles [56]. *In vitro* studies showed stabilized ACP by NCPs like fetuin, osteopontin, and amelogenin [56]. Another transition phase proposed to form before crystallization of hydroxyapatite is octacalcium phosphate (OCP) [92]. OCP has a unit cell of $Ca_8H_2(PO_4)_6.5H_2O$ and is involved in apatite bone formation [93]. OCP is thermodynamically less stable than hydroxyapatite but shares a similar crystallographic plane. It is suggested that OCP is a transient precursor for the homogeneous nucleation of hydroxyapatite [94].

A recently discovered transient phase that can be formed before ACP in a complex fluid found in bone, where NCPs exist in addition to water, is the highly-hydrated polymer-induced liquid precursor (PILP) phase [15] (2.10.a). Because of the large hydration layer (formed by either protein-bound or bulk water that exists in bone), a pre-nucleation phase can be seen as a dense liquid [87]. A polymer like polyaspartic acid sodium salt (amorphous precursor) can induce PILP formation because of the negatively charged acidic residues that can sequester ions in a supersaturated solution [95]. In bone, positively charged regions at collagen can be utilized for infiltration and charge-charge interaction of the PILP phase [96]. Dey *et al.* observed the formation of PILP prenucleation clusters before ACP in simulated body fluid stabilized in the absence of a nucleation-inducing surface [97]. It is suggested that the homogeneous formation of prenucleation clusters (probably by PILP) may promote mineralization in addition to the heterogeneous nucleation that happens with the help of collagen or proteins [90]. In the case of collagen, gap zones with positive net charge close to the C-terminal end of molecules are proposed as nucleation sites. For the protein

case, it can be assisted by SIBLINGs family of NCPs like bone sialoprotein, osteopontin, and dentin phosphoryne, which will produce denser packing of clusters [26, 87].

Fig. 2.10 shows PILP-assisted mineralization in which liquid precursors form first, translocate to the sites of nucleation, and transform to ACP, OCP, and hydroxyapatite. As it is shown, the intermediate phase transformation favors faster kinetics, thanks to the steps with smaller energy barriers [16]. After successful nucleation, the growth of minerals can occur through ion absorption either from the extrafibrillar region or from the charged amino acid residues at the intrafibrillar sites [98]. In the following sections, different mineralization pathways through which the phases mentioned above can form will be reviewed.

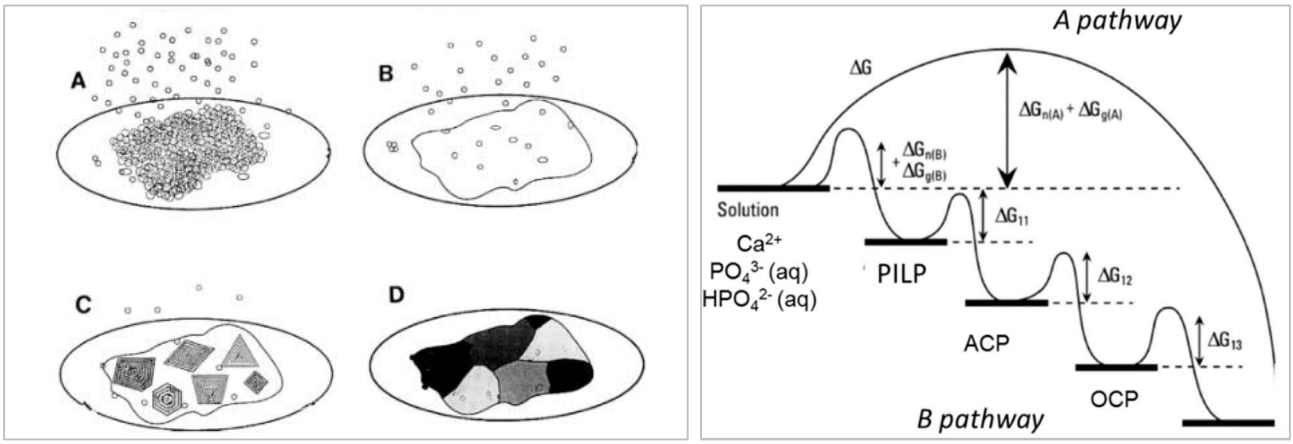

Fig. 2.10. Scheme of the PILP stages that shows accumulation, coalescence, nucleation, and growth of minerals (left image). Reprinted with permission from [15]. Classical mineralization (A pathway) in comparison to multistep mineralization (B pathway). PILP, ACP, and OCP are transitional stages that can reduce energy barriers for phase transformation (right image). Adapted with permission from [16].

2.3.2 Cell-controlled mineralization

Mineralization begins with the uptake of mineral precursors from an ion source. For invertebrates, such as foraminifera and sea urchin, the ion source is an aqueous medium like seawater, while for most of the vertebrates, this source is blood serum that contains calcium and phosphate ions obtained from digested food [19, 99]. Endocytosis is the mechanism by which invertebrates concentrate and sort ions and transport them to the sites of mineralization (Fig. 2.11.A). Other pathways are ion channels and pumps of cells that can transport mineral ions to the mineralization front [100, 101]. Mineral transport in the vasculature can be risky for body health and may cause ectopic mineralization. The reason is that high amounts of mineral should be transported while the solubility of bone mineral is too low [53]. On the other hand, the toxicity of free calcium ions is an issue if minerals are transported through cells [14, 53]. Therefore, cells limit

cytoplasmic calcium concentration as low as 0.1 μM, while calcium concentration in blood is ~1 mM. Phosphate concentration in the cell is five mM, but because of the low concentration of calcium, no mineralization occurs inside the cell [102].

Thus, transport of minerals can be performed with two strategies: vesicle and ion transport. A cryo-imaging study on chicken embryos revealed that membrane-bound vesicles containing mineral precursors are found in the blood vessels produced by unknown cells [103]. The vesicles contribute to the massive transport of mineral precursors to the desired sites (e.g., in rapid bone formation), and they also decrease the danger of ectopic mineralization. Another way to reduce the risk of ectopic mineralization is the action of mineralization inhibitors, such as fetuin, matrix gla protein, and osteopontin [24, 53]. The vesicles are also considered as storage containers of minerals that can reduce the toxicity of calcium for cells. Similar vesicles and mineral particles without membrane both at formation and resorption sites were also found in chicken embryo forming bone [24]. It is suggested that ions are sequestered with endocytosis by cells and translocated through the cell by vesicles and further to the extracellular matrix [25] (Fig. 2.11.A).

Translocation of mineral precursors from vesicles to the extracellular matrix was confirmed in two studies [20, 56]. With cryo-imaging of forming zebrafish bone, Mahamid *et al.* found that submicron-sized packages of ACP nanospheres were translocated to the collagen matrix and started to crystalize there [56]. During the transformation, the shape of particles changes from spherical to the platelet. It was also observed that the crystals were smaller than vesicles. This distinction in size suggests that either vesicle is composed of smaller sub-particles, or it is disaggregated in order to penetrate the collagen fibril bundles [24]. In another study on the mouse osteoblasts, which was conducted *in vitro*, Boonrungsiman *et al.* observed intracellular vesicles that transport minerals to the extracellular matrix. With high-pressure freezing and freeze substitution preservation of ACP, they found that mitochondrial granules, as small as 50 nm, store calcium and phosphate, and transfer them to the vesicles [20]. Mitochondria were also found to deliver calcium and phosphate via MVs to the matrix. Lehninger [87] proposed that mitochondria accumulate ions from plasma so that the ions concentration exceeds the solubility product, and eventually, micro-packets of tricalcium phosphate are formed. The diffusion of ions happens as cytoplasm has much lower ion concentration (~0.1 μM) than plasma. Accumulation occurs by pumping of ions on specific carriers in response to the electrochemical gradient. The formation of micro-packets continues in an ATP-dependent process. Transport of micro-packets to the extracellular matrix was proposed to happen either directly or after dissociation [104] (Fig. 2.11.B). Exocytosis is also suggested as a translocation pathway of minerals [105]. In any way, minerals might finally be extruded from the MVs into the collagen matrix and nucleate there [54].

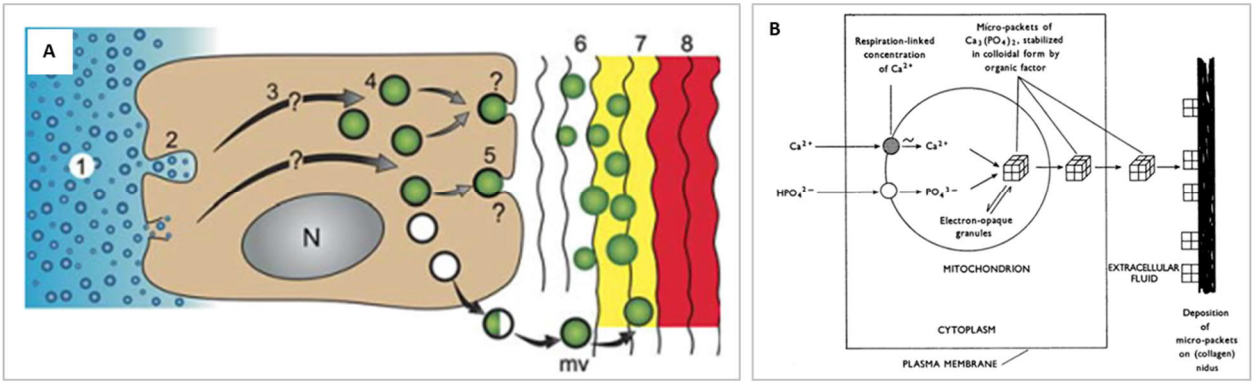

Fig. 2.11. A) The process in which minerals are transported from body fluid (1) to the matrix. The ions are trapped inside the cell with endocytosis (2) and transported within the cell to specialized vesicles (3) where the first disordered mineral phase is produced (4). Afterward, mineral-bearing vesicles are transported to the matrix, or matrix vesicles (MVs) are produced in the cell and accumulate ions in the extracellular matrix (5). Then, the disordered phase is translocated to the mineralization front (6) and transforms into a crystalline phase (7). Finally, the matrix is fully mineralized (8). Reprinted with permission from [25]. B) The mechanism by which ions are accumulated in mitochondria to be transported to the matrix in micro-packets. Reprinted with permission from [104].

There are several mechanisms for initial mineralization within vesicles (Fig. 2.12). MV can be budded from the plasma membrane of the cell [35, 88, 106], and Annexin, located on the surface of MV, can pass calcium into the MV. Alkaline phosphatase on the surface of MV liberates phosphate by cleaving polyphosphate, and afterward, Na+/pi co-transporter delivers phosphate to MVs. Pit 1,2 transporters are also suggested to transport phosphate into vesicles [102]. Calcium and phosphate ions accumulate inside MV and interact with phospholipids to form nanocrystals [102]. When the crystals grow to a specific size, they might rupture the membrane of the vesicle to deposit within collagen fibrils. An alternative suggested mechanism is the formation of ACP in the acidic intracellular vesicles [88]. Alkaline phosphatase is located inside the vesicle, but it has low activity due to low pH. Therefore, a sufficient amount of phosphate is not released inside the vesicles, and ACP will be stable until the intracellular vesicles fuse with the plasma membrane. After fusion, ACP is secreted into the collagen matrix, and alkaline phosphatase is exposed to the extracellular matrix with higher pH, which consequently becomes activated, and liberates more phosphate. This mechanism will lead to the formation of HA in the collagen [88]. In the turkey leg tendon, it was observed that collagen mineralization follows vesicles mineralization. Vesicle's minerals are soluble and can increase the ion product in the collagen environment [107].

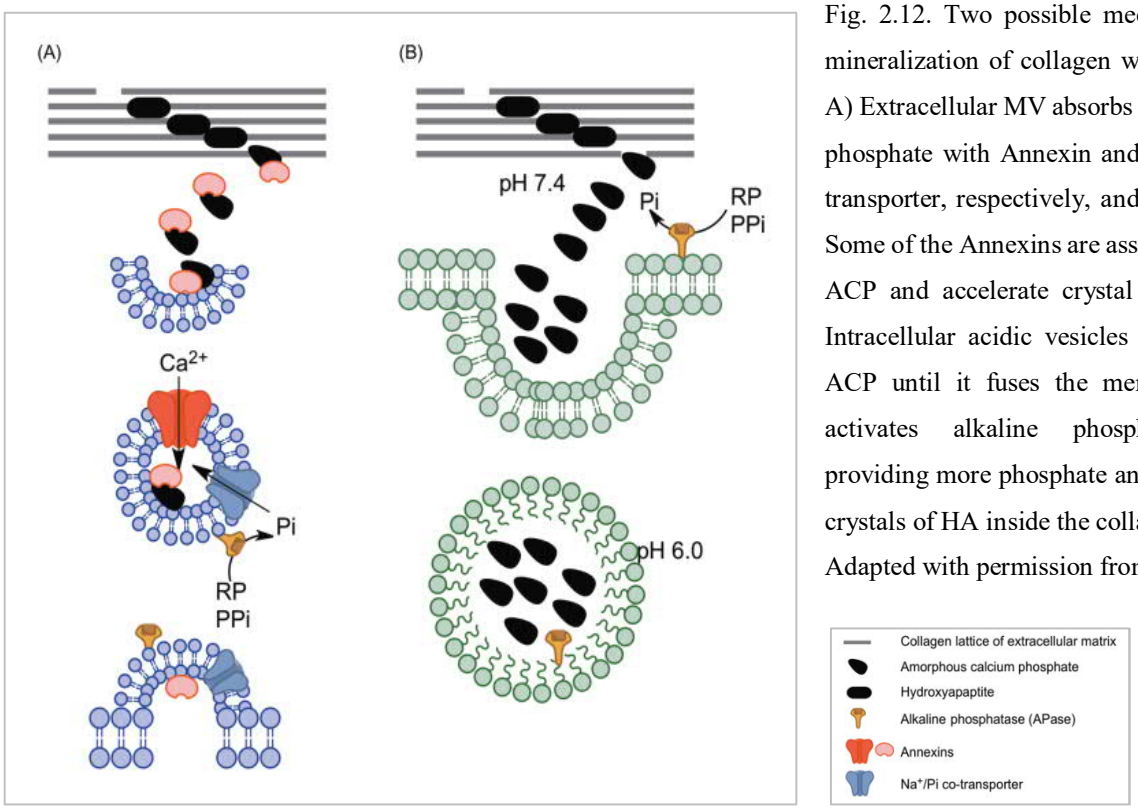

Fig. 2.12. Two possible mechanisms of mineralization of collagen with vesicles. A) Extracellular MV absorbs calcium and phosphate with Annexin and Na+/Pi co-transporter, respectively, and form ACP. Some of the Annexins are associated with ACP and accelerate crystal growth. B) Intracellular acidic vesicles form stable ACP until it fuses the membrane and activates alkaline phosphatase for providing more phosphate and producing crystals of HA inside the collagen matrix. Adapted with permission from [88].

2.3.3 Mediators and inhibitors of mineralization

In contrast to the MV pathway of mineralization, many studies suggest that body fluids, such as blood [102], are usually highly concentrated with calcium and phosphate, which makes transport of ions possible to desired sites, such as bone and teeth [108]. It has also been reported that intercellular space is connected to the endothelium, which provides ions from blood [99]. Calcium transporters, such as vitamin D [109] or fetuin [99], were suggested to be involved too. However, these pathways do not provide a solid explanation for the absence of ectopic mineralization in the healthy case and do not account for the steep gradient in mineral content at mineralizing surfaces. In order to prevent ectopic mineralization, it is suggested that the presence of inhibitors at those sites where mineralization is not desired, such as the cardiovascular system [53], reduces the risk of mineral formation. To annul the effect of inhibitors at those tissues where mineralization is essential, enzymes such as tissue non-specific alkaline phosphatase (TNAP) actively induce mineralization [53].

In the absence of vesicles, the main components that control the deposition of minerals, are collagen and NCPs. Collagen fibril gap zones are suggested as the favorable sites for initiation of mineralization [90] (see Fig. 2.5.B). Fig. 2.13 shows TEM images of collagen fibril and the scheme of dark and bright bands in the overlap and gap zones. Dark bands (shown by spring) are free of proline and hydroxyproline;

however, these imino acids are predominantly found in bright bands (shown by cylinder). Silver *et al.* showed that the e2 band in the gap region (Fig. 2.13.A) could attract and bind ions for crystal nucleation [98]. Traub *et al.* showed that in tooth dentin, the e2 band of the gap region could bind dentin phosphophoryn to mediate the formation of apatite [110]. With regard to the charges provided by collagen, the role of collagen in the mineralization process was intensely investigated [111, 112]. The positive charge at the border of gap and overlap zones can interact with the negatively charged pre-nucleation clusters in the presence of poly aspartic acid (formed via PILP) [96]. Charged amino acids of side chains of polypeptide near overlap and gap zones are also playing a role in mineralization. However, it is essential to know whether charged residues are pointing toward or away from gap zones of collagen [26, 87]. In addition to the effect of collagen on mineralization, at the molecular level, some studies suggested that the organization of the collagen matrix can alter the formation of hydroxyapatite. It was reported that cartilage has a looser matrix than bone, which can accommodate larger inhibitors [88]. In other words, collagen filters proteins like NCPs based on their size and prevents molecules larger than 40 kDa from entering the fibril [113].

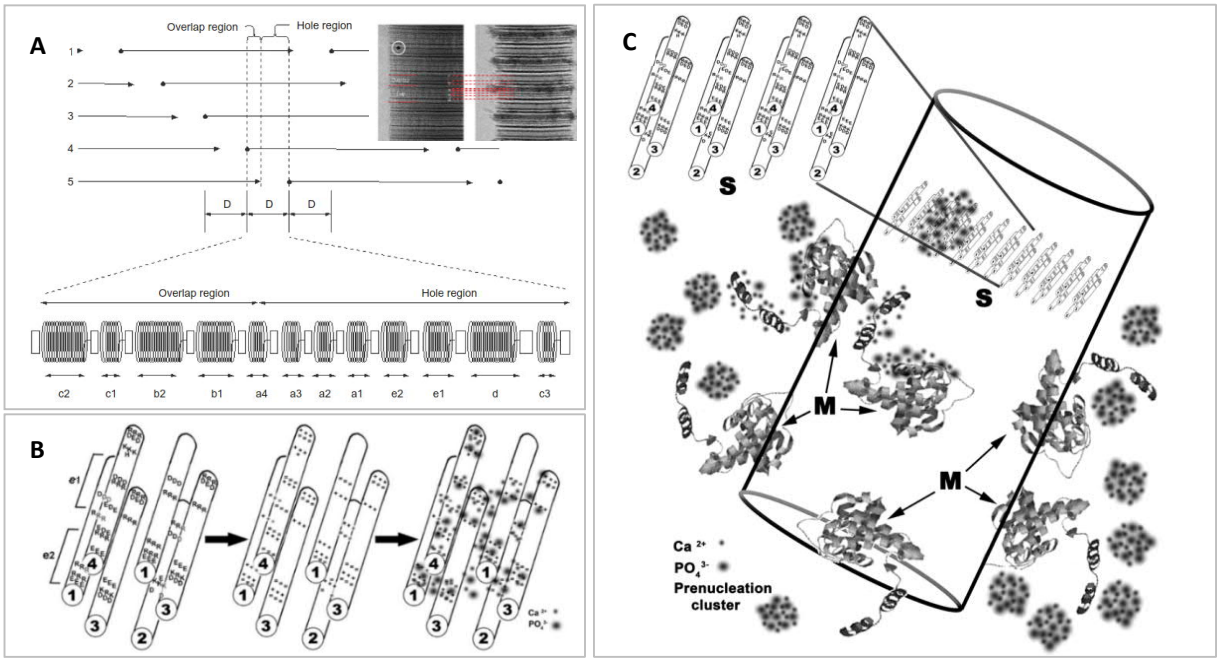

Fig. 2.13. A) Spring and cylinder model for the representation of bands visible with electron microscopy inside gap and overlap zones. Springs are charged regions devoid of proline and hydroxyproline. e2 band is known for binding calcium and phosphate. Reprinted with permission from [98]. Inset shows TEM images of a collagen fibril and its gap and overlap zones. Adapted with permission from [114]. B) Attracting and binding of calcium and phosphate to the negative and positive side chains of amino acids, respectively. C) Intrafibrillar and interfibrillar mineralization by charged amino acids of type I collagen polypeptides and NCPs, respectively. Reprinted with permission from [26].

Acidic macromolecules, like some NCPs, can sequester and bind calcium and phosphate differently [53]. While some NCPs polymerize phosphate or bind it covalently, some other interact with calcium electrostatically. For instance, DMP1 has a high capacity to bind calcium [115]. For release of the ions, different mechanisms are responsible too. Phosphate is liberated by the action of enzymes, such as TNAP, but calcium is regulated by pH and salinity [53]. Therefore, various interactions between NCPs and mineral ions can have different mineralization effects, namely inhibition and promotion of mineralization [102].

Many NCPs are known as mineralization inhibitors. Their inhibition effect is critical as they inhibit mineralization in regions where the mineral formation is not desired, such as the cardiovascular system [53]. Such inhibitors are called systemic mineralization inhibitors (such as fetuin-A). Local NCPs can annul inhibition in forming bone and promote mineralization. Bone sialoprotein (BSP) is an NCP, which is responsible for the rapid mineralization and nucleation of hydroxyapatite [37, 116]. BSP is found in the extracellular matrix of bone and teeth but not in the non-mineralized matrix [117]. Osteopontin, which is secreted by osteoblasts and osteocytes [118], is another NCP that can act like negatively charged acidic polymers in intrafibrillar mineralization of collagen. It has 8-10 aspartic acid residues for sequestering ions in supersaturated solutions [95]. It should be noted that some NCPs, such as osteopontin, can have "dual function", and act as both inhibitor and promotor of mineralization based on the conditions, such as concentration, temperature, and being soluble or attached to a substrate [87, 90]. Biglycan is known as apatite nucleator but inhibits the growth of apatite [12]. SIBLINGs family of NCPs, which are acidic proteins, usually inhibit mineralization. SIBLINGs can recognize collagen, and their charged or phosphorylated conformation, may extend to interfibrillar regions and consequently attract the ions for mineral nucleation [26]. They are also suggested to stabilize ACP by sequestering calcium and phosphate in zebrafish [56].

NCPs function also based on their size. Small NCPs such as osteocalcin expressed in osteoblasts (< 6kDa) can diffuse to the collagen structure [26, 87]. Negatively charged groups of osteocalcin interact with positively charged calcium cations and mediate nucleation and growth of minerals [119]. It was suggested that they might keep the cells from being harmed by the direct contact with the mineralized matrix and also may make the canaliculi free of minerals around the mature osteocytes [37]. Osteocalcin is not found in the unmineralized matrix (osteoid) and mostly exist in mineralizing and mineralized tissue [119]. On the other hand, most of the NCPs are too large (>40 kDa) and cannot enter collagen [26]. Fetuin is another inhibitor with a size of 48 kDa. It is the most abundant serum inhibitor synthesized in the liver. Fetuin is a circulating protein that accumulates in the bone extracellular matrix [120]. *In vitro* studies have shown intrafibrillar mineralization of collagen in the presence of fetuin. This effect is because of the filtering behavior of collagen that does not allow large molecules (> 40 kDa) to go to intrafibrillar spaces [113]. It was also

shown that ACP is stabilized by fetuin [121]. Collagen provides an aqueous environment to exclude fetuin but not calcium and phosphate [113, 122].

Beside NCPs, inorganic molecules have also been suggested to act as mineralization inhibitors [123]. Pyrophosphate is a small molecule secreted by osteoblasts made of two phosphate ions linked by an ester bond. It inhibits mineralization by binding to the surface of hydroxyapatite crystals and prevent crystal growth. It is also suggested that it retards the transformation of ACP to crystalline apatite [124]. Moreover, pyrophosphate can up-regulate osteopontin and inhibit the activity of alkaline phosphatase, both of which result in inhibition of mineralization [123].

In mineralized tissues, the concentration of pyrophosphate is ~0.5% of the total phosphate content [125]. However, in some environments, such as in milk, the concentration of pyrophosphate is so high that it can maintain the high calcium and phosphate content in the colloidal state without precipitating [124]. The concentration of pyrophosphate in the plasma is in the range of 1-6 μM, which is necessary to inhibit ectopic mineralization. It has been reported that in patients with vascular calcification, the concentration of pyrophosphate is reduced [124]. The main source of extracellular pyrophosphate is adenosine triphosphate (ATP), which is hydrolyzed by ecto-nucleotide pyrophosphatase/phosphodiesterase (NPPs) [124]. In hyaline articular cartilage, which is kept unmineralized, it was observed that chondrocytes release ATP [126], which can consequently generate pyrophosphate. Another source is the intracellular pyrophosphate, which can be transported through the membrane protein ANK to the extracellular environment. TNAP, which is a circulating enzyme, cleaves pyrophosphate and increases the concentration of phosphate ions [102]. Tight regulation of NPPs, ANK, and TNAP expression and activity are critical since they determine the pyrophosphate level, which can avoid hypo- or hyper-mineralization. For instance, lower levels of NPP1 were observed in osteoarthritis patients. In general, the ratio of phosphate to pyrophosphate can determine whether mineralization happens or not [124]. Pyrophosphate has also been introduced as a therapeutic agent to inhibit aortic calcification when it is injected into the body [124].

2.4 Role of the osteocytes in mineralization

2.4.1 *In vitro* models

Barragan-Adjemian *et al.* [18] conducted an *in vitro* study of MLO-A5, a post-osteoblast/pre-osteocyte cell, to investigate the early stage of mineralization in association with osteoblasts/osteocytes. They observed that osteoid osteocytes (the immature osteocytes located in the osteoid) and osteoblasts are polarized toward the mineralization front suggesting their activity with respect to the mineralization. They also proposed that primary minerals in the spherical structure are budded from cells and become integrated with the maturation

of osteocytes [18]. Mikuni-Takagaki *et al.* [127] studied matrix mineralization during the differentiation of osteoblast to osteocyte in an *in vitro* model. They observed that osteocytes did not express alkaline phosphatase and leave a free of alkaline phosphatase matrix in their vicinity. Under these conditions, a group of phosphoproteins in a postsecretional process may act as nucleating agents for mineralization. Moreover, casein kinase II, which was highly expressed by osteoid osteocyte, can phosphorylate the matrix proteins BSP2 and induce mineralization [127].

In general, there are some limitations in *in vitro* studies that make it necessary to work under *ex vivo* conditions. First, cell lines do not behave exactly like real osteocytes, although they share a large number of properties with them. For instance, it is likely that the LCN is involved in the mineralization process, but this network is usually not formed in *in vitro* cultures [18]. Second, the mineralization process involves hormones, inhibitors, and signals, which are received from other cells. However, the cell culture medium usually contains a limited number of factors necessary for cell metabolism. Hence, more attention should be paid with the interpretation of the *in vitro* studies.

2.4.2 *Ex vivo* models

Palumbo [128] observed the polarization of osteocytes in the woven bone of chick tibia due to the shifted position of the nucleus toward the vascular side and the higher number of cytoplasmic processes toward the mineralization front. She suggested that the osteocyte processes toward the mineralization front are involved in the mineralization, and the processes toward vasculature are essential in cell nutrition. However, MVs or protrusions were not seen at the plasma membrane facing the vessels. Therefore, it was suggested that the mineralization of the osteoid between osteoid-osteocytes and osteoblasts is controlled by the latter [128]. Roschger *et al.* [73] used a correlative imaging approach (CLSM and qBEI) to demonstrate the quantitative relation between the density of the LCN and the mineral content quantitatively in human osteons. They found that bone tissue is more mineralized near the Haversian canal, where a higher density of osteocyte network exists, and they hypothesized that improved transport of mineral precursors happens through the LCN. They also speculated that local hypermineralization around the LCN could be the reason for the higher density of minerals [73]. Hesse *et al.* [23] studied bone mass density distribution and its relationship to the LCN in the human jawbone with phase-contrast nano-CT. They found that adjacent to both lacuna and canaliculi, higher mineral density exists. Therefore, they suggested that the transport of minerals occurs with diffusion. They also reported that with increasing tissue age, this effect diminished, and mineral density adjacent to the LCN was close to the average mineral density [23]. In another study, Kerschnitzki *et al.* [129] investigated bone mineral particle size and arrangement with respect to the LCN in sheep femur with CLSM imaging and small-angle x-ray scattering. They found that in the matrix with denser LCN, minerals are thicker and more oriented. They interpreted that osteocytes directly interact with

their matrix and minerals [129]. In a nanomechanical study, Zhang *et al.* [130] investigated bone samples of rats with nanoindentation and backscattered electron imaging. They found that the bone matrix in the vicinity of the LCN lacks stiffness in comparison to the bone matrix that exists further away [130]. In a study of the lactating mice, Qing *et al.* found that during lactation, the lacunar size significantly increases, which can be an indication of osteocytic osteolysis. They also observed that the osteocytic resorption of the bone matrix happens reversibly, and the lacunae reach their normal size seven days after the end of the lactation period [131].

2.5 Novel techniques for 3D imaging of the lacuno-canalicular network (LCN) within bone

Methodological developments in the last decades made it possible to characterize material composition and organization at the micro- and nanoscale. When aiming for a thorough description of bone material, the characterization of its structure is crucial in view of its hierarchical organization [2]. Several studies have shown that the micro- and nano-structure have significant impacts on bone mineralization process and biomechanics, such as stiffness and toughness, in health and diseases [73, 132, 133]. Moreover, much effort has been taken to characterize the osteocyte network topology and network-material interaction. However, only recently, a few techniques made it possible to analyze these quantities three-dimensionally, and there is still much unknown about the structure-function relationship of the network and the role of the osteocytes in bone mineralization [9, 23]. The commonly used methods are principally divided into three categories [134]: 1) scanning electron microscopy-based 3D techniques, such as focused ion beam-scanning electron microscopy (FIB-SEM) and serial block face-scanning electron microscopy (SBF-SEM) [135], 2) confocal laser scanning microscopy (CLSM) [136] and 3) X-ray computed tomography (CT) [23]. Fig. 2.14 shows the 2D and 3D images of the LCN obtained by these three techniques. In this section, the physics and applications of these techniques are explained.

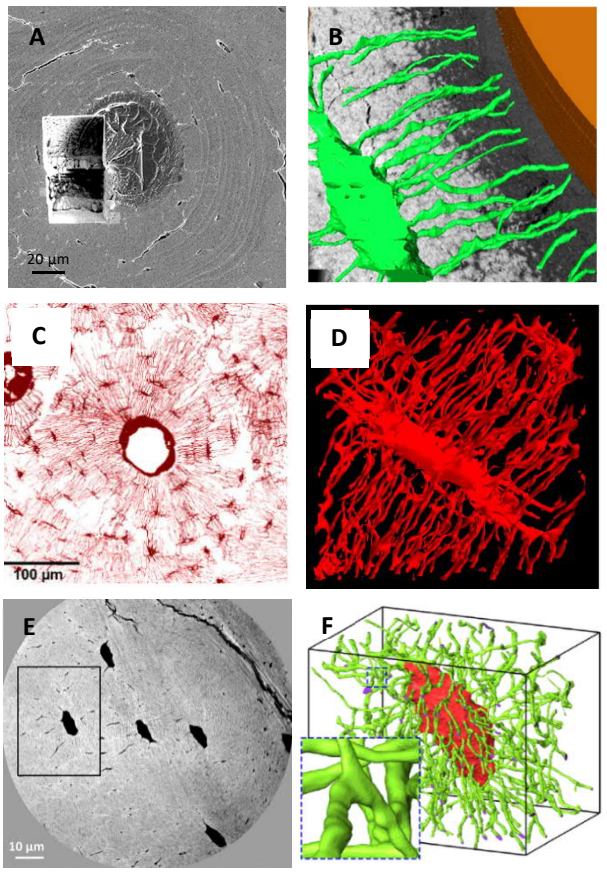

Fig. 2.14. Three classes of imaging modalities for visualization of the LCN within bone. A) A 2D SEM image of bone obtained with FIB-SEM. The hole shows the ROI, which was milled by the ion beam to be imaged with higher resolution SEM. B) The 3D reconstructed image of an osteocyte lacuna and its canaliculi within the ROI imaged with FIB-SEM. The spatial resolution of images obtained by FIB-SEM can be 10 nm (the images were produced within this study). C) A 2D image of the LCN with confocal laser scanning microscopy (CLSM). D) The 3D reconstruction of the LCN, which is stained with rhodamine. Reprinted with permission from [136]. CLSM provides a wider field of views than FIB-SEM; however, its resolution is not as high as FIB-SEM. E) A 2D nano-CT image of bone where osteocyte lacunae (black dots) are visible. F) The 3D reconstruction of a lacuna and its canaliculi. The field of view in this nano-CT image is ~100^3 µm^3, and image resolution is ~60 nm. Adapted with permission from [23].

2.5.1 Scanning electron microscopy-based 3D techniques (FIB-SEM and SBF-SEM)

FIB-SEM is a new technology that combines ion and electron beams to enable the monitoring of the milling process by electrons [137]. One valuable and widespread application of this monitoring is serial slicing (by FIB) and imaging (by SEM) that provides a stack of images that can be reconstructed for visualization of different types of materials such as semiconductors and biological materials [138, 139]. The main components of FIB-SEM are the ion and the electron columns, which are oriented at the 54° (that can varies a bit for different setups) with respect to each other (Fig. 2.15.A). Therefore, the sample needs to be tilted 54° to have the ion beam milling the sample perpendicularly to its surface. This configuration, and the size of the electron and ion optics, dictates a single coincidence point (working distance as 5.1 mm in the setup used in this study).

The ion beam is generated in the FIB column where gallium ions (used in the setup of this work) are formed on the tip of a tungsten needle. In some setups, helium is used for the generation of ions, which results in finer milling. Gallium is usually used because of its low melting point, low vapor pressure, and low surface energy, all of which facilitate gallium ionization [137]. Ions are passed through different ion-optical

elements to be focused and have defined current when hitting the sample (Fig. 2.15.B). First, the beam is refined by passing through spray aperture and then condensed in the electrostatic lens. Beam stigmatism is adjusted afterward by the upper octopole. Then, there are variable apertures to adjust the beam current between 1 nA and 10 nA. The low currents are employed for high-resolution imaging or fine milling, while higher currents are used for fast and rough milling. The beam can be blanked by the blanking deflector and aperture if needed. The lower octopole is utilized for raster scanning over the sample. For focusing on a small spot in the sub-10 nm range, the second electrostatic lens is used. Finally, in some instruments, the multichannel plate (MCP) is used for collecting secondary particles for imaging [138].

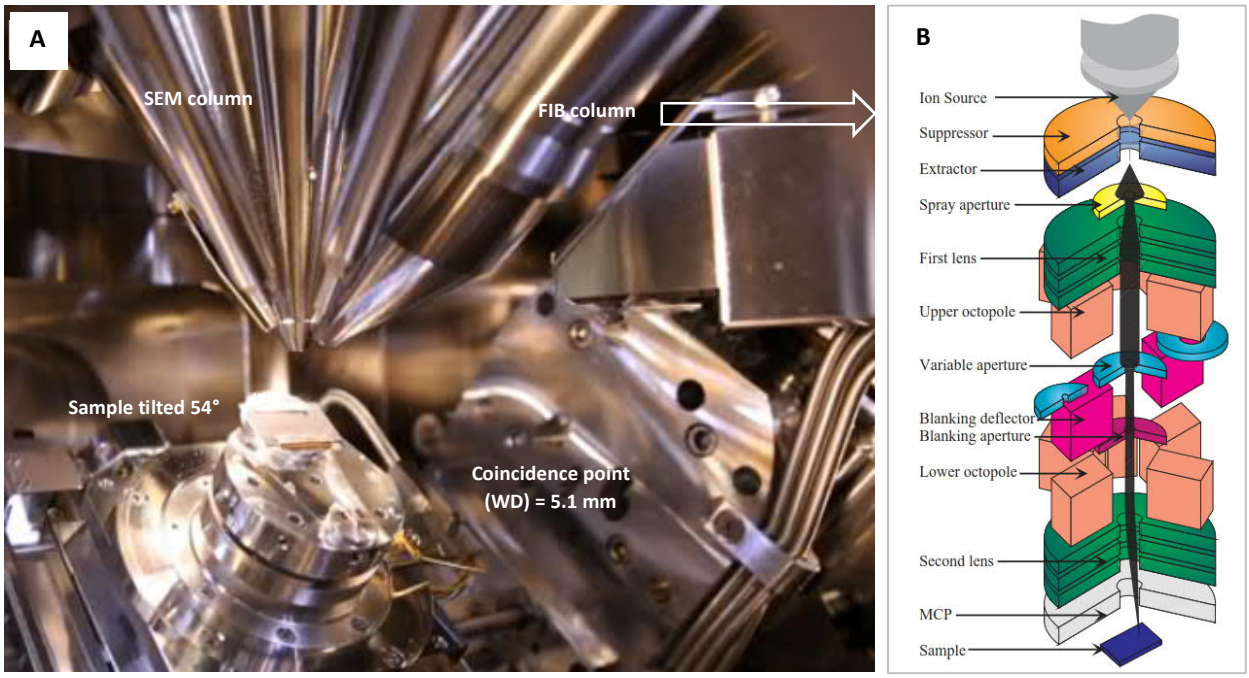

Fig. 2.15. A) A FIB-SEM setup. FIB and SEM columns are located at 54° with respect to each other. With a fully motorized stage, the surface of the sample is tilted at 54° to be perpendicular to the ion beam. The coincidence point at which both FIB and SEM are focused (WD) is 5.1 mm. B) Scheme of FIB column and different objects employed for tuning and focusing ion beam. Reprinted with permission from [138].

FIB has three main functionalities, including imaging, milling, and deposition (for both metals and insulators) [138]. When it is used in combination with SEM for serial slice imaging, the milling purpose is playing a pivotal role. Milling is happening by a physical phenomenon called sputtering. It occurs in a series of elastic collisions where incident ions transfer their momentum to the target atoms in a collision cascade (Fig. 2.16). A surface atom (neutral or ionized) is ejected as a sputtered particle if the kinetic energy of the

primary ion is more than the surface binding energy of bombarded material. After passing the collision cascade, the primary ion will lose its kinetic energy and implanted inside the material at some depth. Inelastic interactions can also occur, resulting in the production of phonons, plasmons, and secondary electrons (SE). The emitted SE is detected and used for imaging during the milling process with FIB [138].

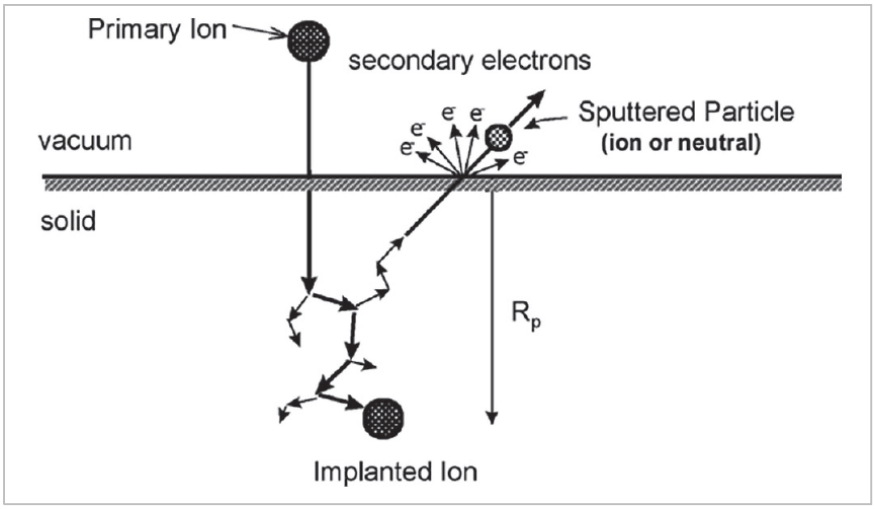

Fig. 2.16. Scheme of the sputtering process. When primary ion collides the surface of the target, it will eject the target atoms within an elastic collision cascade until it loses its initial kinetic energy and becomes implanted inside the target. Reprinted with permission from [138].

The scanning electron microscope (SEM) is the other part of FIB-SEM that is used for imaging. It has a similar column to the one used to generate the FIB, but instead of ions, electrons are extracted from the cathode and accelerated to collide with the material (Fig. 2.17.A). Electron-material collision induces different interactions. The typical particles generated through these interactions are secondary electrons, backscattered electrons, auger electrons, and X-rays that have different interaction volumes (Fig. 2.17.B). Secondary and Auger electrons are low energy electrons and emitted mostly from near the surface (~1 nm and ~100 nm from the surface, respectively). Backscattered electrons have higher energies and come from deeper regions (~1 µm). X-rays have the largest interaction volume and can be emitted up to ~10 µm below the surface. They are used for elemental analysis with energy-dispersive X-ray spectroscopy (EDX) [140].

For imaging purposes, secondary and backscattered electrons are typically detected. Secondary electrons are produced by inelastic collisions of primary electrons and collected easily by positively biased collector grid. Due to the enhanced emission of SE on the edges, they are widely used for topography [140]. This enhancement happens as a result of the increase of the secondary electron coefficient with the tilt angle. When the tilt angle increases, the path that the primary electron beam passes through the escape depth (the

size depends on the material nature) of the secondary electrons increases. As the secondary electron coefficient is proportional to this path length, higher tilt angles, which are usually found on the edges, are brighter in the secondary electron images [141]. Therefore, these images are used to observe the topography of the surface. It should also be noted that a fraction of secondary electrons is generated by backscattered electrons. Therefore, secondary electron images also represent, to some extent, the composition of the materials [141].

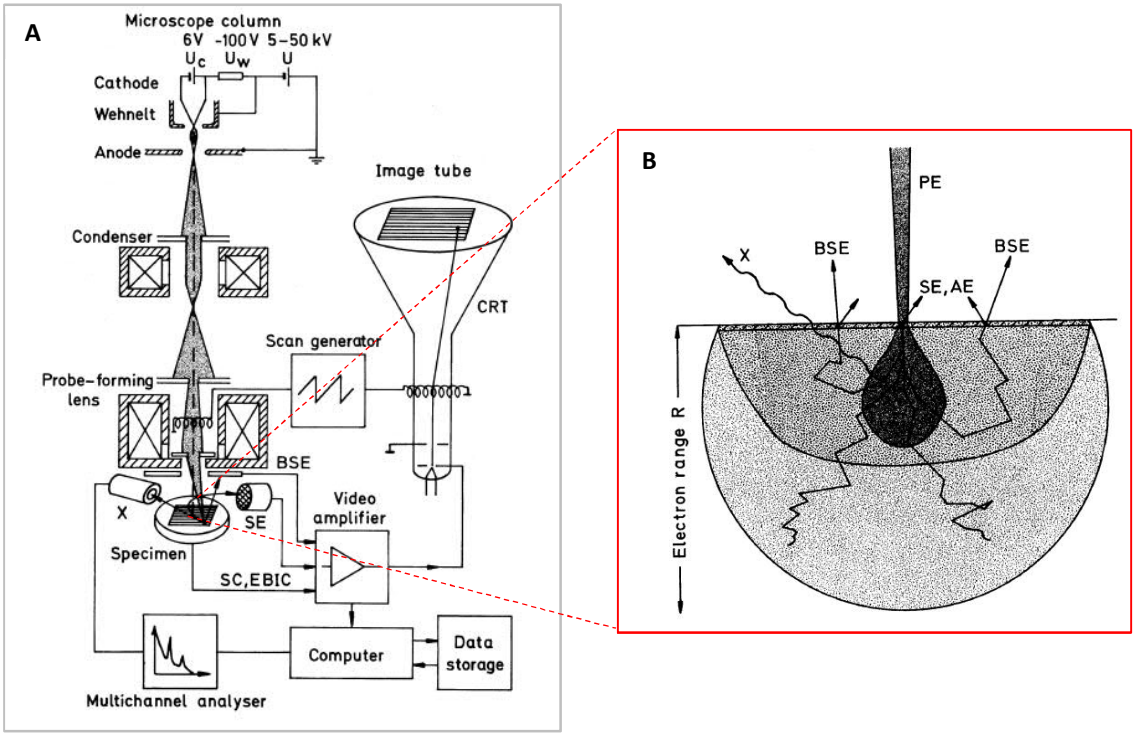

Fig. 2.17. A) Scheme of a scanning electron microscope and its internal component for electron generation and collection. Similar to FIB, electrons are accelerated by different potentials between cathode and anode in a column. Then the electrons are demagnified with an electron lens system to generate an electron probe (with 1 pA-10 nA current and 1-10 nm diameter). B) Different types of interactions of electrons with the material. Primary electrons (PE), secondary electrons (SE), backscattered electrons (BSE), and Auger electrons (AE) and their interaction volumes are depicted. Adapted with permission from [140].

Backscattered electrons (BSE) are originally primary beam electrons that undergo elastic collision with the target with minor loss of energy and return to the surface with reverse direction to escape the sample [141]. BSE images are widely used because of their atomic number (Z) contrast. It also conveys information on the sample topography, mass thickness, and crystallography. They are quantified with the backscattered

coefficient (η) that shows the ratio of backscattered electrons to the primary electrons. η increases with Z with a sharp slope at low Z elements and a shallow slope at high Z elements (Fig. 2.18). For instance, in bone, Z for hydroxyapatite is ~14, and according to the equation fitted for the curve in Fig. 2.18, η is ~0.16. On the other hand, for both organic matrix and poly(methyl methacrylate) (PMMA), Z is ~6.5. Therefore, not only η is too low (~0.07), but also it is equal for these two phases, and there is no Z contrast of these phases in the BSE images (see chapter 4 for the staining method developed in this study to increase Z contrast for the organic phase). In contrast to the significant effect of Z on η, the primary beam energy does not affect η. This phenomenon can be explained by the balance between two effects. On the one hand, the primary electrons with higher energies lose their energy at lower rates (dE/ds), causing them to retain their energy longer, which increases the probability of escaping the sample elastically. On the other hand, this higher energy causes them to travel through an increased penetration depth. Therefore, the electrons might experience more inelastic scattering through the sample, and consequently, the number of the electrons that can return to the surface with minor loss of energy might reduce [141].

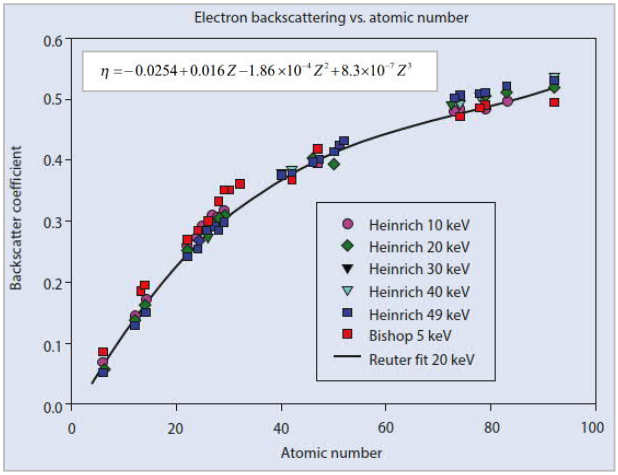

Fig. 2.18. Variation of backscattered electron coefficient with atomic number. Increasing of the atomic number will lead to higher η that gives Z contrast to BSE images. The equation shows the mathematical fit for imaging conditions under 20 keV. Adapted with permission from [141].

Another technique that is also an SEM-based method is serial block face-scanning electron microscopy (SBF-SEM) [135]. This technique has two characteristics in common with FIB-SEM; it uses serial slicing and imaging to provide 3D datasets of the sample, and it is a destructive technique. The main difference between SBF-SEM and FIB-SEM is that in the former, instead of a focused ion beam, an ultramicrotome is employed to slice the sample to reveal a new surface for imaging. Hence, one disadvantage arises here, since only thicker slices (~50 nm) are removed in comparison to the slices milled by FIB, which consequently results in lower axial resolution. This issue causes a non-isotropic resolution because the lateral resolution is ten-fold higher (~5 nm) thanks to the high-resolution imaging by scanning electron

microscopy. A noteworthy advantage of utilizing such a setup for 3D imaging is that a large field of view (~800 μm^2) can be imaged, which provides visualization of up to 100 cells or more in a typical dataset [135].

As the mechanical properties of mineralized tissue make the cutting process challenging, SBF-SEM application on soft tissues, such as brain, is more common. Therefore, to date, this technique has been widely used in neurosciences for neuronal reconstructions [142, 143]. Recent studies, however, show that SBF-SEM can provide images of hard tissues to reveal cellular compartments, e.g. the osteocyte network in undecalcified samples [135]. For such studies, heavy-duty ultramicrotome should be used, since the hard tissue can generate severe knife damage. To avoid cutting issues, a decalcification step is usually added to the sample preparation routine when SBF-SEM is used for mineralized tissues [135]. In this case, the resulting images cannot provide information about the mineralization process since the minerals are already dissolved, but this technique can still contribute to the characterization of the osteocytes network within the matrix.

2.5.2 Confocal laser scanning microscopy (CLSM)

Confocal laser scanning microscopy (CLSM) is another method commonly used for 3D imaging of biological materials [144]. In CLSM setups, instead of using a conventional light source, lasers with different wavelengths are used to provide higher resolution and better image contrast. For CLSM imaging, samples are usually labeled with a fluorochrome, which is a molecule that absorbs light with a particular wavelength and emits light with different wavelengths. This process is shown in the Jablonski diagram in Fig. 2.19.A [144]. In absorption, electrons are excited by the incoming photons and raised to higher energy levels. When they decay to the ground level, they emit photons of specific (different) wavelength, i.e., they generate fluorescence light. A known fluorochrome extensively used for imaging of the LCN in bone is rhodamine with 575 nm and 595 nm excitation and emission wavelengths, respectively. Thanks to the small size of rhodamine (~0.9 nm), it can penetrate through all connected porosities like canaliculi in bone [73].

The mechanism of image generation in CLSM is shown in Fig. 2.19.B [145]. First, the laser beam passes through a dichroic mirror that is wavelength sensitive, and then it is focused on the sample by the objective lens. Afterward, the emission from the sample is guided back to the dichroic mirror and, because of its half-reflective design, the emitted photons are guided toward the convex lens to be focused on the pinhole. The pinhole is the key part of the CLSM system as it removes out-of-focus light, and therefore, higher contrast and resolution in comparison to conventional light microscopes are achieved. Finally, the photons are detected by one or more photomultipliers [145].

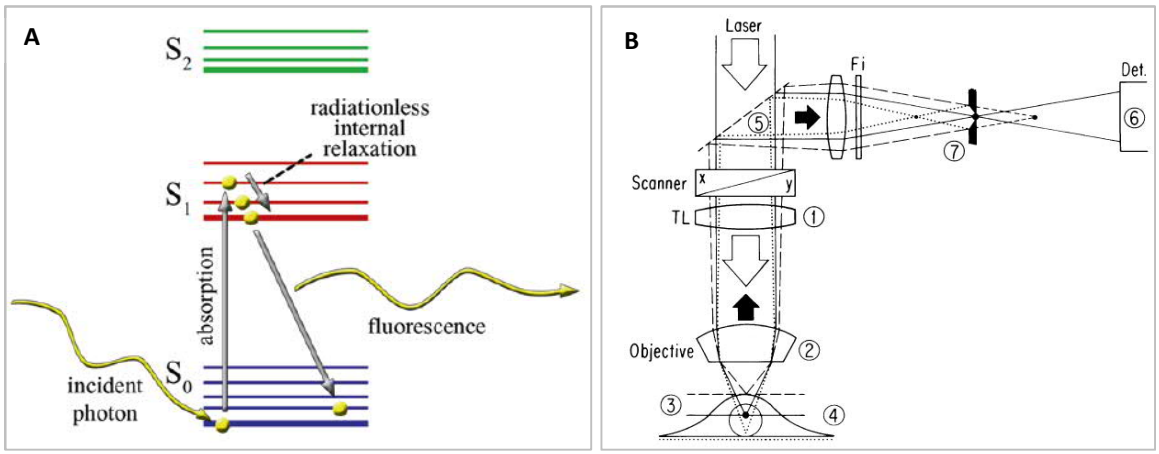

Fig. 2.19. A) Jablonski diagram shows the absorption and emission of photons by a fluorochrome that causes electronic transitions. Reprinted with permission from [144]. B) Scheme of the image formation in a CLSM system; 1) filter, 2) objective lens, 3) out-of-focus layer, 4) in-focus layer, 5) dichroic mirror, 6) detector and 7) pinhole. Reprinted with permission from [145].

2.5.3 X-ray micro-computed tomography (µCT)

Another imaging modality is based on X-ray images obtained in a computer tomography setup. It is the process of acquiring a 3D image of a sample from 2D projections at different angles. Every 2D projection is produced based on the attenuation (i.e., transmitted energy of the beam) of the X-ray radiation on the sample. Depending on the beam energy and also the nature of the material, attenuation can be different and is calculated with the following equation [146]:

$$I_x = I_0 e^{-\mu x}$$

Where I_0 is the intensity of the primary beam, I_x is the intensity of the beam at distance x from the source, and µ is the linear attenuation coefficient. Attenuation is also sensitive to the thickness of the sample. Therefore, 2D projections alone cannot be used for quantification of the characteristics of the materials. This issue is resolved by rotating the sample through 360° (or 180°) to collect as many as possible projections. Afterward, with an image reconstruction algorithm, a 3D volume is generated [146]. Fig. 2.20 shows a scheme of the imaging setup with µCT.

Conventional µCT has a polychromatic beam which produces an artifact called beam hardening. This artifact happens because low energy beams are shielded, while high-energy beams can pass through the

material. The use of synchrotron, where the monochromatic and parallel beam can be used, eliminates this effect [146]. Modern techniques use a nano-focus X-ray source to provide nano-CT imaging. A well-known combination of synchrotron and nano-CT, which is also used for the LCN imaging, is synchrotron radiation phase-contrast nano-CT (SR-PNCT) [23]. In table 2.1, the most important properties of different imaging techniques are summarized.

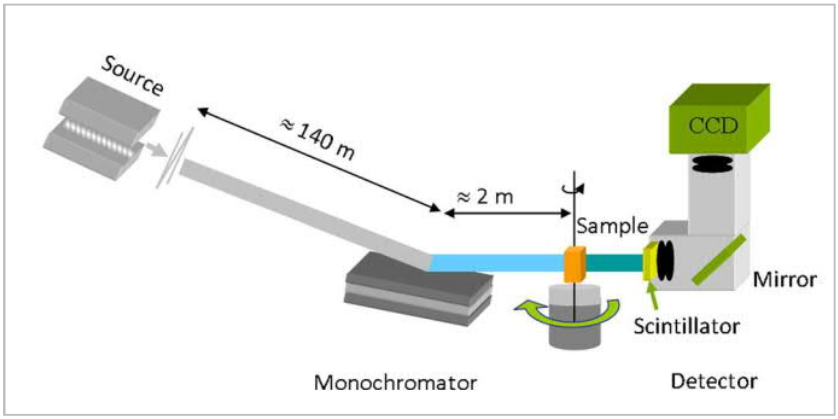

Fig. 2.20. Imaging setup of a synchrotron µCT. For parallel beams, the source is placed at a long distance from the sample. Then, with a multilayer monochromator, a single energy of the primary beam is selected. Afterward, to obtain multiple 2D projections, the sample is situated on a rotation stage that enables imaging in a few thousand angles. Finally, the scintillator converts the X-rays to visible light to enable the CCD camera to detect the projections. Reprinted with permission from [147].

Table 2.1. Different techniques and parameters for imaging of the LCN in the mineralized bone

3D imaging techniques	Type of imaging	Nominal resolution (nm)	Typical field of view (µm^3)	destructive	references
Scanning electron microscopy	FIB-SEM	~5	~10^3	Yes	[135, 148]
	SBF-SEM	~50 axial, 10 lateral	~10^5	Yes	[135]
Laser imaging	CLSM	~200	~0.1 mm^3	No	[136]
	STED	~90 axial, 70 lateral	~50^3	No	[149, 150]
X-ray tomography	µCT	~400	~10^9	No	[135, 151, 152]
	SR-PNCT	~60	~10^6	No	[23]

Chapter 3

Materials and methods

In general, there are mainly three approaches - *ex vivo*, *in vivo,* and *in vitro* - that have been used to study mineralization in biological materials. *Ex vivo* studies refer to those performed on tissues explanted from cadaver [69], live body human [23], or from the animal body [24]. The samples are then fixed and analyzed with various techniques. On the other hand, *In vivo* studies are based on live animal models, such as zebrafish [153], in which cells, blood vessels, or extracellular matrix, can be investigated in their native conditions. Some other works are *in vitro* in which cells, such as osteoblasts [20], pre-osteocytes [18], and bone marrow cells [154], are cultured and studied in the extracellular environment.

In this work, an *ex vivo* study was performed on cadaver human femoral cortical bone. The workflow consists of three main steps. First, the samples were prepared, and different stains were employed for different imaging techniques (3.1). Second, different imaging strategies and characterization methods were used to obtain information about mineralization and the osteocyte network within the samples (3.2). Third, image processing, including preprocessing techniques for cleaning the data from artifacts, and analysis were performed (3.3).

3.1 Sample preparation

Three post mortem samples, which were part of a previous study [73], were obtained from the femoral midshaft of individuals without any known bone-related disease. The samples were obtained at the department of forensic medicine and the department of anatomy of the medical university of Vienna according to ethic commission regulations of the university (EK no. 1757/2013). The samples were frozen and cut in 1 cm thick pieces (from diaphysis, as shown in Fig. 3.1) in the transversal direction. Therefore, as osteons are parallel to the long axis of bone, the circular shape of osteons was preserved (Fig. 3.2.A). For dehydrating the samples, ethanol was used in a dehydration-series in which concentration of ethanol was gradually increased to avoid rapid dimensional changes and possible cracking. Subsequently, the samples were embedded with polymethylmethacrylate (PMMA). With a low-speed diamond saw (Buehler Isoment, Lake Bluff, Illinois), the samples were cut into smaller pieces (~5×5 mm^2 with 1 mm thickness). Afterward, 3 and 1 µm grain size diamond suspension were used (Logitech PM5, Glasgow, Scotland) to polish the sample and achieve a mirror-reflection surface for FIB-SEM imaging. Finally, the samples were stained with rhodamine and iodine for CLSM and FIB-SEM imaging, respectively. Rhodamine staining was done according to the protocol proposed by Roschger *et al.* [73]. Iodine staining was developed in this study based on the protocol developed by Boyde *et al.* [155]. Fig. 3.1 shows the region where the samples were taken from, and the table displays their characteristics.

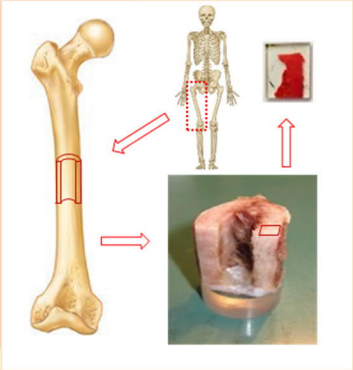

Samples	FM38	FM40	FM48
Age	55	56	48
Sex	female	female	female
Rhodamine staining and Iodine staining	yes	yes	yes
Number of osteons measured	3	3	3

Fig. 3.1. Scheme of sample preparation, showing PMMA-embedded sample extracted from the human cadaver femur of individual FM38. All samples were stained with rhodamine and iodine for CLSM and FIB-SEM study, respectively. For each sample, three forming osteons were measured to visualize the osteocyte network at mineralizing tissue. Adapted with permission from [3, 156].

3.2 Measurement strategies

In this work, the workflow for measuring the bone tissue was mainly based on 2D and 3D imaging and characterization methods. With 2D imaging techniques, regions of interest (ROIs) were selected, iodine staining protocols were validated, and elemental analysis of the bone tissue was performed (3.2.1 and 3.2.5). With 3D imaging techniques, datasets of the lacuno-canalicular network (LCN) in large fields of view with CLSM (3.2.2) and high-resolution datasets with FIB-SEM (3.2.3) were obtained. CLSM and FIB-SEM techniques were also compared in terms of resolution for imaging of the LCN (3.2.4).

3.2.1 Environmental scanning electron microscopy (ESEM) for selection of forming osteons

Using an ESEM, backscattered electron images were obtained from non-coated samples to select ROIs and to evaluate the effect of the iodine staining (see section 4.2.1). For each sample, three forming osteons were selected. Because of the lower tissue age and therefore lower mineral content, the backscattered electron yield of the forming osteons was lower compared to the other osteons. Measurements were performed with an ESEM (FEI Quanta 600, USA) under low pressure (1 mbar) with 12.5 kV acceleration voltage, ~10 mm working distance, and magnifications between 50× and 600×. Fig. 3.2.A and Fig. 3.2.B show images with low and high magnifications of a forming osteon. The visual characteristic of such an osteon is a blurry interface (the mineralization front) between the unmineralized and the mineralized matrix. In the sample preparation, cells were mostly removed, and the canals (i.e., the Haversian canal and the LCN) were filled with PMMA. However, unmineralized tissue consisting mainly of collagen were preserved.

3.2.2 Confocal laser scanning microscopy (CLSM) of the LCN within forming osteons

After finding forming osteons with ESEM, CLSM imaging of bone samples was performed to three-dimensionally visualize the LCN in the regions of interest. The measurement was conducted with an inverted TCS SP8 (Leica, Wetzlar, Germany) equipped with an oil immersion lens (HC PL APO 40×/1.30 OIL). For rhodamine excitation, the 514 nm line of Argon laser was chosen, and the fluorescence signal was measured in a spectral window between 540 and 620 nm with an airy 1 pinhole of 65.4 µm. To find the osteons which were selected with ESEM, first, a 2D overview image (7.7×7 mm) of the whole sample was obtained by stitching (Fig. 3.2.C). Then the forming osteons were imaged in 3D (Fig. 3.2.D and Fig. 3.2.E). For 3D measurements, the parameters of imaging were as follows: Isotropic voxel size = 0.31 µm, image size = 1024×1024 pixel, depth of imaging = 130 slices, scan speed = 200 lines per second. To compensate for the loss of signal observed while imaging through the depth of the sample, the laser intensity and the photomultiplier gain were continuously increased to have a constant brightness and contrast within one dataset.

3.2.3 FIB-SEM measurements of the LCN in the unmineralized and the mineralized tissues

To visualize the LCN, unmineralized and mineralized matrices in one measurement (ROIs were selected with ESEM and CLSM beforehand) and to resolve the ultra-structure components, such as canaliculi and mineralization foci, FIB-SEM (Crossbeam 540 Zeiss, Oberkochen, Germany) was used. The samples were cut to small pieces (~5×5 mm^2 and 1 mm thick) to be mounted easily on the stage. Before mounting, the samples were carbon coated (thickness of ~15 nm) by vacuum carbon evaporator sputter coater (Bal-tec/Balzers, Liechtenstein, Germany). To ensure that the samples were dimensionally stable under the high vacuum (10^{-6} mbar) applied for the imaging (i.e., they would not undergo shrinkage with dehydration), they were mounted inside the vacuum chamber at least 24 hours before image acquisition. Owing to the FIB and SEM columns configuration (see section 2.5.1), the tilt angle was set to 54° so that the sample surface was perpendicular to the ion beam. The working distance (coincidence point of ion and electron beam) was set to 5.1 mm. The milling process was conducted with different ion probes (Fig. 3.3.A). First, a large hole (~100×100×100 $µm^3$) was milled rapidly (~10 minutes) with 65 nA (at 30 kV acceleration voltage) to expose a surface parallel to the ion beam for finer milling (Fig. 3.3.B). Then, in the serial slice and view mode, a typical ROI (~40×30×50 $µm^3$) was milled with 700 pA Gallium ion beam current (Fig. 3.3.C). The slice thickness was 40 nm, and the milling time per slice was ~5 seconds. The dose factor (correlated to the depth of milling in µm for the reference material Silicon) was set to 5 to ensure a milling depth of 50 µm for mineralized tissue. It was observed that unmineralized matrix and PMMA, which are much softer than mineralized tissue, were milled ~100 µm below the surface.

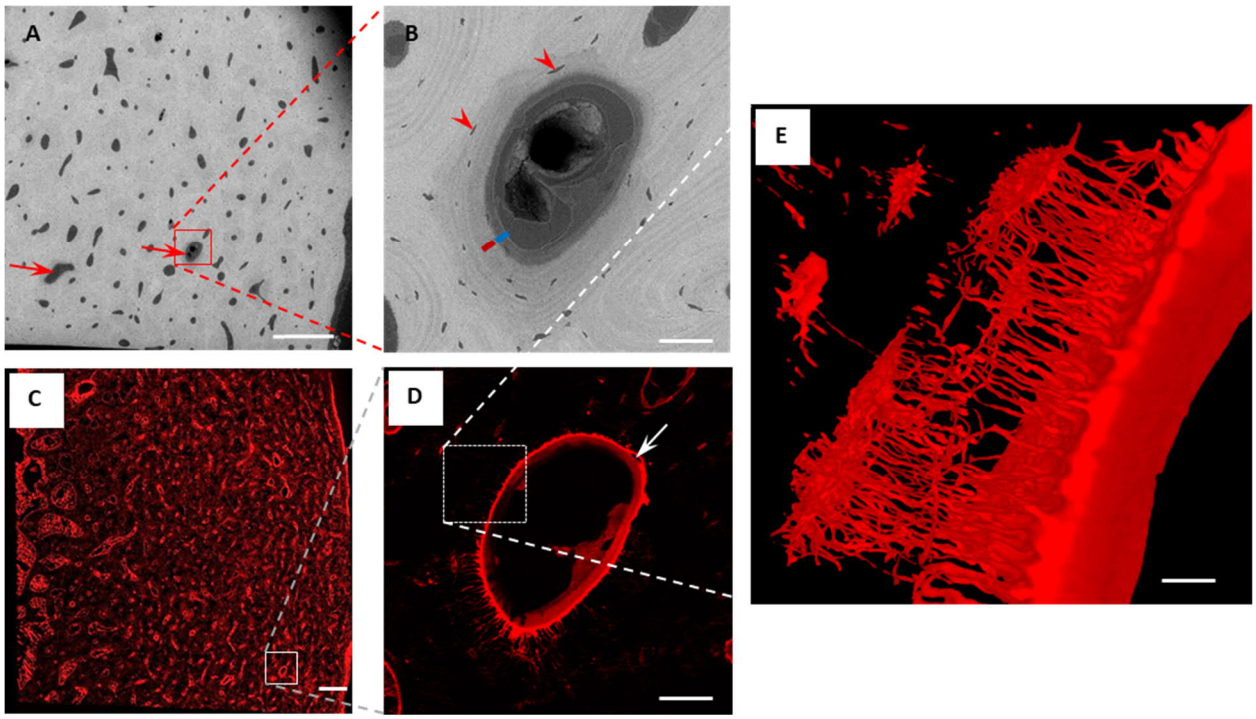

Fig. 3.2. A) An overview ESEM image of the bone cross-section (sample FM38) exhibiting numerous osteons. Brighter regions are attributed to the more mineralized matrix, while regions with lower brightness are less mineralized. The dark spots are Haversian canals within osteons. Two forming osteons with the blurry interface are distinguishable (the arrows). B) A forming osteon at higher magnification (600×) (sample FM38, osteon #1). Unmineralized lamella (the blue bar) between the mineralized matrix (the red bar) and the Haversian canal is visible. There are four surrounding osteons with similar lamellar structures, but they have a different average grey value of the matrix in comparison to the forming osteon. The osteocyte lacunae (the arrowheads) are embedded in the matrix. C) A CLSM overview of the same sample. D) The same forming osteon in Fig. 3.2.B. The arrow shows a lacuna that is located at the interface of the osteoid and mineralized matrix. By 3D imaging with CLSM, the lacuna is visible though it is buried in depth and was not detectable with ESEM. E) The 3D reconstruction of the LCN near the surface of the Haversian canal obtained from the selected region in D (the dashed square). Scale bars for A and C = 500 µm, B and D = 50 µm, E = 5 µm.

After each milling step, the newly revealed surface was imaged with SEM. Secondary and backscattered electron images were simultaneously recorded. High-resolution images (pixel resolution ~40 nm) were obtained with 2.5 kV electron acceleration voltage and 1 nA electron beam current. Acquisition time per image was 28 seconds when the line average noise reduction (N=40) was used. The brightness and contrast were set in a way that no regions were over or under exposed. Therefore, in the histogram of datasets, peaks of brightest voxels (mineralized matrix) and darkest voxels (PMMA) located entirely between 0 and 255

(see chapter 8 for histograms of all FIB-SEM datasets). Fig. 3.5.A and Fig. 3.5.B show examples of secondary and backscattered electron images of a single slice.

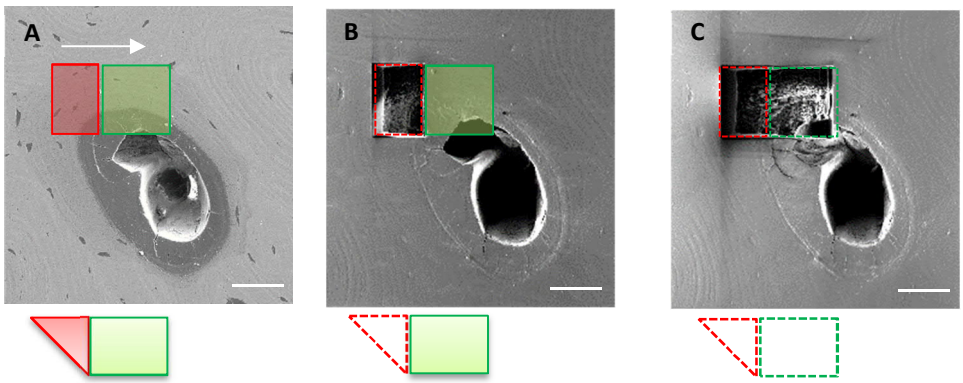

Fig. 3.3. Steps of milling the ROI with FIB-SEM. A) Backscattered electron image of a forming osteon (sample FM38, osteon #1) before milling. B) FIB view of the ROI after rapid milling. C) FIB view of the ROI after milling in the slice and view mode. Red rectangles in the images show the regions, which were rapidly milled with high current ion beams (65nA). Although the dose factor was constant, the cross-section of such a region is triangular (note that the sketch below the images shows the depth of milling). The reason is that milling starts at the surface with low sputtering yield where surface atoms are bound to more atoms around them. As the milling proceeds, the ions will hit the atoms surrounded by fewer neighbors (because of the previously milled region) and, therefore, will be easily retracted. Green rectangles depict the regions milled in slice and view mode with lower ion current (700 pA). The arrow in panel A shows the direction of milling. Scale bars = 50 µm.

3.2.4 Comparison between CLSM and FIB-SEM techniques for imaging the LCN in forming osteons

CLSM and FIB-SEM were both used for 3D imaging of the LCN in this study (Fig. 3.4.A-D). Fig. 3.4 shows the 3D rendering of the LCN near the mineralization front obtained by these two techniques. There are regions at the mineralization front and in the unmineralized matrix where no canaliculi are seen with CLSM (Fig. 3.4.D), while FIB-SEM imaging reveals that there are LCN at those regions (Fig. 3.4.C). This distinction is mainly because of the unspecific staining of bone by rhodamine. Rhodamine stains mineralized tissue walls and unmineralized tissue. Therefore, canaliculi walls in the mineralized matrix are nicely stained; however, in the unmineralized matrix, those walls, as well as organic tissue, are all stained and canaliculi are not distinguishable.

Another issue with CLSM is the resolution limit. Lateral resolution is the smallest distance between two objects, which can be resolved by the microscope. For confocal microscope, it is defined with the following equation [144]:

$$r = {}^{0.4\lambda}/_{NA}$$

where r is the minimum resolved distance, λ is the fluorescence wavelength, and NA is the numerical aperture. For a laser fluorescence with 500 nm wavelength and a 40× oil lens with 1.3 numerical aperture, the resolution is approximately 150 nm. In comparison to electron microscopy with much smaller probe sizes (thanks to the small wavelengths of electrons) that provides a higher resolution (a few nanometers), confocal microscopy resolution is not sufficient to resolve canaliculi with ~200-400 nm in diameter. Therefore, canaliculi were observed wider with CLSM than electron microscopy (Fig. 3.4.E).

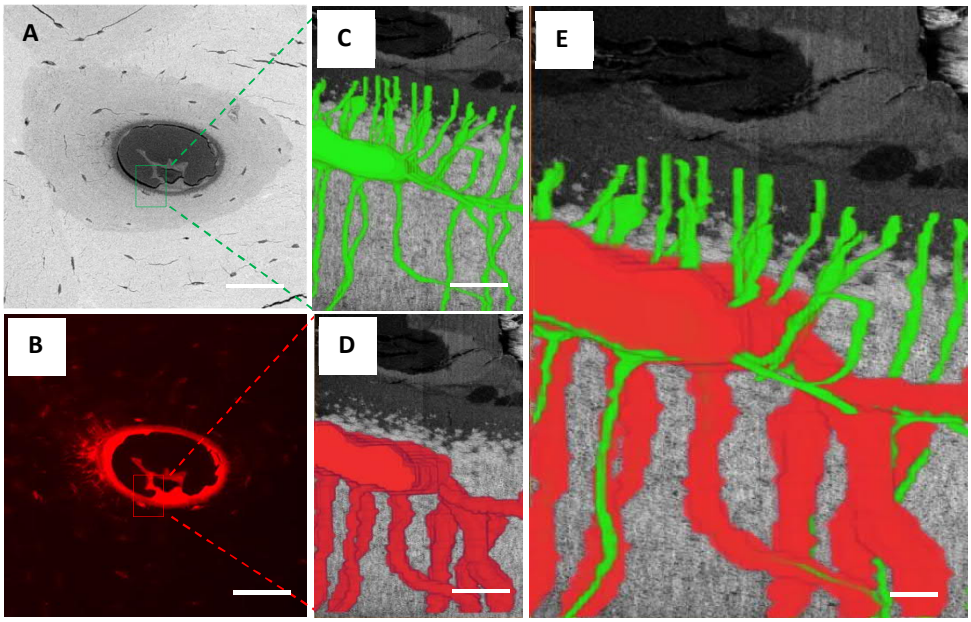

Fig. 3.4. A representative example for correlative imaging of the LCN within bone using FIB-SEM and CLSM (sample FM48, osteon #1). A) ESEM image of a forming osteon in which green rectangle shows the region of interest, which was later imaged with FIB-SEM. B) 2D CLSM image of the same osteon in which the red rectangle shows the region of interest, which was imaged with CLSM in 3D. C) 3D rendering of the LCN within unmineralized and mineralized matrices obtained with FIB-SEM images. D) 3D rendering of the LCN within the mineralized matrix obtained with CLSM images. E) Registration of 3D renderings of the LCN in which green and red colors are related to FIB-SEM and CLSM imaging, respectively. The background is a backscattered electron image of the FIB-SEM dataset. Note that the canaliculi exist at the mineralization front; however, they are not distinguishable by CLSM as rhodamine stains the entire unmineralized tissue. The difference in resolution of these two imaging techniques is also noticeable, as the canaliculi look much wider in CLSM 3D rendering in comparison to FIB-SEM 3D rendering. Scale bars for A and B = 50 µm, C and D = 5 µm, and E = 2 µm.

3.2.5 Energy-dispersive X-ray spectroscopy (EDX) maps of the unmineralized and the mineralized tissues

To characterize the distribution of major elements of bone such as calcium and phosphorous and also to see the distribution of iodine qualitatively, EDX maps were obtained (only for selected slices and not for the whole slice and view process). For this, a large-area silicon drift detector (X-Max^N TLE, Oxford Instruments, UK) was used. The detector was windowless, which could collect X-rays of low atomic number elements in a short time. With EDX, energies of the characteristic X-rays of the elements excited by the electron incident beam were recorded as a spectrum (number of counts vs. X-ray energies) [157]. Fig. 3.5.F shows the spectrum of the X-ray energies of the iodine-stained bone sample. Such a spectrum provides qualitative and quantitative information since the position of peaks identifies the elements, and the area under each peak indicates the number of atoms in the electron-irradiated region [157]. To detect characteristic X-ray of iodine ($L_{\alpha 1}$ = 3.937, $L_{\beta 1}$ = 4.221, $L_{\beta 2}$ = 4.507 and $L_{\gamma 1}$ = 4.801 keV [158]), 10 kV accelerating voltage was used. The acquisition time was set to 2500 seconds for the whole image, and drift correction was applied. The resolution of maps was 60 nm, and the field of view was 40×30 μm^2. Fig. 3.5.C-E show EDX maps of calcium, phosphorous, and iodine at the mineralization front of a forming osteon.

3.3 Image processing

Imaging of bone tissue with electron microscopy not only provides qualitative information of the regions at different mineralization stages but also gives a semi-quantitative data that can be used for a thorough investigation of mineralization. Imaging artifacts generated during the imaging process, such as misalignment, background noise, and curtaining/striping, were processed with in-house algorithms for further image segmentation and analysis (3.3.1-3.3.3). Afterward, segmentation of the Haversian canal and the LCN within bone tissue was performed to specify the reference surface for distance maps (3.3.4). Based on these segmentations, distance maps giving the exact distance of each voxel to the reference surfaces (3.3.5) were produced. Finally, a correlation method was developed to correlate between voxel grey values and their distance values (3.3.6).

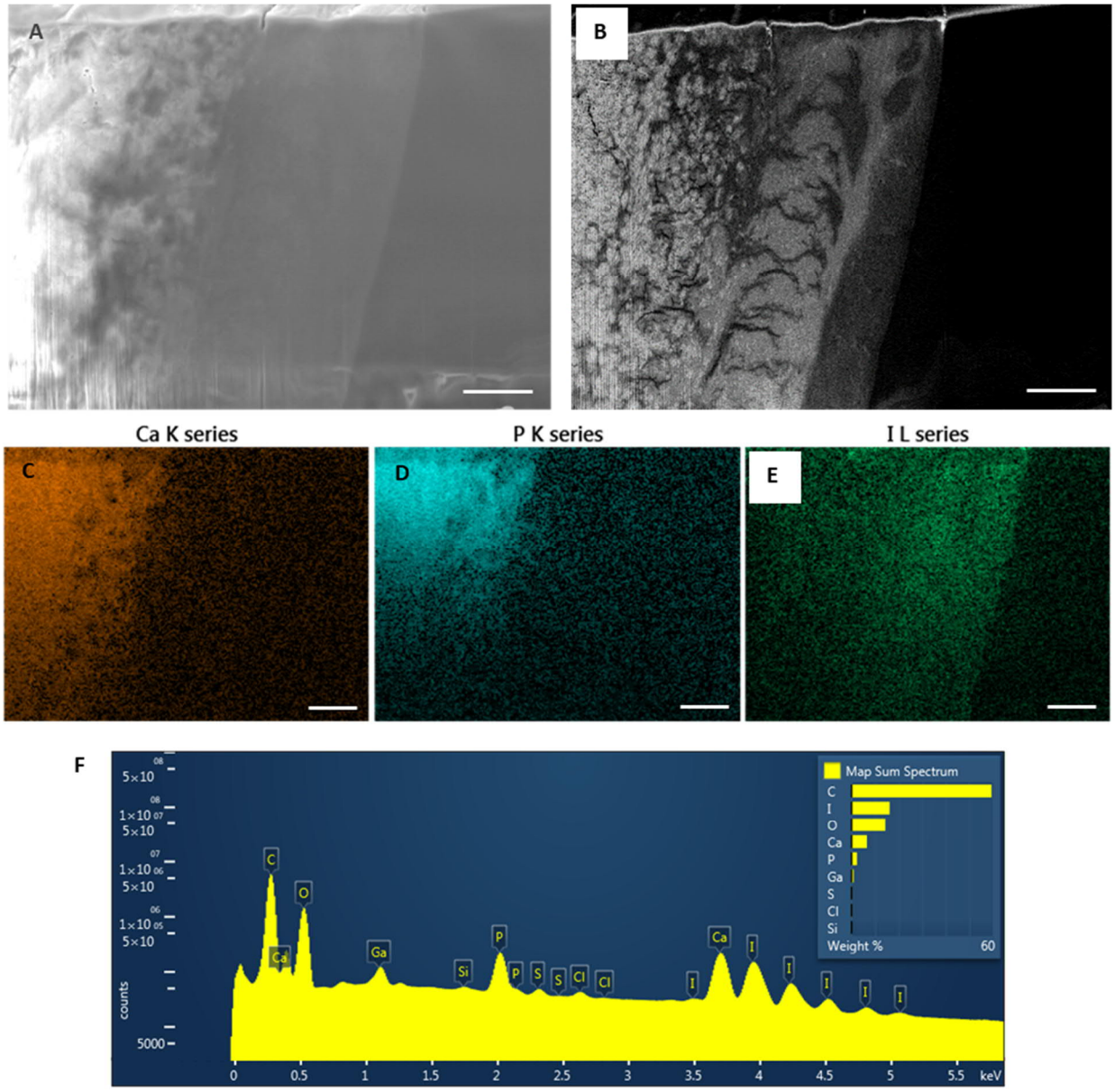

Fig. 3.5. A) Secondary electron and B) backscattered electron images of mineralized tissue, unmineralized tissue, and PMMA. C-E) Calcium, phosphorous, and iodine distribution at the mineralization front. Note that iodine mostly stained unmineralized matrix, and PMMA is not stained with iodine. F) The sum spectrum of the elements of the whole region. Scale bars = 5 µm.

3.3.1 Alignment

The first artifact, which was corrected before the segmentation of the LCN, was the misalignment of the images. The FIB-SEM images are usually not well-aligned as a result of the shrinkage of the sample when it is dehydrated in the vacuum, or because of the bending of the electron beam when it is colliding a charge gradient in the material [159]. An in-house Python script (Version 3.7, Python Software Foundation, Delaware, United States) was developed in which the "Oriented FAST and Rotated BRIEF (ORB)" algorithm was used to align the images. With this algorithm, FAST (features from accelerated segment test) works as the locator that identifies the key points on the image. Edges and corners of the image components are good examples of key points, as they are unique. On the other hand, BRIEF (Binary Robust Independent Elementary Features) is applied as the descriptor to describe the key points [27] for matching the images.

3.3.2 Denoising

Random noise is another image artifact that presents in many imaging methods, such as Atomic Force Microscopy (AFM), scanning electron microscopy (SEM), synchrotron X-ray tomographic images, and Focused Ion Beam nanotomography [160]. Various imaging parameters/conditions, such as complex electronics, heating, or signal amplification [161], can contribute to the increased noise level. In this study, a "total variation Chambolle Denoising" algorithm was used to denoise backscattered electron images. This algorithm works based on minimizing the total variation of the image, which is advantageous over algorithms such as linear smoothing or median filtering because it preserves edges and does not smooth them [162]. Fig. 3.6.B shows the backscattered electron image after denoising with this algorithm.

3.3.3 Destriping

Striping (also called curtaining) is another artifact occurring while milling with FIB. Striping is usually the result of an uneven surface, heterogeneity of the material, different crystal orientations, or underdose of the ion beam [28]. In this work, striping was observed mostly in the mineralized matrix, probably because of an underdose of the ion beam for such a hard tissue. A well-known way for destriping images is using Fourier transform and deleting the corresponding components of stripes in the transformed image [163]. The primary issue with this method is that usually, the components of the main signal in the transformed image are mixed with the components of stripes, and deleting the latter will cause loss of the signal after the inverse transform of the data. Therefore, an algorithm has been proposed that combines the Fourier transform with wavelet decomposition to minimize the loss of signal [164]. This algorithm also occupies less memory space and computer time in comparison to the Fourier transform algorithm [165]. Wavelet decomposition is a method that decomposes an image into its horizontal, vertical, and diagonal components. In the combined algorithm, the Fourier transform is applied to the vertical decomposed component to

remove vertical stripes. The decomposition and transformation continue until no discernable stripe exists in the vertical components. In this work, an in-house Python script, combining wavelet decomposition and Fourier transform algorithms was used to destripe FIB-SEM images. Fig. 3.6.C shows the image after destriping.

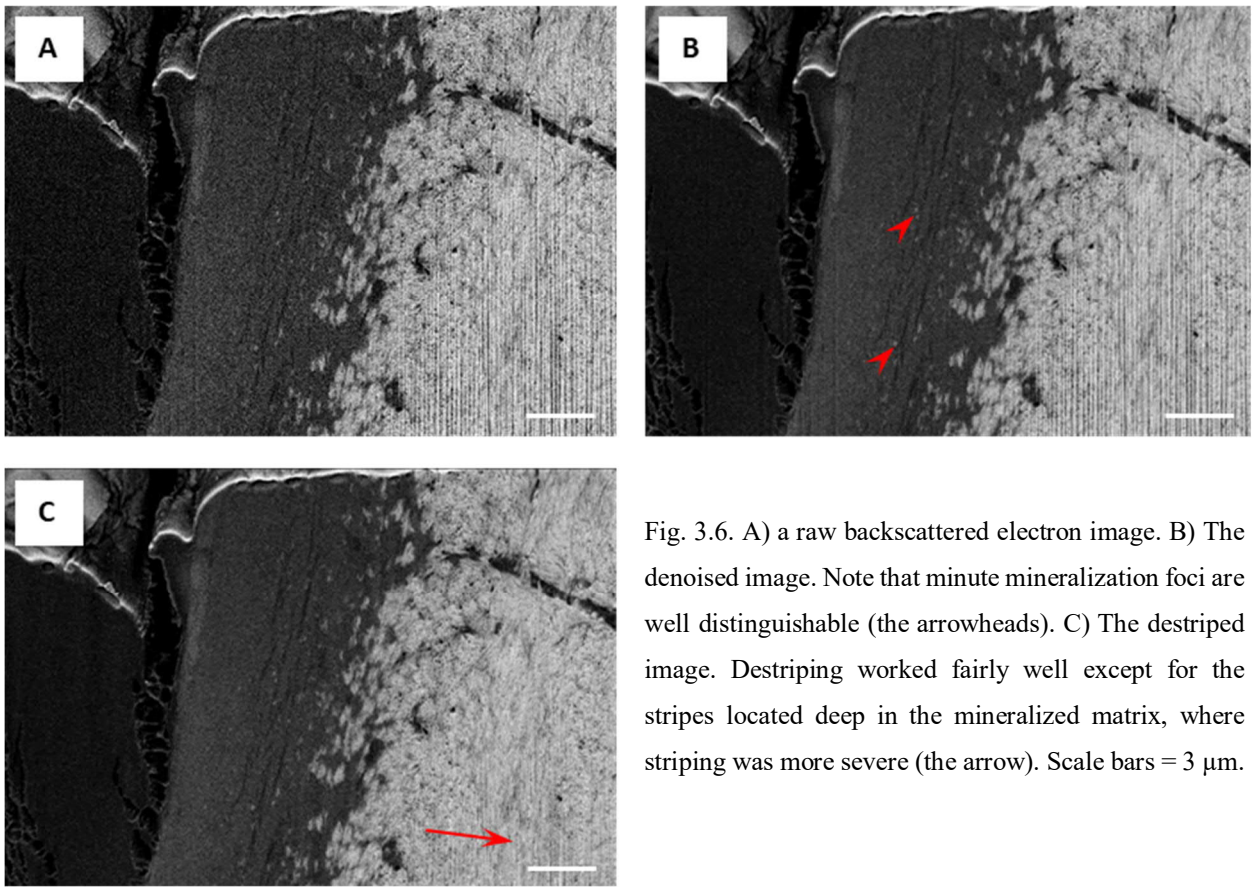

Fig. 3.6. A) a raw backscattered electron image. B) The denoised image. Note that minute mineralization foci are well distinguishable (the arrowheads). C) The destriped image. Destriping worked fairly well except for the stripes located deep in the mineralized matrix, where striping was more severe (the arrow). Scale bars = 3 µm.

3.3.4 Segmentation of the Haversian canal and the LCN

After removing image artifacts, the Haversian canal and the LCN were segmented. Segmentation was conducted on the FIB-SEM dataset with Amira (Version 2019.38, Zuse Institute Berlin (ZIB), Berlin, Germany) to benefit from 3D visualization of the osteocyte network and also to provide references of distance to analyze the mineralization variation with respect to distance from the Haversian canal and the LCN. Thanks to the iodine staining and the image processing, canaliculi were distinguishable in both unmineralized and mineralized matrix. As PMMA was not stained with iodine, three distinct peaks in grey value histogram are visible, which are attributed to PMMA, unmineralized bone tissue, and mineralized tissue (Fig. 3.7.A). The first peak, which relates to PMMA, is representative of the Haversian canal and the LCN with grey values between 0 and 30. Segmentation, however, was performed manually with the “brush”

tool in Amira based on the shape of the LCN and the Haversian canal. This approach was used because different automatic thresholding algorithms, including machine learning, were applied, but they failed to come to a result as good as manual segmentation. It might be owing to variations in image quality, brightness, and contrast, and due to the presence of microcracks, which were similar to canaliculi in shape.

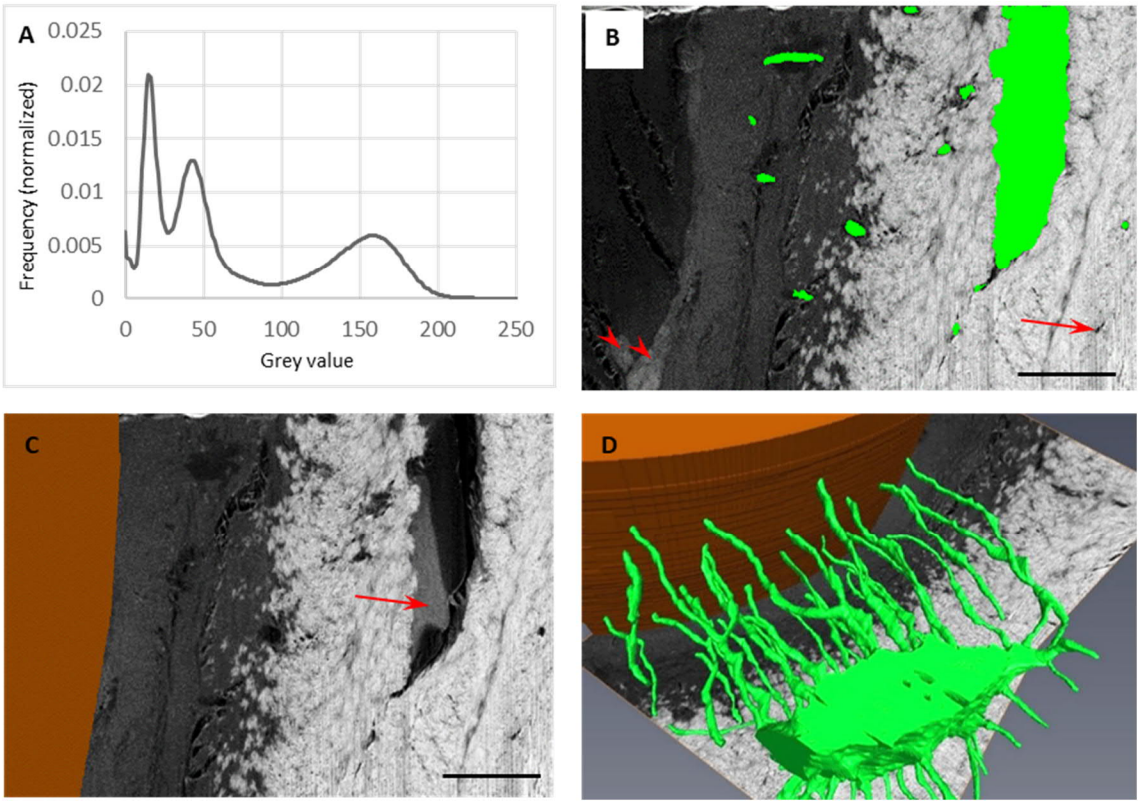

Fig. 3.7. A) The histogram of the frequency of voxel's grey values of one dataset of sample FM48, osteon #2 (left peak: PMMA, middle peak: unmineralized matrix and right peak: mineralized matrix). B) A 2D segmented backscattered electron image of the LCN (green). The arrow shows a microcrack (which is similar to the cross-section view of a canaliculus), and the arrowheads show organic remnants inside the Haversian canal. C) A 2D segmented backscattered electron image of the Haversian canal (brown). The arrow shows an organic remnant inside the lacuna. Microcracks and organic remnants (stained with iodine) were disregarded in the segmentation. D) 3D rendering of the LCN and the Haversian canal. Note that cutting planes are perpendicular FIB-SEM backscattered electron images. Scale bars = 5 µm.

In manual segmentation, every round dark spot in the image with about eight pixels in diameter (~300 nm), which was connected to the lacuna or other canaliculi, was segmented as a canaliculus. Artifacts like microcracks similar to the canaliculi in shape were disregarded (see the arrow in Fig. 3.7.B). Another issue in the segmentation was the presence of stained organic remnants. Iodine, which was used for enhancing Z contrast of unmineralized matrix, led to staining of other organic tissues (see the arrowheads in Fig. 3.7.B

and the arrow in Fig. 3.7.C). Therefore, segmentation of the Haversian canal and the LCN was also conducted with the "brush" tool. As the brightness of the stained organic remnant was different from both the unmineralized and mineralized matrix, the lacuna/mineralized matrix and the Haversian canal/unmineralized matrix interfaces were clearly distinguishable for segmentation. To do the segmentation in a reasonable time, the LCN in every five slices was segmented first, and then the slices in between were segmented by interpolation. The Haversian canal and the LCN were segmented in different colors to perform spatial correlation analysis with respect to both. Fig. 3.7.B and C show a 2D segmented image of the LCN and the Haversian canal, respectively, and Fig. 3.7.D shows a 3D rendering of the LCN and the Haversian canal at mineralizing tissue.

3.3.5 Distance transform of the image stacks with respect to the Haversian canal and the LCN

After segmenting the Haversian canal and the LCN, distance maps were calculated in which each voxel's grey value represents its distance (in 3D) to the nearest segmented surface. For this, the "Exact signed Euclidean Distance Transform (3D)" plugin was used in FIJI (National Institutes of Health, USA). Distance transform is widely used in computer science, e.g., for pattern recognition and image analysis [166]. The input dataset for this transform should be a binary dataset in which the segmented components take value zero. Fig. 3.8 shows the binary image and distance map with respect to the LCN and the Haversian canal.

3.3.6 Data analysis; development of a correlation between the grey values of FIB-SEM images and distance maps

After the acquisition of datasets, segmentation of the Haversian canal and the LCN, and calculation of the 3D distance maps, the development of an analytical tool was necessary to quantitatively correlate grey values of voxels to their corresponding distance values from the Haversian canal and the LCN. The most common way to study the correlation is simply to use linear regression and report the R^2 and p-values to indicate how well two parameters correlate. A second comparable but slightly more advanced approach commonly used is non-linear regression. The major disadvantage of fits is that statistical distributions are not visible in a single line. Another drawback of both linear and non-linear fitting is that the fitted line is forced to follow the given model. In this study, however, a spatial correlation was utilized, which was a powerful tool for mapping relationships. For this, first, the 2D histogram was plotted with the distance values on the x-axis and the grey values on the y-axis that provides the distribution of voxels with respect to the distance and grey values. Afterward, the 2D histogram was divided into smaller bins containing a certain number of voxels. The x-axis bin size was 67 nm (~1.5 times the voxel size), and the y-axis bin size was 1 (out of 256, due to the 8-bit nature of the SEM images that range from 0 to 255). With the help of

Alexander van Tol (MPIKG, Potsdam, Germany), a Python script (Python Software Foundation, Beaverton, USA) was written based on a Numpy function that counts the number of voxels ($m_{i,j}$) in each bin in which i and j are representative of the bin position in the 2D histogram in x and y directions respectively. Fig. 3.9.D shows a 2D histogram with $m_{i,j}$ (shown by dots) for the bins.

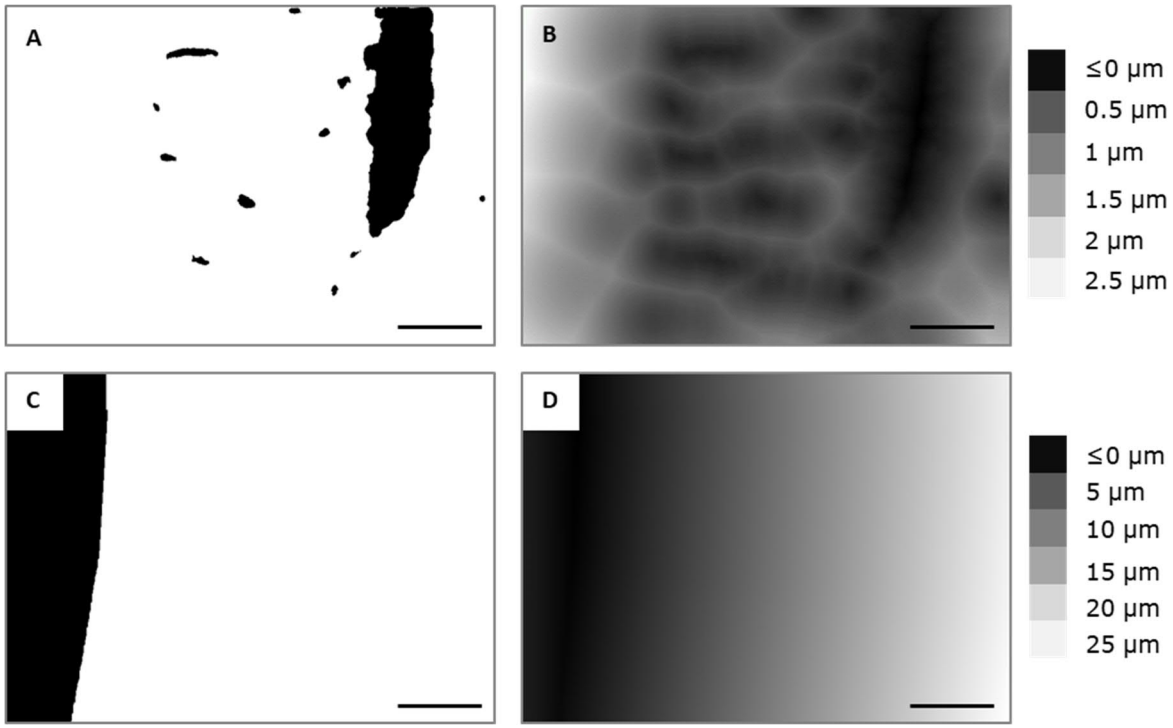

Fig. 3.8. Distance maps with respect to the LCN and the Haversian canal. A) The binary image of the LCN and the surrounding matrix. B) The correlated distance map with respect to it. C) The binary image of the Haversian canal and the surrounding matrix. D) The correlated distance map with respect to it. Note that distance maps shown here are single images of a 3D distance map. Grey values in the distance maps show the distance of the matrix from the nearest segmented surface. The brighter the voxel is, the further away from the correlated surface it is. Scale bars = 5 µm.

Considering the geometry of the canaliculi, the number of voxels at a defined distance increases by receding from the center of the canaliculi. Particularly for cylindrical canaliculi, the number of voxels at a certain distance increases with radius (r). Fig. 3.9.A shows an artificial example in which a canaliculus (green circle) is surrounded by a matrix with Gaussian noise around the grey values 50 and 150. Histogram of grey values (Fig. 3.9.B) shows red and blue peaks assigned to the bright and dark voxels, respectively. The histogram of distances (Fig. 3.9.C) shows that the number of voxels increases linearly with radius (circumference = $2\pi r$). Hence, the 2D histogram of grey values and distances (Fig. 3.9.D) confirms that the number of voxels at a specific distance increases with increasing distance to the canaliculus. Therefore, a 2D histogram cannot provide the probability density distribution (PDD) of voxels as it contains information

about the number of voxels. To compensate for the geometry issue, the 2D histogram was normalized based on distance from the LCN. This normalization results in the probability density ($d_{i,j}$) which is defined by:

$$d_{i,j} = \frac{m_{i,j}}{\sum_{j=0}^{255} m_{i,j}}$$

In which, number of voxels are normalized to the sum of the number of voxels at each distance bin (note that i is fixed in the sigma as the sum of $m_{i,j}$ is calculated for the bins at a certain distance bin). Therefore, the PDD is calculated in such a way that the sum of all bins for a given distance bin is equal to 1. Fig. 3.9.E shows the PDD for the artificial example of a canaliculus and its surrounding matrix shown in Fig. 3.9.A. With such a graph, the fraction of voxels at a certain distance can be easily recognized.

After validating the correlation method, the correlation analysis was performed for the FIB-SEM dataset shown in Fig. 3.7.D. For all datasets, the distance transform was computed on the original volumes, but the correlation analysis was considered only on a smaller subvolume to avoid the edge artifacts. Fig. 3.10.A and B show cross-sections of canaliculi and distance map in a subvolume at the mineralization front, respectively. Fig. 3.10.C and D show the normal and normalized 2D histogram of grey values and distances from canaliculi, respectively. Interestingly, after normalization, a different distribution of grey values is visible, which was not recognizable in Fig. 3.10.C. The normalized graph reveals that at small distances from the canaliculi (below ~0.5 µm), the probability density of unmineralized matrix is high, while at further distances from canaliculi (up to ~2 µm), the probability density of mineralized voxels is high. This observation will be investigated in more detail in section 4.4.

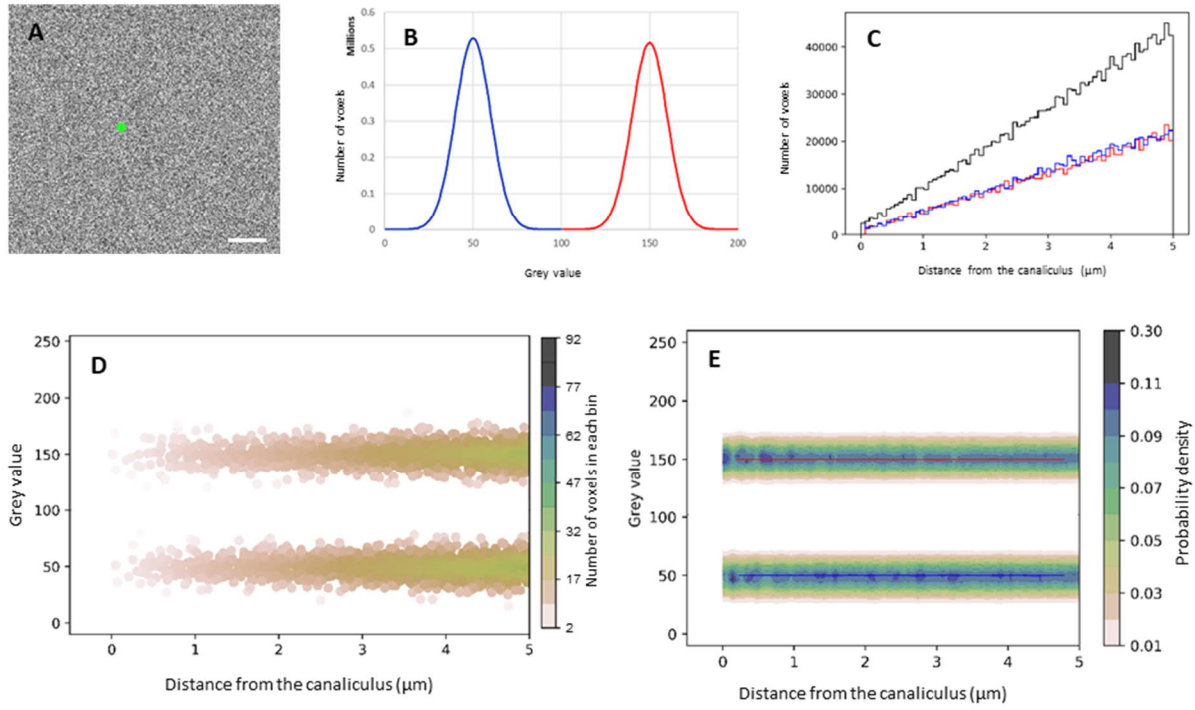

Fig. 3.9. An artificial model of a canaliculus within a matrix with Gaussian noise around the grey values 50 and 150 (A) and the correlated histogram of grey values (B) and histogram of distances (C). The red and blue graphs in the histograms are assigned to the bright and dark voxels, respectively. The black graph in panel C shows the sum of the red and blue graphs. 2D histogram (D) showing the density distribution of voxels in which each dot is representative of $m_{i,j}$ that gives the number of voxels in each bin. Due to the geometry of the canaliculus, density increases with distance. Probability density distribution (PDD), which is a normalized 2D histogram (E), shows the probability density $d_{i,j}$ of bright voxels with average grey value = 150 (red line) and dark voxels with average grey value = 50 (blue line). Note that in such a distribution, the effect of geometry on the distribution of voxels is eliminated. The analyses are shown up to five µm from the surface of the canaliculus. Scale bar = 2 µm.

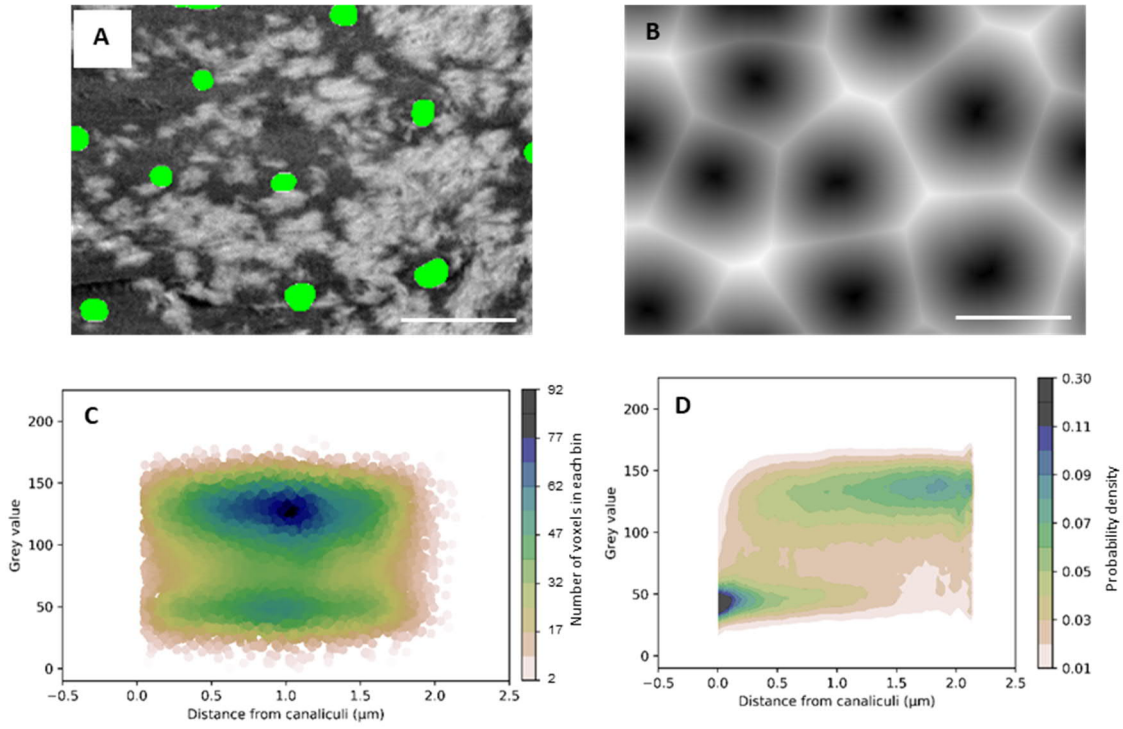

Fig. 3.10. A) A cross-section of canaliculi (green spots) at the mineralization front shown in Fig. 3.7.D. B) The corresponding distance map of Fig. 3.10.A. Note that the distance map is obtained in 3D, and only a single slice is shown here. Brighter regions are representing voxels far away from the canaliculi, while darker regions are representative of voxels near the canaliculi surface or inside them. C) A 2D histogram showing how many voxels with a certain grey value exist at a certain distance from the LCN. The color code shows the total number of voxels at each grey value and distance bin. D) The normalized correlation graph of panel C. The color code shows the fraction of voxels at each grey value and distance bin. Scale bars = 2 µm

Chapter 4

Results

Bone is a dynamic tissue that is remodeled regularly to liberate minerals into the body fluid for mineral homeostasis and also to remove microcracks that could lead to bone fracture. Remodeling rate increases in adults near the onset of menopause due to the hormonal changes. In this process, first, old bone is resorbed, and then, an unmineralized matrix (osteoid) is deposited, which will be further mineralized. The mineralization process is thought to be aided by a dense lacuno-canalicular network (LCN) [6], specifically in the transporting of mineral precursors. The LCN and the mineralization front consist of nanoscale components such as canaliculi and mineralization foci (i.e., tiny, separated mineralization centers in the unmineralized matrix), respectively, that require imaging and characterization techniques with nanometer resolution. In view of the spatio-temporal aspect of mineralization in bone, imaging techniques aimed at understanding the mineralization process should provide 3D information of the transition from the unmineralized to the mineralized bone. To achieve these goals, first, an iodine staining protocol was developed to visualize the unmineralized matrix and the LCN that pervades both unmineralized and mineralized matrices (4.1). This approach was of high importance as so far, based on current literature, no 3D data have been produced to unveil the interplay between mineralizing matrix and the osteocyte network in human bone. After the optimization of staining parameters, FIB-SEM datasets were acquired for the 3D rendering of the LCN as well as the Haversian canal within bone tissue (4.2). These datasets also provided information about the degree of mineralization (mineralized voxels) and iodine staining (unmineralized voxels) that were distinguishable with a grey value thresholding of the backscattered electron images. Afterward, the Haversian canal and the LCN surfaces were selected as the references to obtain the distance maps. Finally, the relationship between grey values of voxels (i.e., the local degree of mineralization) and their distance values (4.3 and 4.4) was quantitatively evaluated by probability density distribution (PDD) graphs. The orientation of collagen fibrils and mineralization foci was also observed and measured thanks to the high-resolution images of FIB-SEM and optimized staining of unmineralized collagenous fibrils (4.5).

4.1 Development of iodine staining for visualization of the unmineralized tissue

For PMMA-embedded samples with unmineralized tissue, it is difficult to differentiate between PMMA and soft tissue as both materials consist of light elements such as H, C, N, and O that have small backscattered electron coefficients [167]. Moreover, when the imaged samples consist of mineralized tissue, PMMA, and unmineralized tissue, because of the huge difference in grey values between mineralized and unmineralized tissues, there is not adequate greyscale resolution to distinguish between different mineralized tissues [168]. To overcome this limitation, soft tissues are often stained with heavy elements-containing chemicals such as uranyl acetate, lead citrate, and osmium tetroxide [169]. Such stains enable

investigators to image details of soft tissues in different biological samples. However, in post-embedding staining protocols, such stains might lead to overstaining of polishing blemishes and also mineralized tissue, which is undesirable [168]. In contrast, iodine, which is another heavy element (Z = 53), is advantageous for staining of archival samples that are not fresh and are permanently preserved in PMMA, without causing the issues mentioned above [168].

Iodine staining is typically conducted in liquid or gaseous phase (dry) for the staining of soft tissue. The liquid staining protocol is performed with the so-called Lugol solution in which potassium iodide and elemental iodine are dissolved to form triiodide ion [170]. Bone, cartilage, and muscle tissues have been stained using this protocol for backscattered electron imaging and Micro-CT [168, 171]. The dry protocol relies on gaseous iodine, which is advantageous to avoid problems associated with wetting of specimens, such as specimen shrinkage [172] and pooling around cracks and defects [155] that causes overstaining and consequently higher backscattered signal. In this study, an optimized dry protocol of iodine staining was established for visualization of the unmineralized tissue (osteoid) in the forming osteons of PMMA-embedded human osteonal bone. For this, at first, preliminary tests involving saturated iodine vapor were conducted (section 4.1.1). These tests led to overstaining of the surface and lack of staining in the first 25 µm below the polished surface of the sample. These issues were overcome using an optimized protocol in which the amount of iodine added over time in the reaction was adjusted to keep the atmosphere always slightly undersaturated (4.1.2). It was further found that laser irradiation has a detrimental effect on the staining if it is conducted before adding iodine. This is particularly important and should be taken into account in those cases where confocal microscopy imaging is involved (section 4.1.3).

4.1.1 Preliminary test

Gaseous Iodine (I_2) was used (Fig. 4.1.A) to stain unmineralized collagenous tissues in PMMA-embedded bone samples following the method proposed by Boyde *et al.* [155]. I_2 diffuses into the samples, and it can be reduced to iodide and triiodide. There it can form ionic bonds with cations [155] and might react with carbon-carbon double bonds of unsaturated molecules in the soft tissue to form organoiodine compounds. Therefore, when these reactions are taking place, the average atomic number of the regions abundant in soft tissues increases, and consequently, the Z contrast of backscattered electron imaging is enhanced. Considering the phase diagram of iodine (Fig. 4.1.B), the solid sublimates to vapor at room temperature. Therefore, to have a gaseous phase of iodine, 50 mg [155] solid iodine (Alfa Aesar, Karlsruhe, Germany) were put in a 25 ml glass container together with the sample for one week. The container was sealed with Polytetrafluoroethylene (PTFE) tape. Immediately after incubation, the color of the gaseous atmosphere around the sample changed to pink, which is an indication of iodine sublimation.

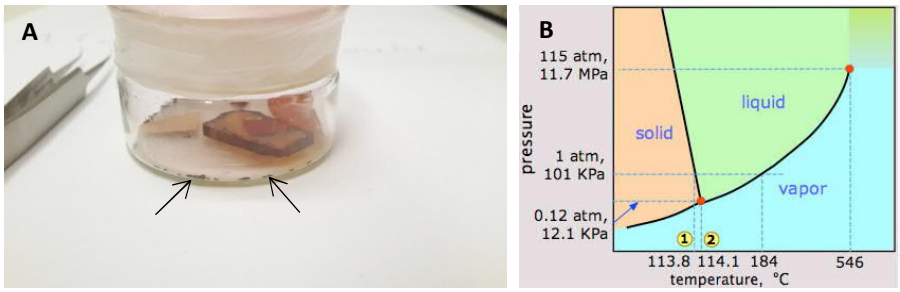

Fig. 4.1. A) Iodine staining of PMMA-embedded samples. Iodine particles (the arrows) were put inside the container to sublimate into vapor and stain the unmineralized matrix. The pink color of the atmosphere around the sample is iodine vapor. B) Phase diagram of iodine. At room temperature, iodine undergoes a solid-vapor phase transition. Reprinted with permission from [173].

To verify staining protocol efficiency, the sample was imaged with environmental electron microscopy (ESEM) and focused ion beam-scanning electron microscopy (FIB-SEM). The ESEM images of the sample block surface (Fig. 4.2.A) show that, after one-week staining, the contrast between the mineralized matrix and osteoid vanished. FIB-SEM investigation of a cross-section of the same region (Fig. 4.2.C) revealed that a thin layer on the surface (~3 µm) was overstained with iodine (the red arrow in Fig. 4.2.C). This homogeneous, iodine-rich layer at the surface of the sample is responsible for the vanishing of contrast in the ESEM images. Despite being overstained at the surface, most of the osteoid below the surface was not stained and still lacked backscattered signal. From these two observations, it was concluded that iodine was excessively used, and the time of staining was not sufficient for iodine to reach regions deeper in the tissue.

4.1.2 Optimized protocol

The FIB-SEM image of the preliminary test of iodine staining showed the accumulation of the iodine on the surface of the sample. 50 mg of iodine was therefore deemed excessive, as it apparently kept the staining atmosphere at the saturation vapor pressure of iodine during the entire incubation time. Fig. 4.3.A schematically shows the vapor pressure of iodine with respect to the time of staining. It is speculated that this constantly saturated iodine vapor in contact with the surface of the sample causes an initial excessive surface accumulation of iodine that prevents more vapor from diffusing into the tissue. A similar effect was observed by Boyde with Lugol solution, where it was seen that higher concentrations of iodine ions in solutions led to overstaining of the tissues [168]. In contrast, when a lesser amount of iodine was added to maintain the atmosphere under the saturated vapor pressure, the partial pressure of iodine decreased over time, and a smaller volume of iodine in total could diffuse through the sample (Fig. 4.3.B).

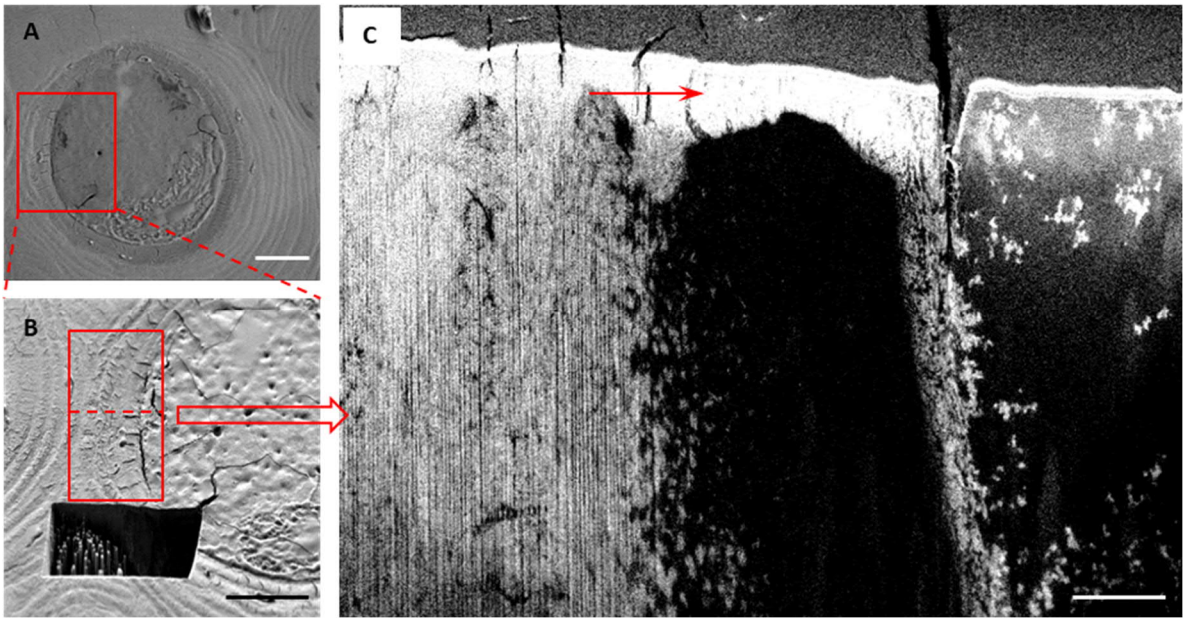

Fig. 4.2. The preliminary test of iodine staining with an incubation time of one week and 50 mg solid iodine. A) ESEM image of a forming osteon, B) SEM picture of the same osteon milled with FIB ready for slice and view (red rectangle). The dashed line shows the slice from which the backscattered electron image was taken. C) Backscattered electron image of one slice with three regions; mineralized matrix (left), unmineralized matrix (middle), and PMMA (right). The red arrow shows the overstained layer of osteoid. Scale bars for A and B = 50 µm and C = 5 µm.

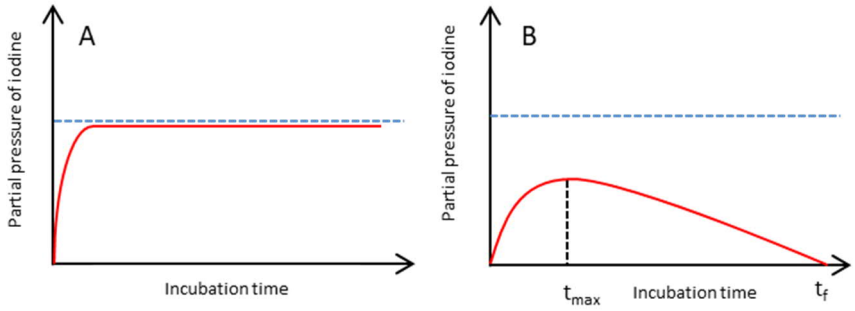

Fig. 4.3. Variations in vapor pressure of iodine with time. The Blue dashed line shows the saturated vapor pressure. A) The red line shows the vapor pressure of iodine that exists in the container. It is equal to vapor pressure at saturation because an excessive amount of solid iodine was used, so the vapor was in equilibrium with the solid during staining. B) The red curve shows the variation of iodine vapor when a controlled amount of iodine (below saturation point) was added. Up to t_{max}, vapor pressure is gradually increasing because of the presence of the solid iodine in the container. After t_{max}, when all of the solid iodine is evaporated, vapor pressure starts to decrease and reaches zero at t_f.

Therefore, to provide vapor pressure similar to what is schematically depicted in panel B of Fig. 4.3, the minimum amount of iodine that produces a saturated vapor pressure was calculated. It was assumed that iodine vapor and air inside the container create an ideal gas mixture. According to Dalton's law of partial pressures, the following equation is obtained:

$$P_A = X_A\, P$$

in which P_A is the partial pressure of component A in a gas mixture with two components, X_A is the mole fraction of A, and P is the total pressure. Partial pressure is the product of the mole fraction of a gas component and the total pressure of the gas mixture for ideal gases [174].

Considering $X_A = \frac{n_A}{n_A+n_B}$ in which n_A = moles of A and n_B = moles of B, the following equation is derived:

$$P_A = \frac{n_A}{n_A + n_B}\, P$$

Given that P is 1 atm, P_A is the partial pressure of iodine at 25 °C in air saturated with iodine, which is 0.305 mmHg (0.0004 atm) [175] and n_B is the number of moles of air in a 25 ml container. Assuming n_A + n_B = 0.0011 moles, n_A (which is the moles of iodine at saturation) is calculated as 4.42×10^{-4} mmole in saturation. By multiplying with the molecular weight of iodine (I_2, 253.8089 g/mole), the amount of iodine that sublimates to vapor and produces saturated vapor pressure is calculated, which is 0.11 mg. Therefore, to stay below the saturation point to avoid overstaining of osteoid, ~0.1 mg solid iodine within six days of incubation time was used. After four days, all of the solid iodine evaporated. This provides an approximation of the average iodine sublimation rate of $0.01\times$n mg.h^{-1} (in which n is the mass of iodine used in milligram). It is also estimated that with the 50 mg of iodine in the preliminary test, the atmosphere reaches saturation in about 12 min.

To ensure that the iodine gas would diffuse a large distance through the sample below the surface of the block, the cycle was repeated. After two staining cycles, the staining was validated by ESEM and FIB-SEM. Fig. 4.4 shows a typical forming osteon exhibiting an active mineralization front. It is observed in ESEM images that after staining, the grey value of osteoid increased, and the contrast between mineralized

and unmineralized matrix decreased. However, at the end of the staining procedure, the two regions still maintained distinct grey values. The FIB-SEM image (Fig. 4.4.D) nicely shows three ranges of grey values for PMMA (including lacuna and canaliculi in black), unmineralized matrix (including unmineralized collagenous fibrils in grey) and mineralized matrix (including mineralization foci and fully mineralized matrix in white).

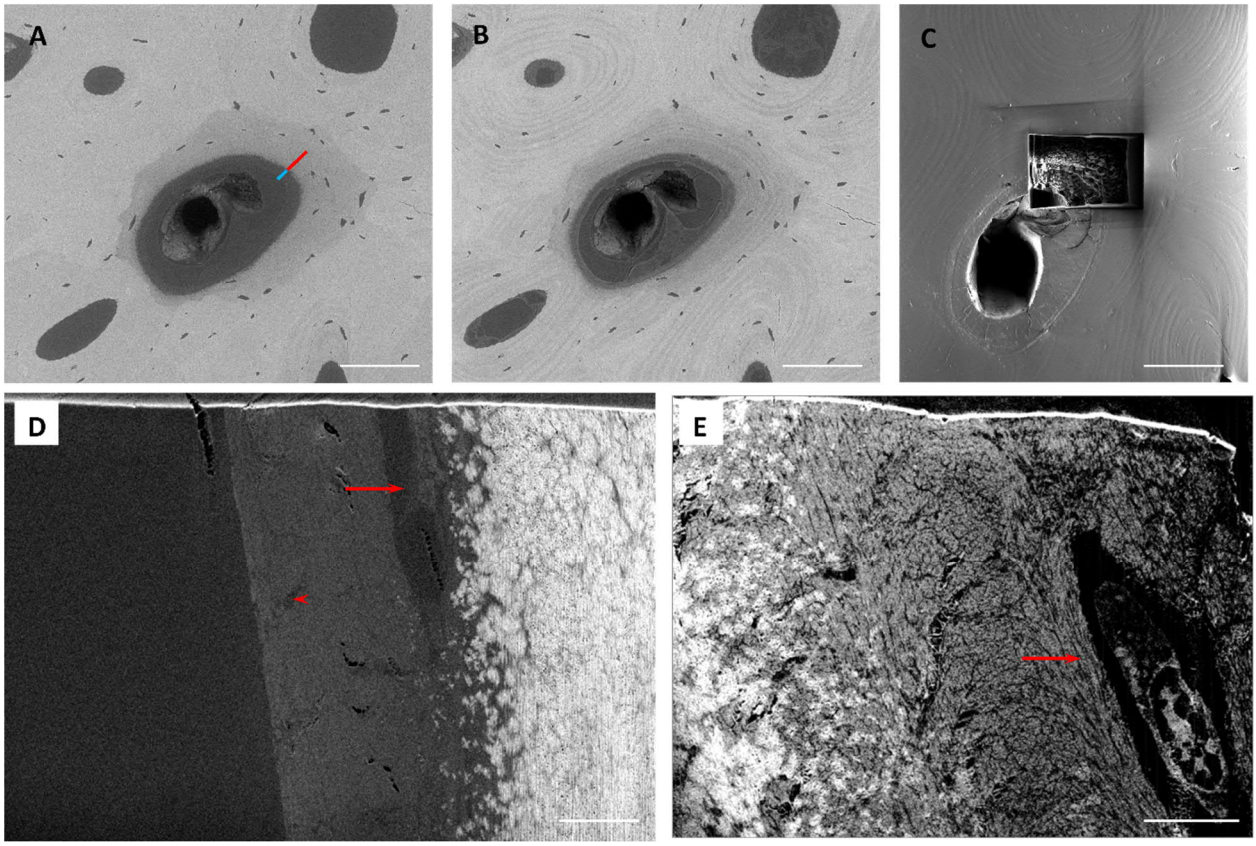

Fig. 4.4. Validation of optimized iodine staining of osteoid with ESEM and FIB-SEM. A) A typical forming osteon before staining with an unmineralized region (the blue bar) and a mineralized region around it (the red bar). B) The same osteon after two cycles of staining with 0.2 mg iodine and ten days of incubation time. C) FIB image of the milled ROI after slice and view. D) A backscattered electron image from the FIB-SEM dataset. The unmineralized collagenous matrix is homogeneously stained, and the osteocyte lacuna (the arrow) and a canaliculus (the arrowhead) are visible. E) A backscattered electron image from the FIB-SEM dataset of another sample, which is stained for a longer time (35 days). Apparently, longer incubation time leads to better staining in a way that even collagen fibrils around the lacuna are distinguishable. Scale bars for A, B and C = 100 µm, D and E = 5 µm.

These results show that the major parameter to be considered when performing iodine staining of soft tissue, specifically osteoid, from the gas phase is the vapor pressure produced by the solid I_2. It is critical to adjust the amount of solid to the volume of the staining vessel to ensure that the vapor pressure, at the beginning

of the staining procedure, is set below the saturation point. The other effective parameter is the incubation time, i.e., a longer time might contribute to deeper staining since some of the iodine molecules might remain in the sample with no reaction until they reach the carbon-carbon double bonds located at the deeper sites. Moreover, as the iodine reacts reversibly with many organic molecules [176], it might cause the bound iodine at the surface to release again, diffuse deeper, and react with carbon-carbon double bonds. One FIB-SEM dataset of a forming osteon, which was stained for a longer time (35 days), exhibits a better stained unmineralized matrix in which even the collagen fibrils are distinguishable (Fig. 4.4.E). However, since only one dataset is available for such a long protocol, further experiments should be performed in the future to determine the exact effect of time on iodine staining.

4.1.3 Effect of laser irradiation on iodine staining of the unmineralized tissue

To visualize the LCN in 3D and large fields of view, the samples were imaged with confocal laser scanning microscopy (CLSM). For some of the samples, CLSM was conducted before iodine staining, while for some others, it was performed after iodine staining. Fig. 4.5 shows FIB-SEM images of different osteons in different samples. For the osteon that was stained with iodine before performing CLSM, the staining of osteoid is homogeneous, and the mineralized matrix is easily distinguishable from the unmineralized matrix and PMMA (Fig. 4.5.A). In contrast, those osteons which were iodine stained after performing CLSM show overstaining of osteoid (Fig. 4.5.B and Fig. 4.5.C) and heterogeneous staining of the unmineralized matrix (Fig. 4.5.D).

According to the studies in which alterations of collagen structure, composition [177] and covalent bonding in laser-treated tissues were observed [178], it is speculated that the high power of the laser might produce more carbon-carbon double bonds for iodine to react to and therefore more intense staining in laser-irradiated samples is observed. It is known that iodine ions such as iodide and triiodide can react with cations and carbon-carbon double bonds of unsaturated molecules in the soft tissue [155]. Particularly, by imaging tissues with a laser, some parts of the organic components of the matrix are partially “burnt” and delocalized double bonds could form. It might also be possible that during high power laser irradiation, collagen can be partially transformed into amorphous carbon that provides more sites for iodine reaction with delocalized carbon-carbon double bonds.

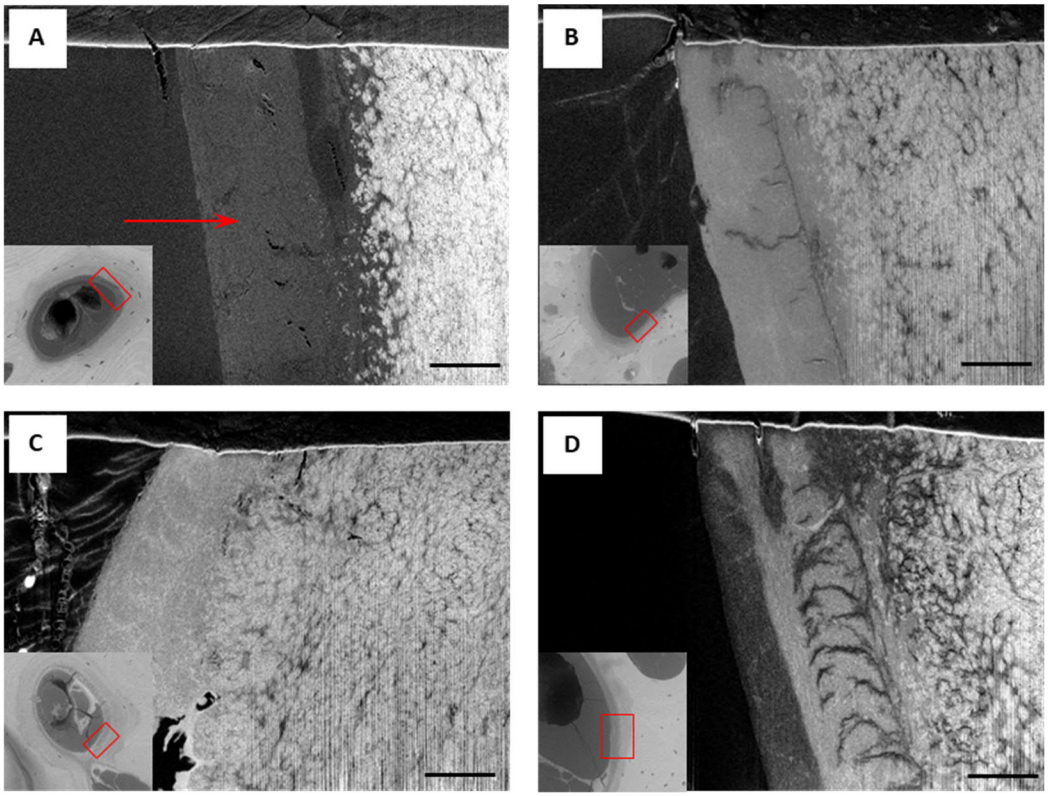

Fig. 4.5. Effect of CLSM on iodine staining of osteoid. A) An osteon which was homogeneously stained with iodine before performing CLSM. The stained osteoid located between PMMA and the mineralized region is visible by the red arrow. B, C, and D) Three different osteons, which were imaged with CLSM and then stained with iodine. Osteoid in these three osteons has been affected by laser and overstained with iodine afterward. Red rectangles show the regions which were sliced and imaged with FIB-SEM. Scale bars = 5 µm.

4.2 3D visualization of bone at the nanoscale

For visualization of the LCN, three major techniques are currently used to provide 3D information. These techniques are 1) focused ion beam-scanning electron microscopy (FIB-SEM), 2) confocal laser scanning microscopy (CLSM) and 3) X-ray computed tomography (CT) (see section 2.5 for details of the methods). Briefly, FIB-SEM and CT (notably nano-CT) provide images with a few nanometer resolution and small fields of view (~100^3 μm^3), while CLSM provides a few hundred nanometer resolution images with much larger fields of view (~1 mm^2 and ~40 µm in depth). Moreover, with backscattered electron imaging mode of FIB-SEM or nano-CT, in addition to resolving the LCN, information of the mineralization degree of the matrix is also obtained. Therefore, correlative imaging of bone with CLSM and FIB-SEM can provide useful data for fast selection of ROIs, visualization of the LCN in large fields of view and assessment of essential phenomena in bone such as mineralization. For this goal, first, the ROIs with ESEM and CLSM

were selected (4.2.1). Then FIB-SEM datasets were acquired, and the LCN was visualized by 3D rendering using Amira, i.e., an image processing software (Version 2019.38, Zuse Institute Berlin (ZIB), Berlin, Germany) (4.2.2). Afterward, a thresholding method was developed to distinguish between unmineralized and mineralized matrices of bone for further investigation of the mineralization process (4.2.3).

4.2.1 Selection of regions of interest (ROIs) using environmental scanning electron microscopy (ESEM) and confocal laser scanning microscopy (CLSM)

To fulfill the aim of this study, which was the visualization and characterization of bone forming tissue and its relationship to the LCN, two primary criteria for the selection of ROIs were defined. First, the selected bone tissue should be composed of both the unmineralized and mineralized matrix. Second, there should be a dense LCN in the selected region. It was also considered that the region should be entirely located within an osteon to ensure that the imaged mineralized matrix belongs to the measured osteon and not to a neighboring one. Two imaging techniques, namely ESEM and CLSM, were used to guarantee that the criteria mentioned above were met. ESEM was a handy instrument to image the surface of uncoated samples, mineralized and unmineralized tissues, and to verify the effectiveness of iodine staining. Fig. 4.6.A shows the ESEM overview of sample FM48 from which three osteons were selected (see chapter 8 for overview images of other samples). On the other hand, CLSM was employed to visualize the LCN buried below the surface inside the unmineralized and mineralized tissue. The laser intensity was adjusted to image canaliculi in the mineralized tissue. At higher laser power, one could image the canaliculi network in the fully mineralized matrix, whereas the osteoid region was oversaturated, as shown in Fig. 4.6.C. By using lower laser intensities, as shown in Fig. 4.6.D, the unmineralized region of the osteoid near the Haversian canal can be more clearly investigated, but the details of the canaliculi network in the mineralized regions are now lost. Therefore, both approaches were applied to image the LCN in the mineralized matrix and to see osteoid around the Haversian canal. The correlative imaging (ESEM-CLSM), enabled visualization of the bone tissue with backscattered electron images of ESEM and the LCN with the CLSM in the same region. Consequently, an ROI was selected for FIB-SEM imaging that comprised the unmineralized matrix and the canaliculi network (red rectangle in Fig. 4.6.B).

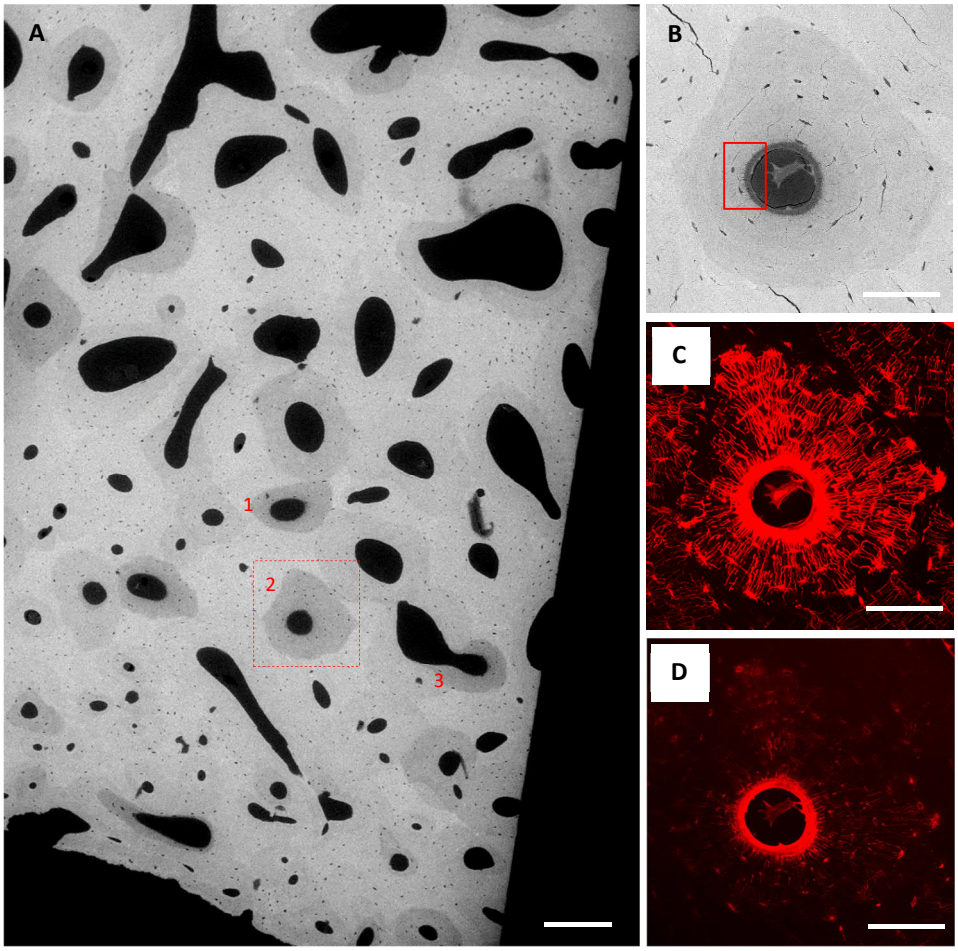

Fig. 4.6. A) ESEM overview of sample FM48 from which three forming osteons were selected (dashed square shows osteon #2). B) The ESEM image of osteon #2 in higher magnification and the ROI (the red rectangle). The selected ROI was used for FIB-SEM imaging afterward. C) The CLSM image of the same osteon. Note the dense LCN in this region. The layer thickness for the CLSM dataset was 0.38 µm, and the final depth of imaging was 50 µm. D) The CLSM image with lower laser intensity, showing osteoid and the canaliculi adjacent to it. Scale bars for A = 250 µm, B, C and D = 100 µm.

4.2.2 FIB-SEM imaging of the forming osteons and 3D rendering of the LCN and the Haversian canal

After finding the ROIs, FIB-SEM imaging was employed to acquire 3D high-resolution datasets. Fig. 4.7.A shows a cross-section of the FIB-SEM dataset, parallel to the surface of the sample, located 6 µm below the surface. Similar to the ESEM image (in the inset), three main phases (PMMA, mineralized and unmineralized tissues) are visible. At the interface of the mineralized and unmineralized tissues, the

mineralization front with newly mineralized foci as small as ~200 nm is observable. In the mineralized matrix, an osteocyte lacuna (the red arrow) and many canaliculi pervading the matrix (dark spots, like those indicated by the arrowheads) can be observed. The 3D rendering of the segmented components from high-resolution FIB-SEM stacks is shown in Fig. 4.7.B and Fig. 4.7.C (top and side view, respectively). The Haversian canal is represented in brown and the LCN in green.

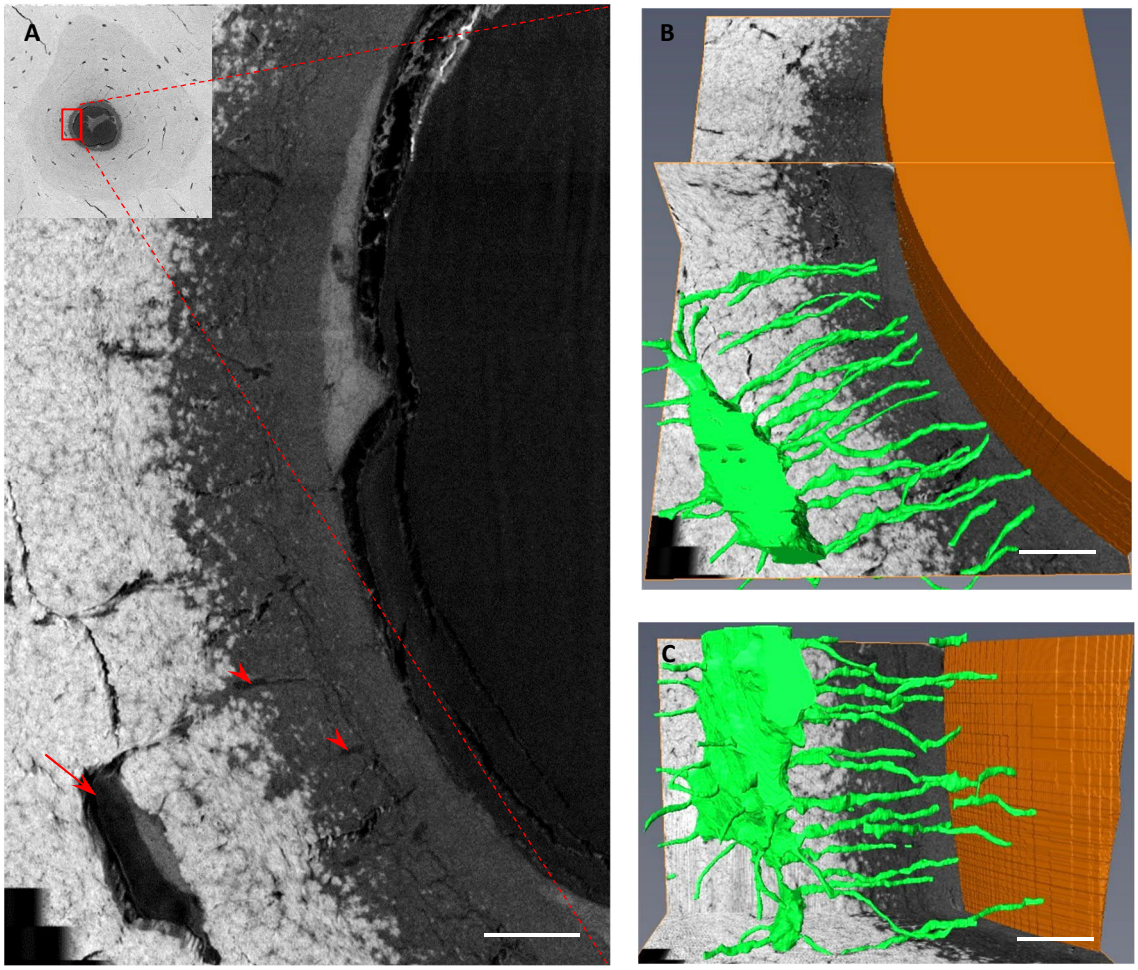

Fig. 4.7. A) A FIB-SEM backscattered electron image of the ROI selected from the ESEM image (inset). The arrow shows an osteocyte lacuna, and the arrowheads show canaliculi. B) The top view of the 3D rendering of the Haversian canal (brown) and the LCN (green) which are located within bone tissue. C) The side view of the same region. Scale bars for A, B, and C = 5 µm.

4.2.3 Thresholding of the three phases of the forming osteon

To quantitatively discriminate the three phases shown in Fig. 4.7.A, the histogram of the grey values was plotted (Fig. 4.8). The histogram shows three peaks, which are representative of the three phases mentioned above. The PMMA phase was segmented out, as explained in section 3.3.4. For the other two phases, two thresholds were defined to separate mineralized and unmineralized matrices and to analyze these tissues based on their grey values. One single threshold might not be sufficient because some of the voxels are at the interface of the mineralized and unmineralized phases (such as the voxels at the boundary of mineralization foci), which cannot be assigned to either the mineralized or unmineralized voxels. One reason for the existence of such voxels is the partial volume effect. This effect appears when the resolution of imaging is comparable to the size of the imaged component. Hence, some parts of the component are visible in other voxels with the incorrect brightness [179].

Moreover, as the histograms of individual osteons were different and peaks positioned differently (see chapter 8), the development of a thresholding method that works appropriately for all osteons was critical. To do this, the standard deviation for each peak was calculated (peaks are separated based on the grey value of minimum frequency). For the mineralized matrix threshold, three times standard deviation was subtracted from the grey value of the maximum frequency of mineralized matrix peak. For the unmineralized matrix threshold, two times standard deviation was added to the grey value of the maximum frequency of unmineralized matrix peak (Fig. 4.8.A). This method for thresholding was used to fulfill the following criteria for all datasets. First, to avoid overlapping of the thresholds, i.e., the mineralized matrix threshold number was not less than the unmineralized matrix threshold. Second, to have the local minimum of the histogram between the two thresholds or near to that window (the yellow double arrow in Fig. 4.8.A). Based on these thresholds, the mineralized matrix (red) and the unmineralized matrix (blue) were colored to validate the thresholding method (Fig. 4.8.B). The remaining voxels (grey values between 72-89) were colored in yellow (~3% of all voxels) and excluded from the analysis. Note that grey values 72 and 89 are the thresholds for the unmineralized and the mineralized matrices, respectively, which are calculated for the sample FM48 osteon #2. See chapter 8 for the thresholds of other datasets.

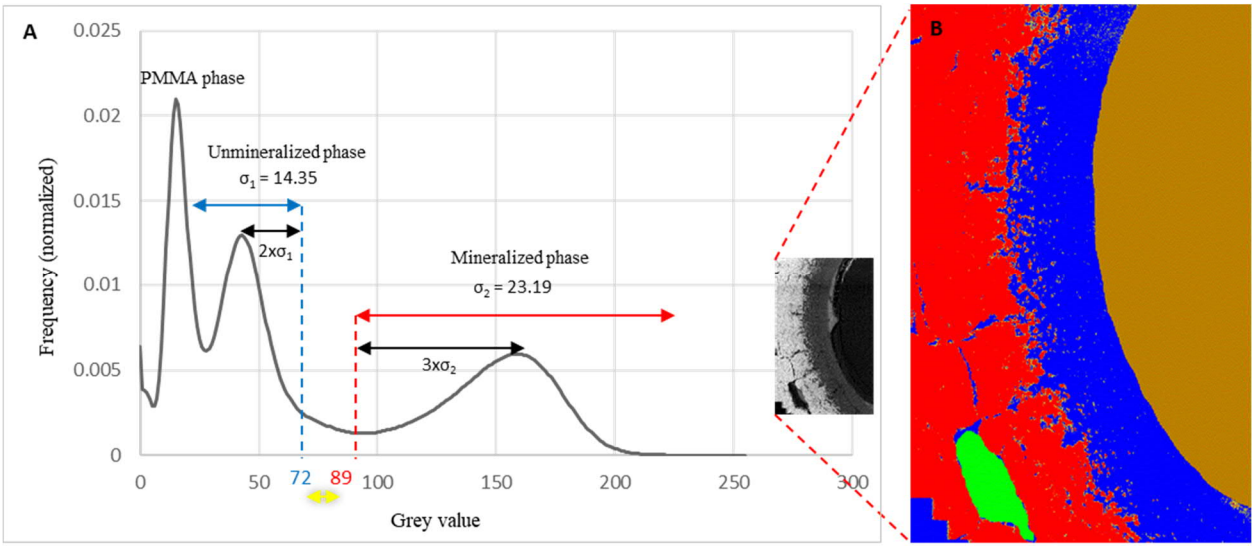

Fig. 4.8. A) Histogram of the sample FM48 osteon #2 with three peaks representative of the three phases (PMMA, mineralized, and unmineralized tissues). Note that the histogram is obtained from the whole 3D stack while a 2D slice is shown. The black double arrows show two and three times standard deviation away from the peak maxima to calculate the thresholds for unmineralized (=72) and mineralized (=89) tissues, respectively. The red, blue, and yellow double arrows indicate mineralized, unmineralized, and mixed tissues, respectively. The inset shows a FIB-SEM image of the dataset. B) The FIB-SEM image colored based on the thresholds; Red is mineralized, blue is unmineralized, and yellow is corresponding to the voxels at the transition zone. The Haversian canal and the lacuna are colored in brown and green, respectively.

4.3 The Haversian canal as a reference for mineralization of bone matrix

The Haversian canal is a microscale canal inside bone that contains blood vessels and nerves. It is part of the vascular system through which mineral precursors are transported [180]. Lining cells and osteoblasts are located at the surface of Haversian canals and are responsible for the secretion of collagen, non-collagenous proteins (NCPs), and matrix vesicles (MVs), which all play significant roles in mineralization [3]. Therefore, considering the Haversian canal as a reference surface of mineralization can give new insight into the mineralization process of forming osteon. For this aim, first PDD graphs with respect to the Haversian canal were plotted to characterize different stages of mineralization in a forming osteon (4.3.1). This analysis was repeated for three osteons of three samples to provide adequate information to compare different stages of mineralization (particularly primary and secondary stages of mineralization) (4.3.2). Afterward, a normalization method was developed to standardize the PDD graphs for different samples for more precise comparison of the parameters such as iodine staining of unmineralized matrix and mineralization front width (4.3.3).

4.3.1 Quantification of unmineralized, transition and mineralized zones

After segmenting the Haversian canal, generating correlated distance maps, and thresholding grey values of bone tissue, the PDD was plotted to identify the correlation between grey values of voxels and their distance to the surface of the Haversian canal. For this, a region with a size of ~20×25×40 μm^3 was selected, and the correlation was analyzed (Fig. 4.9.A).

In Fig. 4.9.B, the PDD of this region is shown. The color code in the PDD graph shows the probability density that varies between 0 and 0.3 (densities in the range of 0 - 0.01 are excluded and shown in white in the PDD graph to avoid a crowded graph) and shows the fraction of mineralized and unmineralized regions at each distance. PDD graph of the Haversian canal displays three zones; a fully unmineralized zone (up to ~4 µm from the Haversian canal surface, where most of the voxels have grey values below 72), a transition, where the probability of the voxels of being assigned to the mineralized phase increases steeply and reaches more than 99% at ~8 µm, and a fully mineralized zone (where most of the voxels are with grey values above 89). Interestingly, an increase in the degree of mineralization is visible between ~8µm and ~17µm as the probability of higher grey values increases.

The distance histograms of unmineralized (blue), mineralized (red), and total (black) voxels in Fig. 4.9.C also demonstrate the existence of the transition zone mentioned above. In Fig. 4.9.D, the volume fraction of mineralized matrix (VFMM) graph is plotted that shows the fraction of mineralized voxels to the total voxels, i.e., the mineralized tissue fraction at each distance. This graph also confirms that bone apposition starts with almost no mineralization up to ~4 µm, continues with formation and growth of foci until ~8 µm, and ends with a fully mineralized matrix.

To track the variation of the average grey value of voxels at different distances, moving average fit curves were plotted for the PDD graphs. The blue, red, and black curves are related to unmineralized, mineralized, and total voxels, respectively. The blue curve, which is almost constant with distance, shows that iodine staining of the unmineralized matrix was homogeneous. The red curve depicts two steps of increase in the degree of mineralization. The first step happens at the mineralization front (transition zone in the PDD graph), where mineralization foci are still separate and not fused together (Fig. 4.7.A). The second stage with a gentle slope, however, is attributed to the fully mineralized matrix and could be the sign of the well-known secondary stage of mineralization in bone [17].

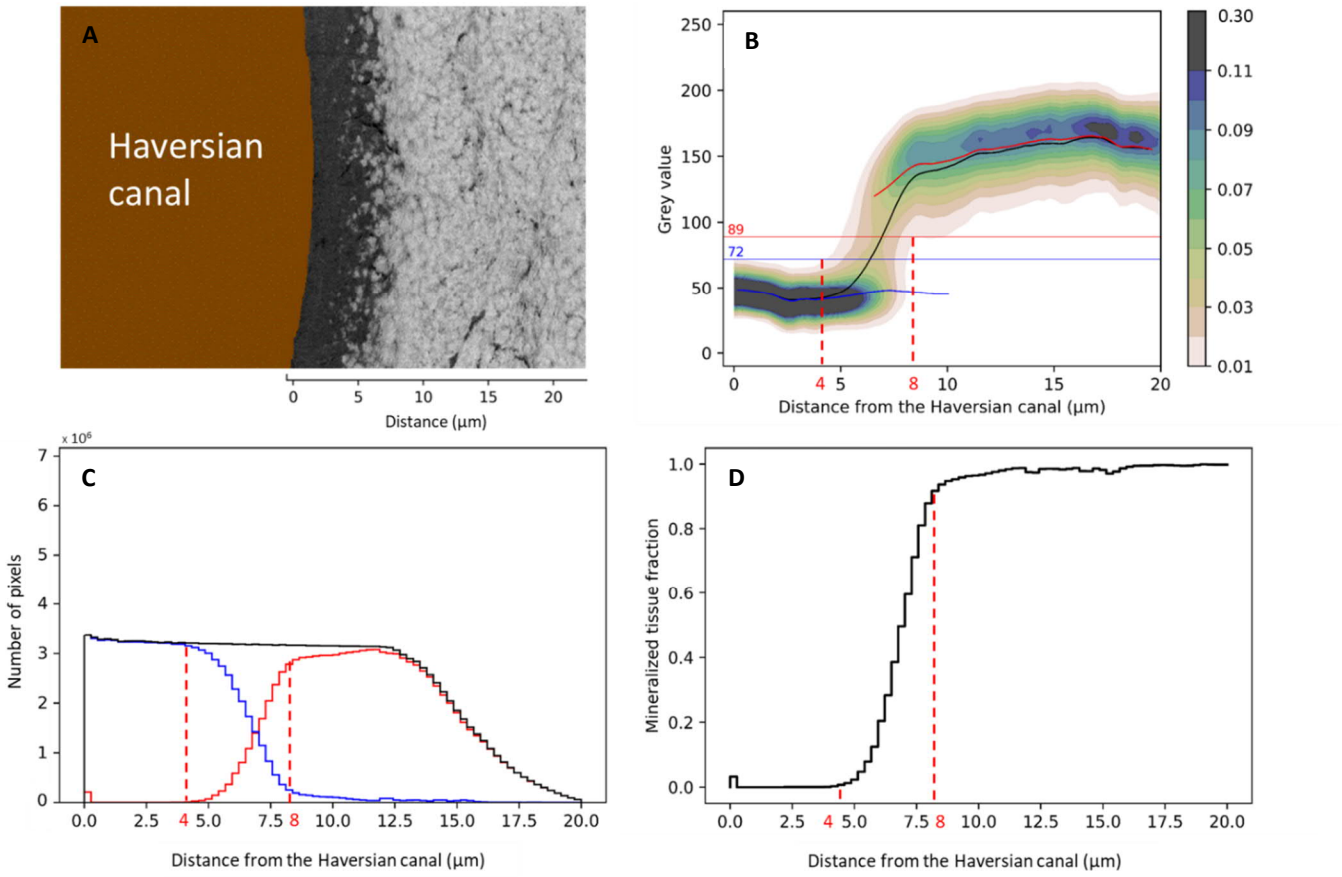

Fig. 4.9. A) A backscattered electron image obtained by FIB-SEM from the ROI of sample FM48 osteon #2. The stack size of the ROI is ~20×25×40 µm^3. Note that the image is representative of a 3D stack from which the following graphs were obtained. B) PDD graph of grey values and distance to the surface of the Haversian canal. Dashed lines separate different zones (fully unmineralized, transition, and fully mineralized zones). The red curve is the moving average fit for mineralized voxels (with grey values above 89), the blue curve is the fit for unmineralized voxels (with grey values below 72), and the black curve is the fit for all voxels. The color code shows the probability density of each grey value at each distance. C) Histogram of unmineralized (blue), mineralized (red), and all (black) voxels with distance. D) VFMM graph is obtained by dividing the red curve to the black curve of the histogram in panel C.

4.3.2 Comparison between the Haversian canal probability density distribution (PDD) graphs of different samples

To compare different datasets of different samples, nine data stacks (three osteons in each of the three samples) were acquired, and the relative PDD graphs were computed with the same procedure presented in the previous section (Fig. 4.10). Similar to what is shown in Fig. 4.9.B, in all samples, an unmineralized matrix adjacent to the Haversian canal with widths varying from 3 to 10 µm is visible (see chapter 8 for the corresponding FIB-SEM images). The PDD graph of this region is constant over distance, which indicates

a homogeneous iodine staining of osteoid around the Haversian canal (except for sample FM40 osteon #3 that shows an increase in the average grey value of the unmineralized matrix from the surface of the Haversian canal up to ~2.5 µm). Afterward, a "transition zone" from unmineralized to mineralized is visible in all datasets. In the mineralized region, the two steps of increase in the degree of mineralization (red curves) are visible and are quite consistent in different datasets (except for sample FM48 osteons #1 and #3).

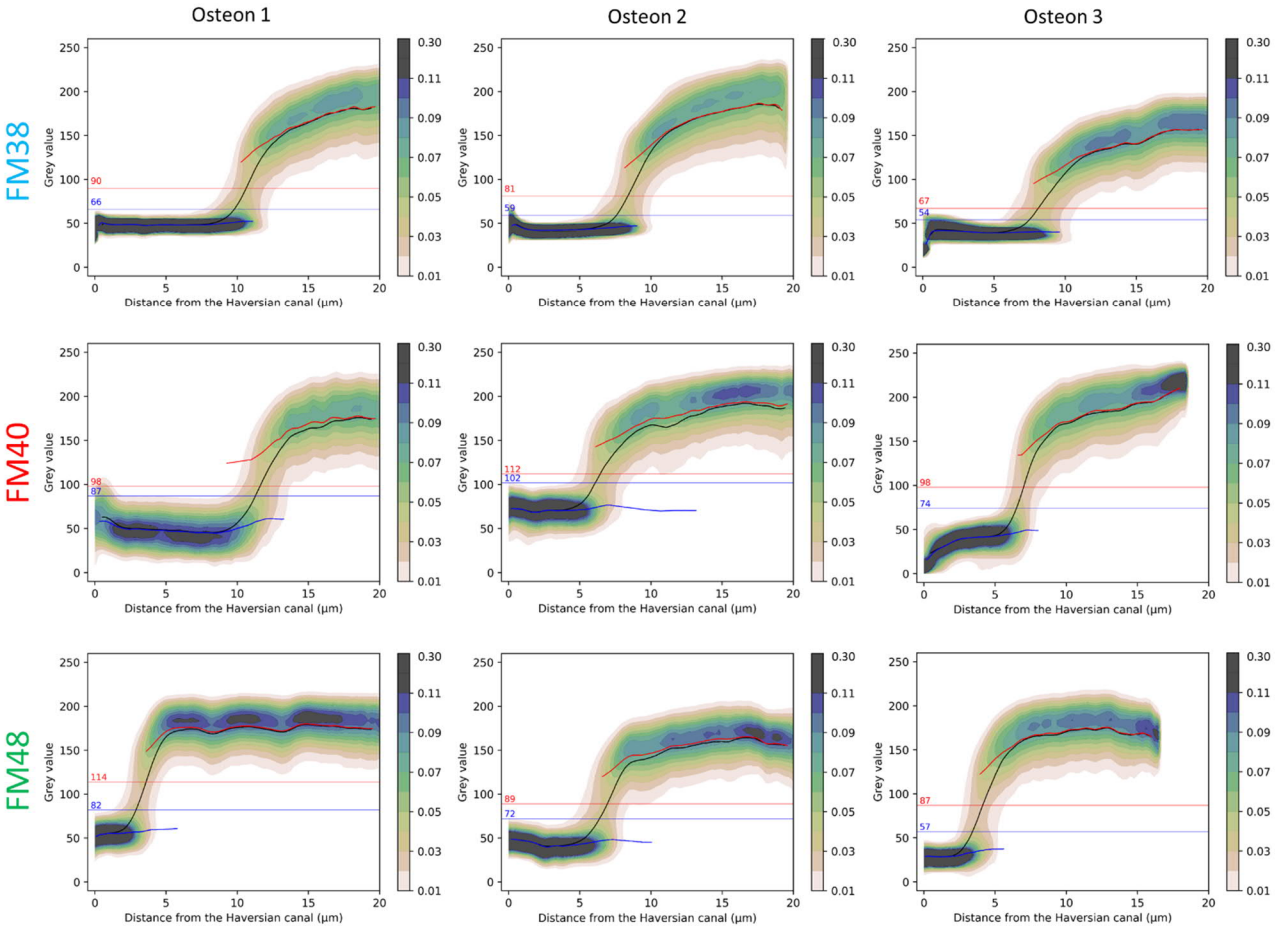

Fig. 4.10. PDD graphs of three samples (for each sample, three osteons were measured). The graphs show the similarities and differences in mineralization near the Haversian canal. For all samples, there is a fully unmineralized matrix adjacent to the Haversian canal with different sizes. The transition zone, in which mineralization of matrix starts, is visible in all samples. Moreover, two steps of mineralization with different slopes are visible further away.

4.3.3 Normalization of the PDD graphs

For comparing mineralization front properties in different osteons, the black fit curves of the PDD graphs in Fig. 4.10 were normalized and overlaid (Fig. 4.11). This normalization is also beneficial for a standard interpretation of data, as imaging parameters such as brightness and contrast are not precisely the same in all data acquisitions. For this, the histogram of grey values was used in Fig. 4.8.A and a linear equation was utilized to transform the data points of the black curve to values between 0 and 1. The grey value of the maximum frequency of PMMA and mineralized matrix were set at 0 and 1, respectively. The linear equation and related parameters are:

$$Y = \frac{X-p}{m-p}$$

where Y is the normalized grey value, X is the original grey value, p is the grey value of maximum frequency of PMMA, and m is the grey value of maximum frequency of mineralized matrix. For sample FM48 osteon #2, p and m are equal to 15 and 159, respectively (see the inset of Fig. 4.11). As it is seen in the equation, p is first subtracted from the original grey values to shift the curves down, and then the result is divided by the difference of m and p to compress the curve within 0 and 1. Afterward, the curves were shifted in the x direction to position the mineralization front (where the graphs start to increase) at zero. It is seen that the curves corresponding to the unmineralized matrix (before distance zero) have different values in different individuals. Specifically, FM40 osteons (red curves) are brighter than FM48's (green curves), most likely owing to the more intense staining with iodine. FM38 osteons (blue curves), which have the lowest normalized grey values, might have been less stained compared to the other individuals, a fact also distinguishable in FIB-SEM datasets (see chapter 8).

4.4 The lacuno-canalicular network (LCN) as a reference for mineralization of bone matrix

In all forming osteons, a mineralization front was observed that starts with a low VFMM region and ends with a high VFMM region, representative of younger and older tissues, respectively. This gradient is because mineralization happens in the same direction that osteoblasts deposit the unmineralized collagenous matrix [181]. Therefore, in addition to being 3D, these datasets provide a time-scale, which can be used in a spatio-temporal analysis of the forming bone. In this section, after visualization of regions with low to high VFMM (4.4.1), probability density distribution (PDD) graphs of each region will be presented (4.4.2). Afterward, the kinetics of mineralization with respect to the canaliculi will be assessed (4.4.3), and the degree of mineralization at the canalicular scale will be compared in different samples (4.4.4).

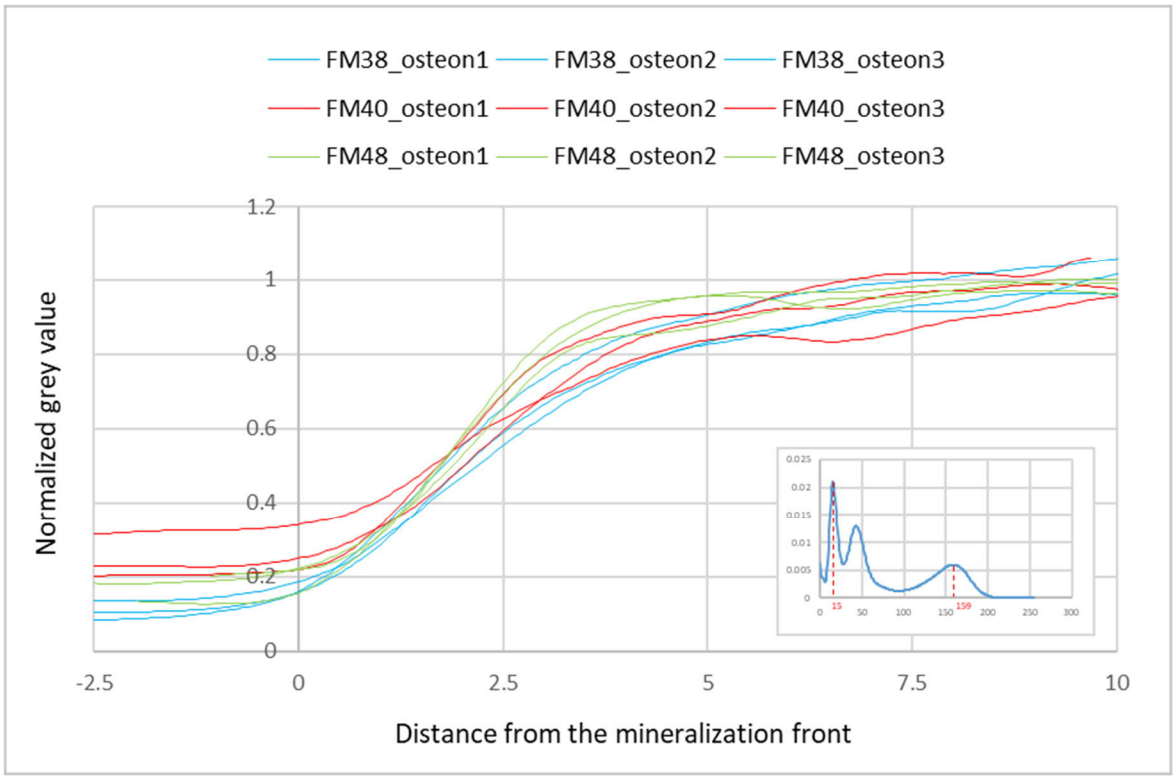

Fig. 4.11. Normalized PDD graphs of three samples; FM38 (blue curves), FM40 (red curves), and FM48 (green curves). Inset shows the histogram of grey values for sample FM48 osteon #2. m = 159 (grey value of maximum frequency of mineralized phase) and p = 15 (grey value of maximum frequency of PMMA phase) are used for calculating the parameters of the linear equation for normalization of black curves of PDD graphs.

4.4.1 Visualization of regions with the low, medium and high volume fraction of mineralized matrix (VFMM)

To understand the interaction of the LCN with its surrounding matrix at the mineralization front, the LCN was segmented and used as another reference for constructing distance maps. Fig. 4.12.A shows a magnified region of Fig. 4.7.B with a dense canaliculi network. It is visible that the canaliculi pervade the bone matrix from near the Haversian canal surface in the unmineralized matrix to an osteocyte lacuna in the mineralized matrix. To cover the transition zone from the unmineralized to the mineralized matrix, an ROI parallel to the mineralization front with the size of $8\times8\ \mu m^2$ was selected, and the region with VFMM between 5% and 95% was analyzed (Fig. 4.12.A, the yellow box). This subvolume was divided into three regions with low, medium, and high VFMM. The "low" region starts at 5% and ends in 35%, the "medium" region starts at 35% and ends in 65%, and the "high" region starts at 65% and ends in 95% of VFMM. Therefore, the

average VFMM for these regions was approximately 20%, 50%, and 80%, respectively. As the width of the mineralization front was ~4 µm, the subvolume containing the three regions (low, medium, high) was ~4×8×8 µm^3. Fig. 4.12.B-D show the cross-sections of these three regions that help to track the progress of mineralization around canaliculi. In the region with low VFMM, mineralization starts with the formation of isolated mineralization foci with a size range of ~50-600 nm. Interestingly, it is seen that they are mostly formed far away from the canaliculi, and a "halo zone" adjacent to the canaliculi surface remains. Later on, they grow, merge, and give rise to mineralization clusters that can be observed in the medium mineralized region. Finally, in the highly mineralized region, their density is so high that they form a homogeneous mineralized matrix. It is visible that the "halo zone" lingers in medium and highly mineralized regions, and the matrix in the vicinity of canaliculi is the last region that is mineralized.

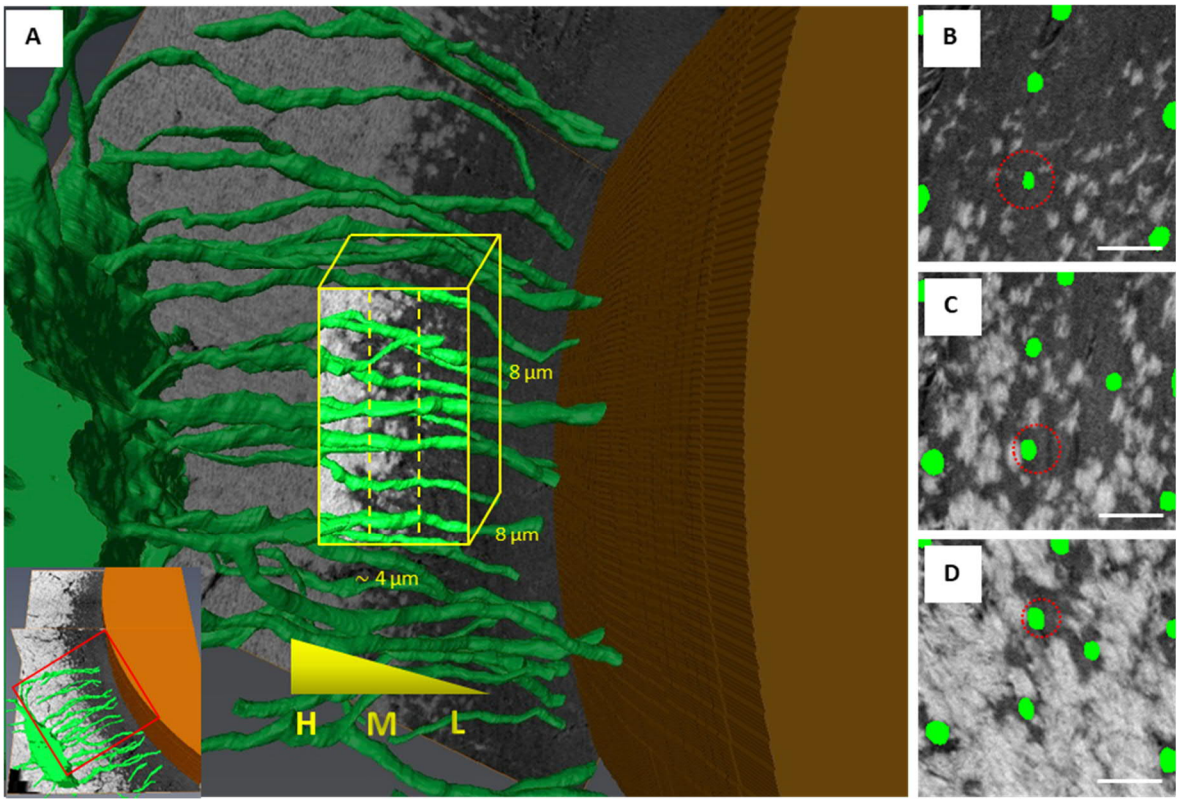

Fig. 4.12. A) High magnification image of the mineralization front with the pervading canaliculi network. From the Haversian canal (right) to the lacuna (left), an increase in VFMM is visible (Yellow triangle shows this increase; L, M, and H are representative of subvolumes with low, medium, and high VFMM, respectively). B) A region with low VFMM (20%), C) A region with medium VFMM (50%), and D) A region with high VFMM (80%). Dashed circles show "halo zones" around the canaliculi. Scale bars = 1 µm.

4.4.2 Probability density distribution (PDD) graphs of the regions with low, medium and high VFMM

To statistically confirm the presence of the "halo zone" at the mineralization front and to establish if its properties depend on the VFMM in the early stage of mineralization, PDD graphs were computed where the LCN was taken as the reference of distance. Fig. 4.13 shows the PDD graphs for the subvolumes shown in Fig. 4.12. The blue and red curves are constant over distance, which suggest a homogeneous iodine staining and a constant degree of mineralization, respectively. All the PDD graphs show that independent of the VFMM, there is a higher probability of finding unmineralized matrix around canaliculi, i.e., at small distances. As it can be inferred from the behavior of the black curve, the fraction of mineralized voxels increases with distance from the canaliculi. Furthermore, it can be observed that, although the width of the unmineralized matrix around canaliculi reduces as the mineralization proceeds, it still exists in later stages (Fig. 4.13.C). A similar conclusion can be drawn from VFMM histograms (Fig. 4.13.D-F). These histograms are obtained by dividing the number of mineralized voxels by the total number of voxels in a subvolume and show that, with increasing VFMM of subvolumes (from Fig. 4.13.D with ~20% to Fig. 4.13.F with ~80%), voxels at smaller distances around canaliculi are less mineralized.

4.4.3 Course of mineralization with respect to the LCN

To analyze the course of mineralization, exponential curves were fitted to the black curves in PDD graphs of the LCN. Here is the exponential equation:

$$Y = Y_0 - A \exp(-X/d)$$

where Y_0 is the plateau, A is the amplitude, and d is the decay length. With reference to the graphs shown in Fig. 4.13.A-C, the plateau is the average grey value at 2 μm distance, the amplitude is the range of grey values between distance zero and the plateau, and the decay length shows the distance at which the average grey value of the matrix reaches 63% of the amplitude. The decrease in decay length with increasing VFMM (Fig. 4.14) indicates that the mineralized matrix becomes closer to the surface of the canaliculi as the mineralization progresses (see chapter 8 for decay length of exponential fits for all datasets).

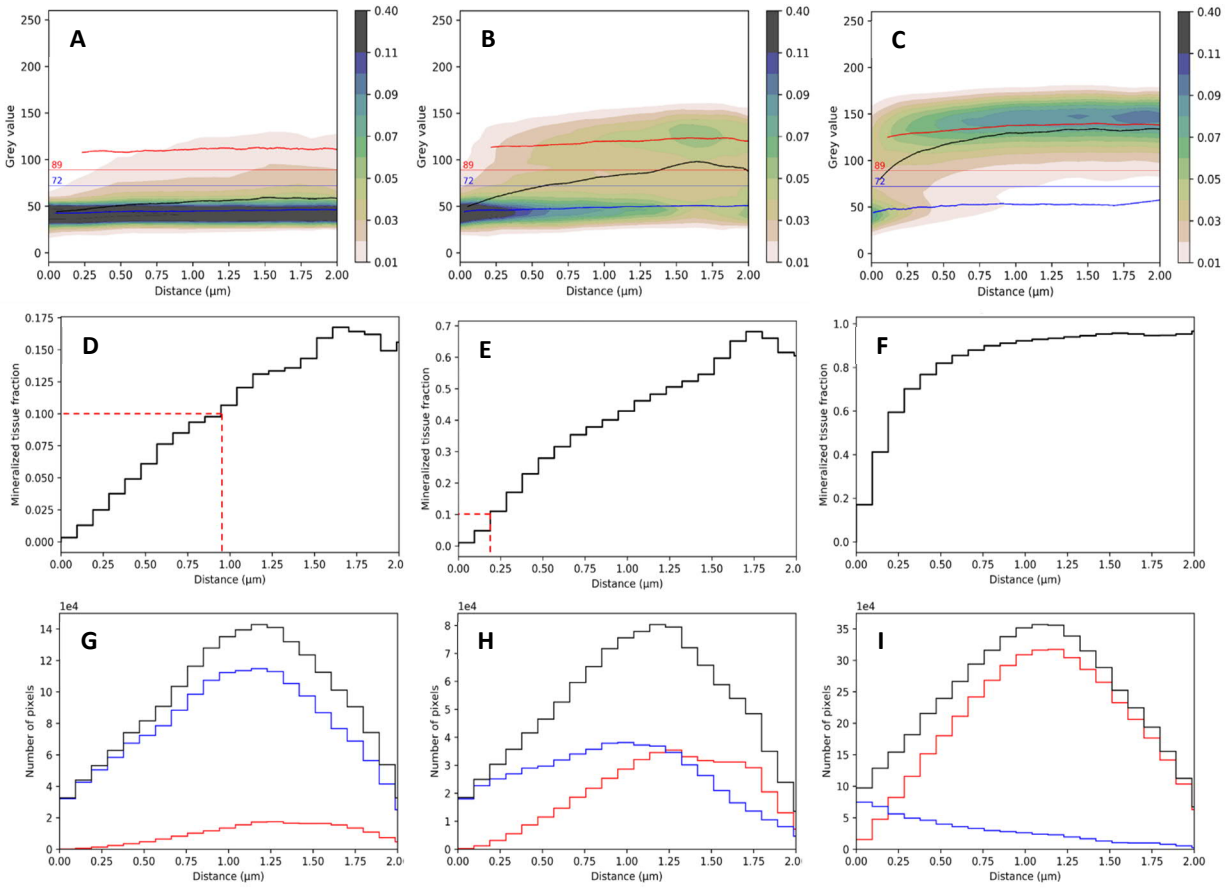

Fig. 4.13. PDD graphs (sample FM48 osteon #2, see chapter 8 for the other samples' data) of grey values at different distances from the canaliculi network for three regions with A) low, B) medium, and C) high VFMM. VFMM graphs of subvolumes with D) low, E) medium, and F) high VFMM. The dashed lines in Fig. 4.13.D and E show the distance where 10% of the matrix is mineralized. In panel F, this distance is almost zero. G, H, and I show the histogram of unmineralized (blue), mineralized (red), and all (black) voxels.

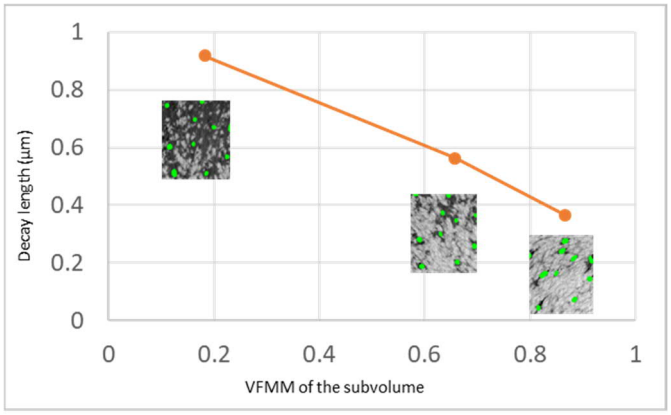

Fig. 4.14. Variation of decay lengths with VFMM. Note that only a single slice of the subvolume is shown. The presented data is from sample FM48 osteon #2 (see chapter 8 for the other samples' data).

4.4.4 Degree of mineralization with distance to the canaliculi

It was shown in Fig. 4.13 that the red fit curves corresponding to the mineralized matrix voxels (grey values higher than 89 for sample FM48, osteon #2) are parallel to the x axis (distance from canaliculi), which is an indication of a constant degree of mineralization with distance from canaliculi. To prove this effect statistically, the PDD graphs and red fit curves of subvolumes with low, medium, and high VFMM were plotted. Fig. 4.15 shows PDD graphs of high VFMM subvolumes for nine datasets of three samples (see chapter 8 for PDD graphs of low and medium VFMM subvolumes) in which the red curve is constant with distance, showing a constant degree of mineralization.

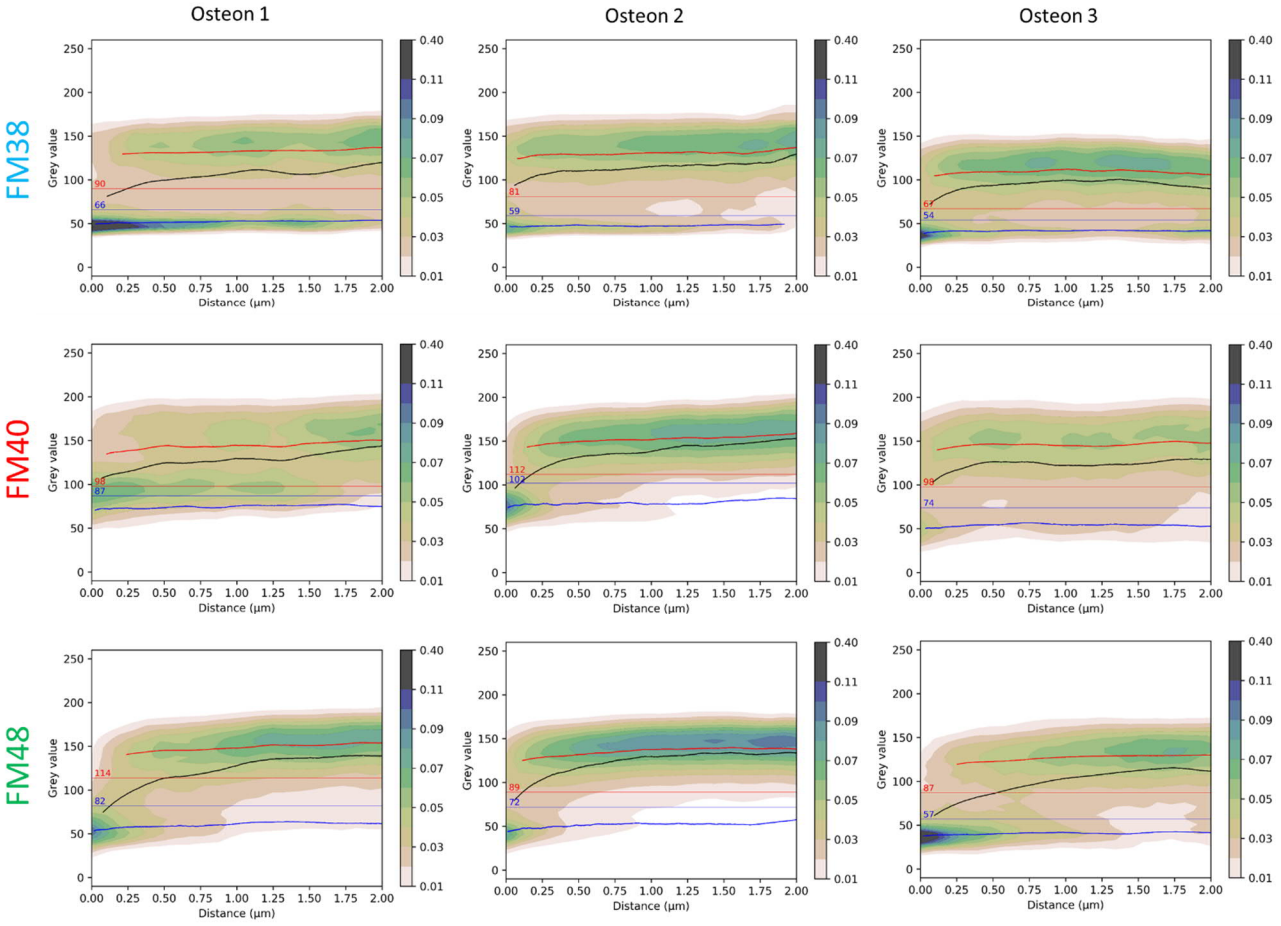

Fig. 4.15. PDD graphs of subvolumes with high VFMM for different samples. The degree of mineralization, which is depicted by the red fit curve, is constant over distance.

4.5 Local orientation of mineralization foci and unmineralized collagen fibrils

In regions with low VFMM, where mineralization foci were separated and not yet merged, the orientation of the foci was evaluated and compared with the orientation of the unmineralized fibrils (Fig. 4.16). The orientation was evaluated with the "Local orientation" module in Amira (Version 2019.38, Zuse Institute Berlin (ZIB), Berlin, Germany) that computes the orientation of objects in 3D, not only in the image plane. With this module, the image stack is first divided into bins (size of bins were 20 pixels in each dimension). Two main orientations for each bin were calculated, one for the unmineralized matrix (grey values between 0-72) and one for the mineralized matrix (grey values between 89-255). This was according to the thresholds calculated in section 4.2.3 (for sample FM48_osteon #2). After thresholding, a Fourier transform is calculated on each bin to extract the amplitude. For this, the inertia matrix M is computed on each Fourier transformed bin. The matrix is symmetric; therefore, the Jacobi iterative method can be used to extract the eigenvalues and the eigenvectors.

$$M = \begin{bmatrix} M_{xx} & M_{xy} & M_{xz} \\ M_{yx} & M_{yy} & M_{yz} \\ M_{zx} & M_{zy} & M_{zz} \end{bmatrix}$$

The eigenvector associated with the lowest eigenvalue is representative of the main fibril orientation. The confidence of the estimated main orientation is calculated with the following equation:

$$confidence = \frac{Val_1 + Val_2 - Val_3}{Val_1 + Val_2 + Val_3}$$

in which Val_1, Val_2, and Val_3 are the first (maximum), second, and third (minimum) eigenvalues, respectively. With this formula, the confidence is between 0.33 and 1, which was subsequently normalized to the range of 0 and 1.

Fig. 4.16 shows the two main orientations of bins associated with mineralization foci (orange) and unmineralized collagen fibrils (green). The orientation is depicted with the angles of foci and fibrils relative to the x (ϕ) and z (θ) axes. It is seen that mineralization foci are aligned with the unmineralized collagen fibrils. The histogram of orientations is also plotted in Fig. 4.16, showing the same angle for foci and fibrils.

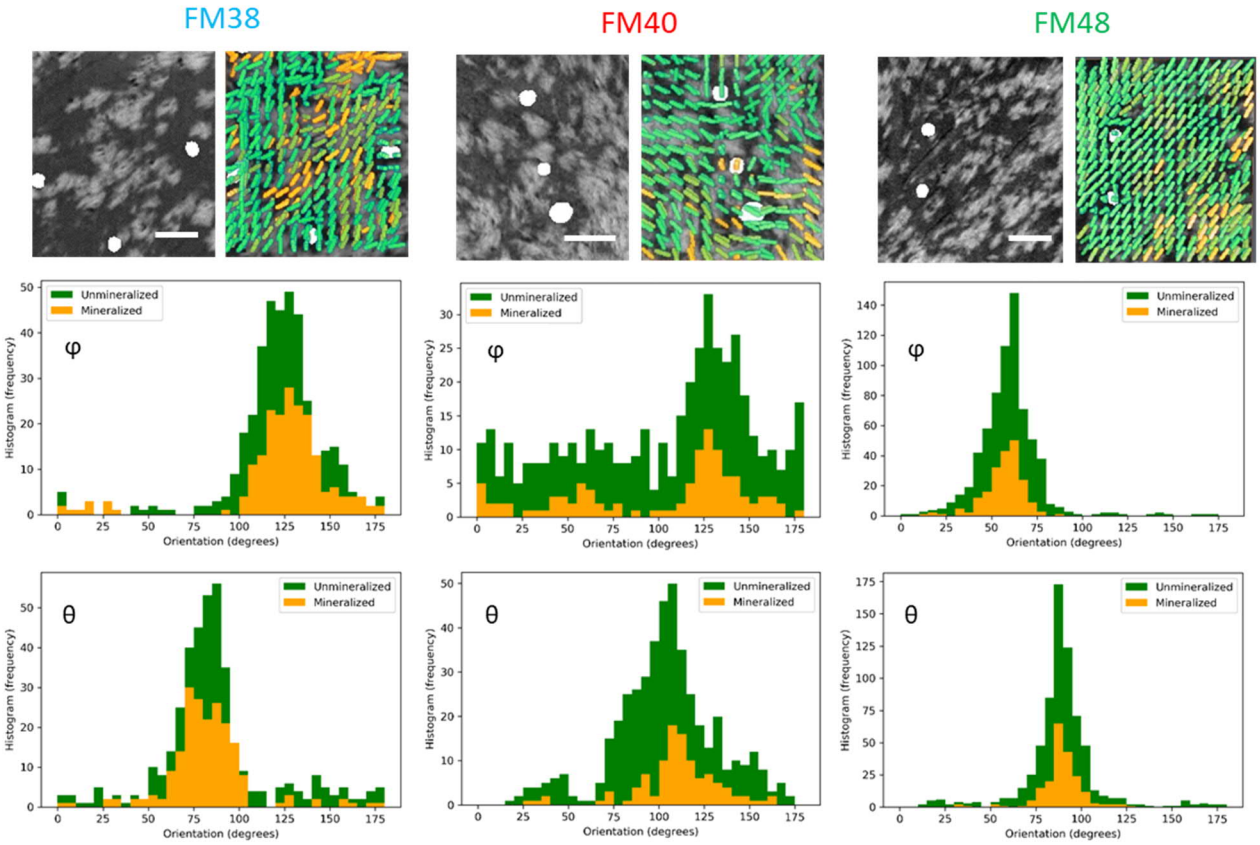

Fig. 4.16. Local orientation of mineralization foci (orange bars) and unmineralized collagen fibrils (green bars) for individuals FM38, FM40, and FM48 (each column is corresponding to an individual). The canaliculi cross-sections are white. The bins that contain both mineralized and unmineralized voxels are depicted with olive green. The histograms show the frequency of bins at each angle (green is for unmineralized and orange is for mineralized bins). ϕ and θ are the angles that the foci and fibrils are making with the x and z axes, respectively. Note that backscattered electron images are single slices of subvolumes extracted from FIB-SEM datasets. Scale bars = 1 μm

Chapter 5

Discussion

Bone consists mainly of the collagenous matrix, and minerals which are formed in the tightly controlled mineralization process [14]. By means of the "nucleation and growth" mechanism in bone, a mineralization front consisting of numerous mineralization foci is created. Through this process, the matrix becomes eventually homogeneously fully mineralized, with almost no unmineralized matrix remaining. Mineralization starts with the primary stage in which mineral content reaches 70% of its final value within a few days [17]. Prior to that, an unmineralized matrix is deposited by osteoblasts (5.1) where prenucleation droplets or matrix vesicles (MVs) are possibly implanted, which can promote the formation of mineralization foci (5.2). Alternatively, this stage of mineralization might be guided by the lacuno-canalicular network (LCN), through which mineral precursors are transported and deposited at the mineralization front (5.3). The foci, which are formed at this front, are elongated mineral clusters with specific orientation relative to the collagen fibrils (5.4). After the primary stage of mineralization, bone mineral content reaches its highest level in the secondary stage of mineralization within several years [85]. This process is believed to be aided by the osteocyte network, which would serve as the transport route for the mineral precursors [73] (5.5). In this work, the mineralization pattern on the micro/nanoscale was described with respect to the LCN and the Haversian canal, as this can reveal the mechanisms (5.6) behind the largely unknown and controversial mineralization process.

5.1 Unmineralized matrix formation

Although FIB-SEM does not provide live imaging of bone formation, the imaged regions provide a snapshot of the progression of the mineralization process. Therefore, the mineralization process was tracked from the beginning. In fact, in the imaged regions newly deposited matrix, the mineralization front and older fully mineralized matrix can be observed sequentially. The nine FIB-SEM datasets of forming osteons of three individuals (FM38, FM40, and FM48) and their probability density distribution (PDD) graphs confirmed that mineralization in bone remodeling always starts after secretion of an unmineralized matrix (Fig. 4.10). This observation is consistent with the studies that showed the formation of the osteoid by osteoblasts [18], which is followed by mineralization of the unmineralized collagenous matrix. Unmineralized matrix is reported to be visible in bone, dentin, and other calcified tissues except for enamel, in which minerals appear immediately adjacent to ameloblasts [182]. In bone, it is suggested that osteoblasts secret inhibitors, such as pyrophosphate, that can hinder mineralization close to the cells [53]. Therefore, an unmineralized matrix is always found adjacent to the Haversian canal in forming osteons. For mineralization, enzymes such as TNAP are suggested to cleave pyrophosphate, which in turn has two effects. First, a decrease in the concentration of pyrophosphate occurs. Second, the concentration of inorganic phosphate increases, which is needed for mineralization [53]. It is believed that the body fluid is supersaturated with respect to the hydroxyapatite [183]. Therefore, these inhibition and promotion

mechanisms are particularly important if the unmineralized matrix is also highly concentrated with calcium and phosphate ions.

The width of the osteoid seam in the measured osteons shows a distinct variation. Some osteons, such as FM38 osteon#1 and FM40 osteon #1, have wide (> 10 µm) osteoid seams while for some others, such as FM40 osteon #2 and FM48 osteon #1, it is narrow (< 5 µm) (see FIB-SEM datasets of all osteons in chapter 8). This observation was confirmed by the PDD graphs in Fig. 4.10. This variation can be explained by the location where each osteon is cut. Fig. 5.1 shows different stages of remodeling, which start with bone resorption by osteoclasts and are followed by secretion of collagen matrix by osteoblasts. The red window indicates the region from where the FIB-SEM datasets of this study are acquired, which consist of both unmineralized and mineralized matrices. At the left end of the window, mineralization has just started, and the mineralized tissue fraction in the cross-section is low while at the right end of the window, the tissue is almost mineralized and a small fraction in the cross-section is unmineralized. Depending on the position within this window, the unmineralized to mineralized matrix fraction can be different.

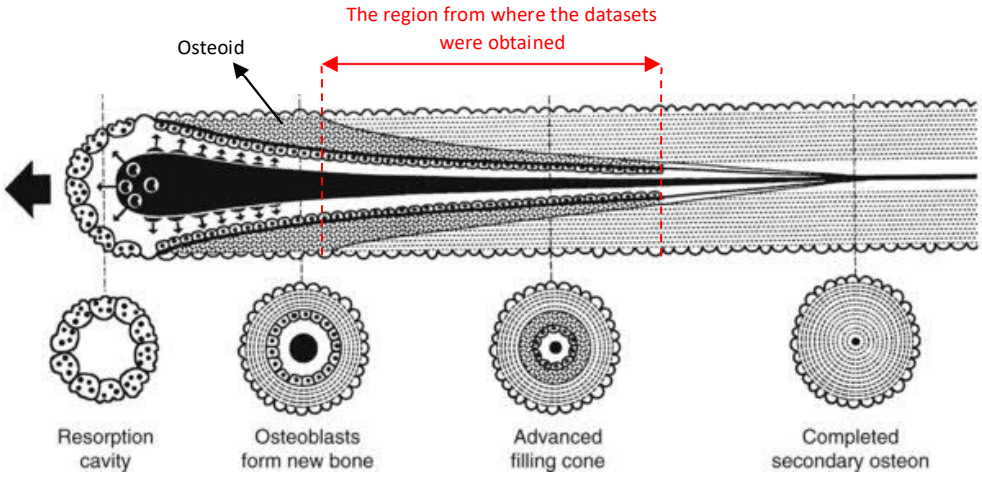

Fig. 5.1. Scheme of a forming osteon that shows every step of the remodeling from the bone resorption by osteoclasts to the bone formation by osteoblasts. Angiogenesis is happening in parallel to bone deposition in the black zone (a Haversian canal in the middle of the osteon). The red window indicates the region where the osteon starts to mineralize until it becomes fully mineralized. The FIB-SEM datasets were acquired from different zones of this region, resulting in samples having different unmineralized to mineralized matrix fractions. Note the change of the osteoid size within the window showing its largest and lowest size on the left and right ends of the window, respectively. Adapted with permission from [184].

5.2 Formation and growth of mineralization foci

After the secretion of the unmineralized matrix, mineralization appears in the form of foci at the interface of the unmineralized and mineralized matrices. Foci are small, electron-dense, and separated spots in the newly deposited matrix. They can form the fully mineralized matrix since they gradually grow and integrate with the neighboring foci. In this work, foci with different sizes were observed (~50-600 nm). The smaller foci appear darker than bigger ones in the SEM images, as demonstrated quantitatively in the PDD graphs in Fig. 4.10. The red fit curves in the graphs, which are related to the mineralized voxels, reveal that smaller foci have an average grey value of ~120 (e.g., for sample FM48 osteon #2). This value increases up to ~150 for bigger foci, and after that, the grey value increases in the fully mineralized matrix at the secondary stage of mineralization. The increase in the grey value of foci might be owing to three reasons. First, it is speculated that different size of mineral crystals is responsible for the distinctions in the grey values of foci, which means smaller foci contain smaller crystals, while bigger foci are composed of bigger crystals. Second, the different densities of mineral crystals in the foci might account for the variations in the grey values. If this is the case, the density of crystals in smaller foci is lower than in bigger foci. Third, considering the very small size of the foci in general, the partial volume effect can be responsible for the lower grey values of the smaller foci. A significant parameter in the partial volume effect is the resolution to the foci size ratio as it defines the number of voxels at the interface of the foci with the unmineralized matrix to the ones located in bulk. The higher the resolution to foci size ratio is, the higher the surface to bulk voxels ratio and, consequently, the higher the partial volume effect will be. The resolution of the FIB-SEM datasets was 40 nm, and the foci size ranges from ~50 to 600 nm, so the resolution to the foci size ratio varied from 0.8 to 0.06, respectively. Therefore, for smaller foci, the partial volume effect is considerable, while for bigger foci, where the resolution to foci size ratio is nearer to zero, the partial volume effect is negligible. It should be noted that this artifact was almost eliminated (see chapter 8, the yellow voxels in the colored backscattered electron images), thanks to the development of the two-threshold method for thresholding of unmineralized and mineralized matrix separately (Fig. 4.8). However, for future studies, foci can be analyzed individually with their grey value histograms to exclude the voxels with partial volume effect more precisely.

For all individuals, the average width of the zone where foci are observed, i.e., the width of the mineralization front (from 5% to 95% volume percentage of the mineralized matrix) is 3.67 ± 0.57 µm. This width was measurable from the FIB-SEM datasets (see chapter 8) by the PDD graphs (Fig. 4.11). The width of this region mainly depends on two parameters. First, the formation rate of foci, i.e. the number of deposited foci per volume and time, which is related to the agglomeration of mineral particles within collagen fibrils. Second, the growth rate of foci, which consists in the nucleation of more crystals in the

direct vicinity to the agglomerate or in the growth of the already precipitated crystals. The growth rate shows how fast a focus reaches its neighbors' surface and integrates with them (volume increase of mineralized area per time). If the formation rate was far faster than the growth rate, one could expect a wider mineralization front with foci of comparable size. On the other hand, the growth rate far faster than the formation rate might shorten the mineralization front and produce an almost flat interface between unmineralized and mineralized matrices. Fig. 5.2 shows the scheme of these two extreme scenarios.

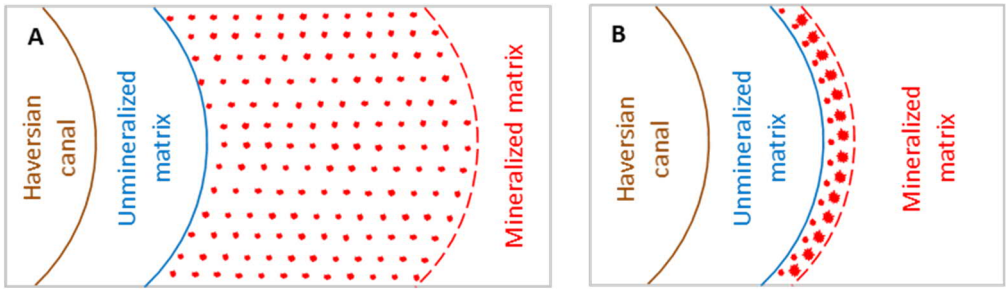

Fig. 5.2. Two extreme scenarios of mineralization with fast formation rate/slow growth rate of the foci (A) and slow formation/fast foci growth rate (B). In scenario A, the foci are formed so fast that they do not have enough time to grow, so a wide mineralization front is created. On the other hand, in scenario B, the foci are immediately grown and join the mineralized matrix (see the bigger foci at the interface). Therefore, the mineralization front is narrow. Note that the dashed red lines suggest that there is no sharp interface between the mineralization foci and the fully mineralized matrix.

By comparing these two extreme scenarios with the mineralization fronts in the datasets of this work, two conclusions can be drawn. First, as the fronts are neither so wide that the entire unmineralized matrix is filled with the foci nor so narrow that a flat interface between unmineralized and mineralized matrices is created, it is argued that the formation and growth of the foci happen in a similar timescale causing a defined transition zone. Second, as it was observed in Fig. 4.11 and FIB-SEM datasets, the mineralization fronts are similar in all individuals in terms of size and distribution of the foci (3.67 ± 0.57 µm) that shows the formation and growth in healthy bones are happening similarly, which might indicate that all individuals are mineralized with the same mechanisms independent of factors such as the density of the LCN, size of the osteon, or the age of the individuals.

Mineral apposition rate (MAR) has been quantified with histomorphometric analyses in which a fluorochrome such as tetracycline is used to mark the mineralization front in the early stages of mineral formation. This refers to the investigated regions in the present study, where the location, number, and growth of the foci likely define where the fluorescent label forms. Bone histomorphometry allows the

precise calculation of MAR since the fluorochrome is injected at multiple times at a known time interval [181]. It has been observed that MAR decreased with a quadratic function of time for trabecular bone. For osteonal bone, it has been reported that bone apposition rate decreased with an exponential function of radius [185]. Similarly, in osteonal sheep bone, it was observed that MAR increase was proportional to the unfilled wall width of the osteon (inversely proportional to time). Metz *et al.* [186] postulated that osteocytes give the signal to the osteoblasts to reduce bone apposition rate. In general, the investigation of the mineralization front should be considered in future works as it has been reported that variations in the mineralization front can be a diagnostic criterion [187, 188].

5.3 Role of the lacuno-canalicular network (LCN) on the early stage of mineralization

Thanks to the high density of the LCN (74 km/cm^3) in human osteons [9] and the LCN's high surface to volume ratio, the LCN might have different interactions with the matrix that results in different phenomena in bone mineralization. Two phenomena were identified and analyzed in the measurements of this work. First, it was observed that mineralization foci are deposited further away from the canaliculi surface and create a "halo zone" free of minerals (Fig. 4.12) similar to what is seen around the Haversian canal where unmineralized matrix had higher probability density adjacent to the surface. In the case of the Haversian canal, the volume fraction of mineralized matrix (VFMM) was approximately zero, while in the case of canaliculi, some amounts of minerals were found right beside the canaliculi surface. Second, it was revealed that the mineralization degree of the foci is almost constant with the distance to the canaliculi (e.g., 136.06 ± 3.03 for PDD graph in Fig. 4.15, FM38 osteon #1) in different subvolumes with low, medium and high VFMM (Fig. 4.15) or it has a slight upward slope (e.g., 147.86 ± 5.64 for PDD graph in Fig. 4.15, FM40 osteon #1). In both cases, this observation is in contrast with the hypothesis that simple diffusion of mineral precursors from the canaliculi can be responsible for the increase in the mineralization degree in the bone matrix [23].

For the halo zone effect, the probability density distribution was quantified for the mineralized and unmineralized matrices with distance. For instance, for the PDD and VFMM graphs in Fig. 4.13.A and 4.13.D which are related to a subvolume with medium VFMM, the fraction of unmineralized matrix at distance 0.2 μm is 0.9, and is 0.1 for the mineralized matrix. However, far away from the canaliculi surface, e.g. at distance 2 μm, the fraction of the unmineralized matrix is 0.4, and for the mineralized matrix is 0.6. This distinction indicates that the fraction of the unmineralized voxels to the total voxels is high near the surface of the canaliculi, which gradually decreases with distance. The same trend is visible in the

subvolumes with low and high VFMM, indicating that the halo zone exists until the matrix is fully mineralized. Moreover, it is observed that this halo zone only exists at the mineralization front and shrinks as mineralization proceeds. This effect was quantified in Fig. 4.13.D-F. In the subvolume with low VFMM, the distance at which 10% of the matrix is mineralized is ~0.9 µm, while for medium and high VFMM, this distance is ~0.2 µm and ~0.0 µm respectively.

By looking at the PDD graphs of the canaliculi, it is realized that mineralization follows the black curve in Fig. 5.3.A, indicating the presence of the halo zone near the canaliculi surface. One speculation for this observation is the diffusion of the inhibitors from the canaliculi surface into the matrix. The red curve in Fig. 5.3.A, which is originally the black curve vertically flipped, indicates the diffusion profile of inhibitors. This model shows there is a gradient of inhibitor concentration in the unmineralized matrix. When mineralization is initiated, the regions where the concentration of inhibitors are lower, i.e. the regions far away from the canaliculi surface, show a higher density of mineralization foci. On the other hand, the regions with a higher concentration of inhibitors, i.e. the regions near the surface of the canaliculi, exhibit a lower density of mineralization foci.

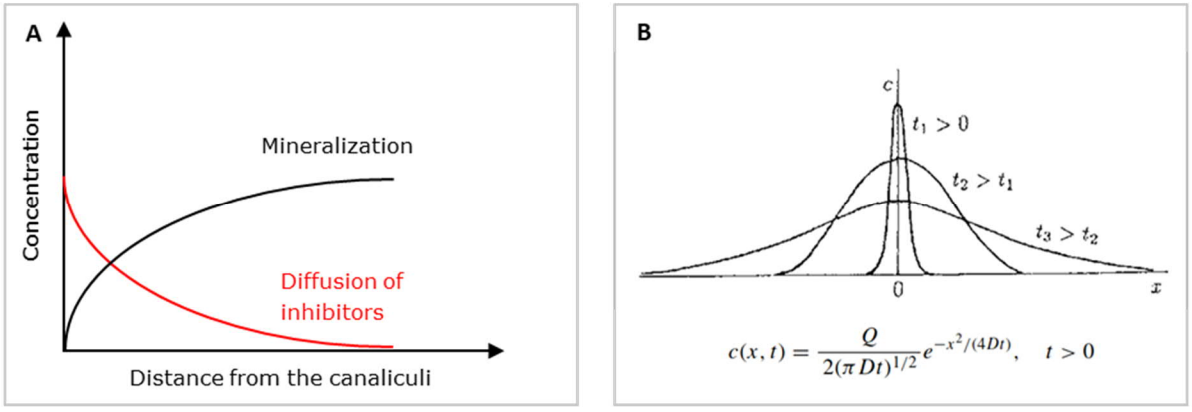

Fig. 5.3. A) Qualitative scheme of the black curves in the PDD graphs and diffusion profile for inhibitors. B) Diffusion profiles in which Q particles with diffusion coefficient of D are released at x (distance) = 0 and t (time) = 0 [189]. It is seen that the diffusing component is highly concentrated at the reference surface near time zero ($t_1 > 0$). When diffusion proceeds, the concentration at the reference surface decreases substantially and increases further away gradually ($t_2 > t_1$). At longer times, the concentration will be more homogeneously distributed, and the diffusing component reaches far distances ($t_3 > t_2$). The equation below the curves shows the concentration in terms of time and distance from the reference point. Adapted with permission from [189].

Another speculation for the existence of the halo zone around the canaliculi, is the formation of the Liesegang rings in which periodic precipitation occurs, while diffusion and reaction of ions happen simultaneously [190]. The rings were observed for the first time by Raphael E. Liesegang, who could produce silver chromate rings *in vitro* by adding concentrated silver nitrate solution to a potassium dichromate containing gel [191]. He observed that concentric rings of silver dichromate precipitated at the diffusion front, and distance between them increased with time (Fig. 5.4.A). One of the mostly accepted models to describe the Liesegang rings formation was proposed by Ostwald in 1897 who suggested that supersaturation of ions and a fast chemical reaction afterward lead to a depleted zone behind the diffusion front, as the diffusion rate is too low to feed the nuclei [192, 193]. Several parameters can affect the formation of Liesegang rings, such as gel concentration, ion concentration, and temperature. The concentration of the inner ion should be within a narrow range to promote Liesegang ring formation since a high concentration of it, hinders diffusion of the outer ion. On the other hand, a high concentration of the outer ion results in the formation of more rings [193]. In general, any variation in parameters that causes faster diffusion (like higher temperature and a lower concentration of gel) will lead to fewer rings and shorter distances between them.

The Liesegang rings phenomenon was also observed in the *in vivo* systems as many cations and polyanions are involved (see the examples in Fig. 5.4.C-F). Polymers of high molecular weight in the body, such as proteins, nucleic acids, polysaccharides, and lipids can form an extracellular milieu similar to the gel environment used in the *in vitro* systems. In the *in vivo* systems, supersaturated solutions of the mineral cations (such as calcium), inorganic anions (phosphate, silicate, and carbonate), organic polycations (polyamines and histones) and organic polyanions (acidic proteins and nucleic acids) are responsible for Liesegang ring formation [194]. It is speculated that this phenomenon can appear in bone where ions with different diffusion coefficients are moving in a gel-like medium (i.e., the osteoid) and precipitating.

For the second phenomenon (constant degree of mineralization with distance from the LCN), foci size distribution with respect to the canaliculi might explain the effect. It was observed that foci size (Fig. 4.9.A), as well as their degree of mineralization, increases with distance from the Haversian canal (see the red fit curve in Fig. 4.9.B until 8 μm). The preliminary results of the size distribution also confirm that the foci are smaller close to the Haversian canal (average size = ~50 nm), and their size gradually increases until they form bigger aggregates (average size = ~200 nm) (Fig. 5.5).

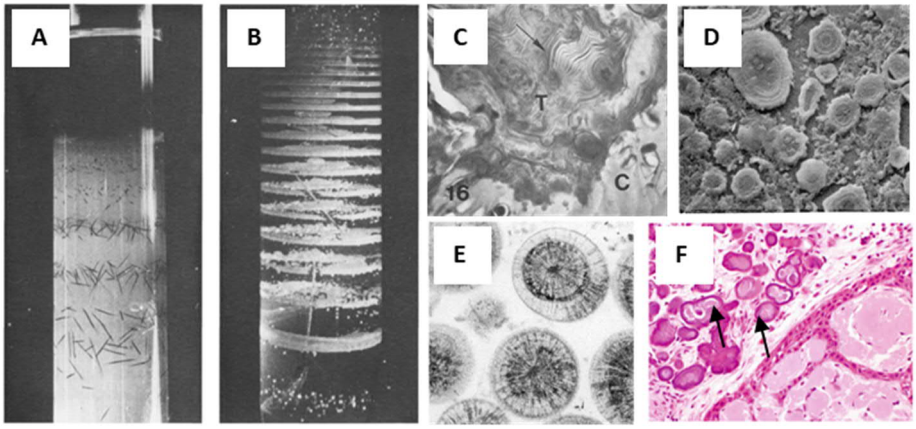

Fig. 5.4. Examples of Liesegang rings in different *in vitro* and *in vivo* environments. A) Needle-like Silver chromate precipitates in the form of Liesegang rings from top to down [195]. B) Calcium phosphate precipitates [195]. C) Mineralized tessera (T) abutting unmineralized hyaline cartilage (C) [196]. D) Liesegang rings in the renal cyst [194]. E) Calcium carbonate in oolithic limestone [194]. F) Calcifying Epithelial Odontogenic Tumor [197]. The arrows show the concentric laminations, which are the results of Liesegang rings calcification. All images are adapted with permission from the corresponding references.

Therefore, there might be a correlation between the size of the foci and their degree of mineralization, i.e. the smaller the foci are, the lower their degree of mineralization is. It can be speculated that the foci near the canaliculi and far away from them, at a given distance from the Haversian canal, have a similar degree of mineralization because they have more or less the same size. In fact, the average foci size is increasing with distance from the Haversian canal, but it is constant with distance from the canaliculi (Fig. 5.5). The halo zone and the size distribution of the foci around the Haversian canal and the canaliculi are depicted in the scheme in Fig. 5.6.

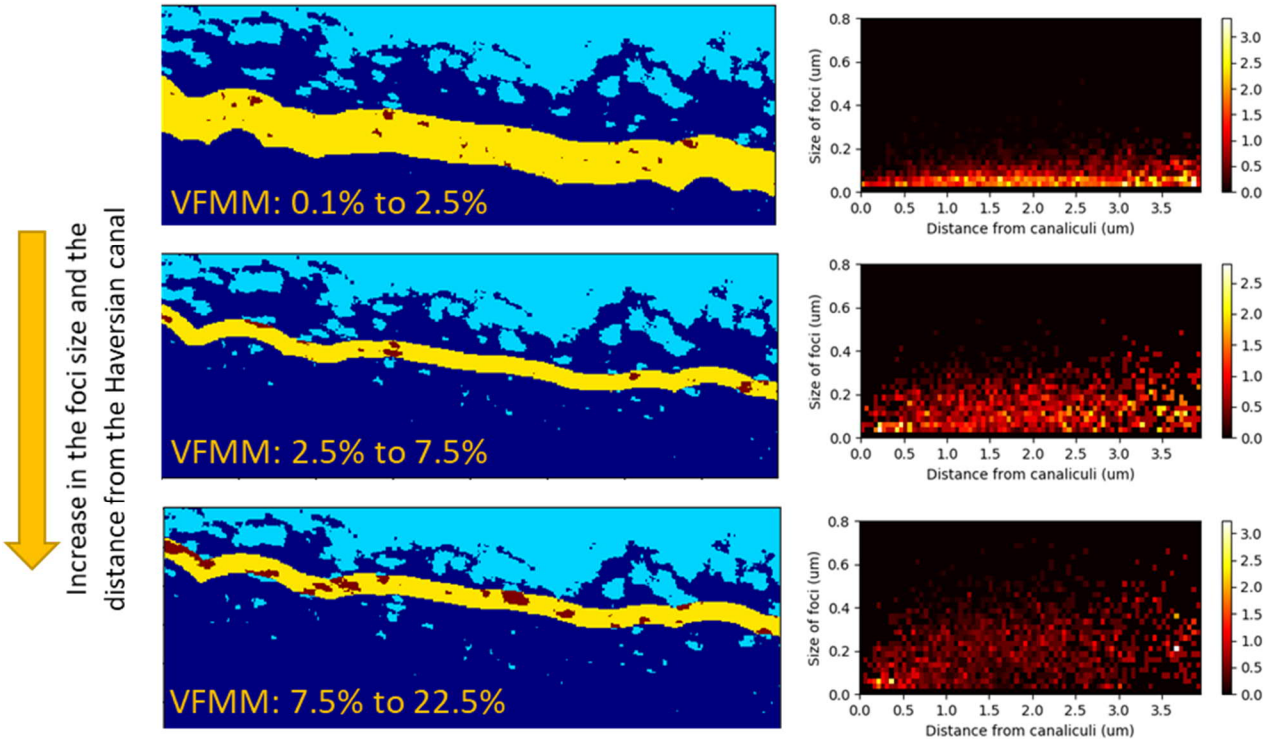

Fig. 5.5. The size distribution of the foci with respect to the Haversian canal and the LCN. The yellow bands in the left images are selected based on the VFMM and highlight the foci used for the size-distance correlation in the right graphs. The first row corresponds to the foci nearer to the Haversian canal, and the last row is related to the foci further away from the Haversian canal.

As the halo zone only exists at the mineralization front, its contribution is only for the primary stage of mineralization where huge amounts of mineral precursors (70% of the final calcium content of the mineralized matrix [17]) are deposited. For the secondary stage of mineralization, the collagen matrix is highly mineralized, and the mineral precursors can be transported through the dense matrix or through the lacuno-canalicular network. Hence, this stage is too slow and usually takes several years [85].

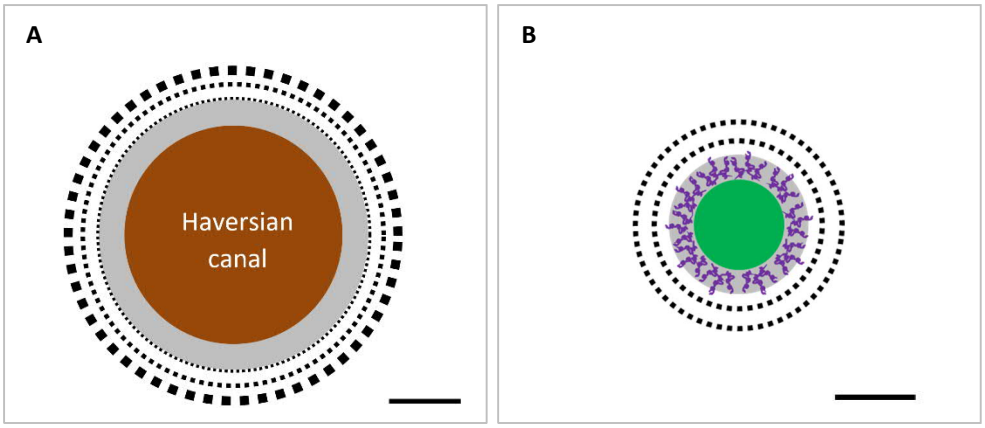

Fig. 5.6. Scheme of mineralization around A) the Haversian canal and B) the canaliculus (green filled circle). Grey zones adjacent to the canals are unmineralized matrix. Dashed circles around the canals show mineralization foci that have different sizes around the Haversian canal but similar sizes around the LCN. The purple coiled structures are representative of diffusing inhibitors in the vicinity of the canaliculi that can inhibit foci formation. Scale bars for A = 10 µm and B = 0.5 µm.

5.4 Foci orientation

Minerals appear in the matrix in the form of separated mineralization foci, as discussed earlier. Thanks to the high-resolution FIB-SEM images, foci were identified in the matrix in terms of their 3D shape and orientation. In contrast to studies that observed spheres or rounded mineral aggregates [18, 198], the backscattered electron images and local orientation analysis in this work revealed that foci are elongated parallel to the long axis of collagen fibrils (Fig. 4.16). If the nucleation of crystals happens within MVs, the shape of the vesicles might determine the final shape of the foci. The original shape of MVs is spherical, as observed with electron microscopy [14]. However, it is speculated that their shape can adapt to the space confined by collagen fibrils after they are budded from the osteoblasts. Therefore, the MVs might change from spheres to ellipsoids, and consequently, mineralization foci will be elongated. Interestingly, a similar phenomenon was observed in the unmineralized matrix, where the cross-sections of the canaliculi were elliptical, and their major axis was parallel to the adjacent collagen fibrils. It shows that collagen fibrils are stiff enough to shape soft tissues such as the canaliculus wall and probably MV membranes according to their orientation (Fig. 5.7).

Alternatively, the crystals might be formed in intra- or interfibrillar regions and follow the orientation of collagen fibrils independent of vesicles [199]. This process can happen through NCP-aided mineralization.

One role of the NCPs such as osteopontin in bone mineralization is to stimulate the formation of polymer-induced liquid precursor droplets that can enter intrafibrillar regions of collagen and initiate mineralization while they inhibit extrafibrillar mineralization [95]. In this case, the addition of more droplets will lead to the extension of prenucleation clusters along the collagen fibrils. At some point after crystal nucleation, these clusters can extend to the extrafibrillar spaces while keeping their elongated shape.

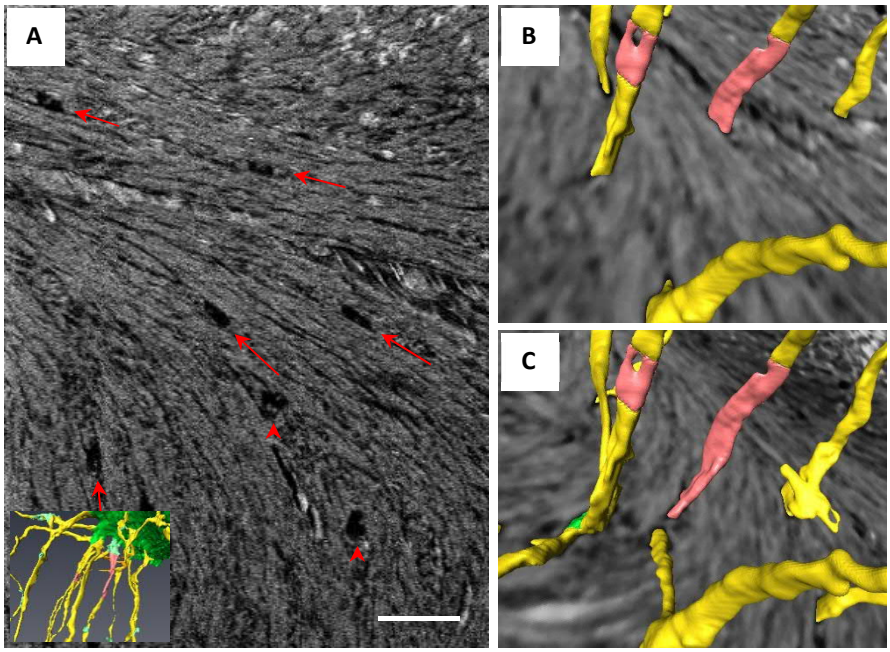

Fig. 5.7. A) The cross-sections of the canaliculi within the unmineralized matrix. The arrows are showing the direction of the elliptical canaliculi, which are aligned with the collagen fibrils orientation. Some of the canaliculi are circular (the arrowheads). The collagen fibrils around them are not well organized, which might allow them to keep their circular shape. The inset shows the 3D rendering of the canaliculi in this region. B) and C) Magnified images of the canaliculi in 3D. The pink canaliculus highlights the elliptical shape of the canaliculus cross-section. It should be noted that in contrast to this observation, other reports show that the collagen matrix around the canaliculi is mainly disordered [200]. Scale bar = 2 μm.

5.5 Mineralized globules and the secondary stage of mineralization

After formation, the mineralization foci grow until they form an integrated, fully mineralized matrix. The microstructure of this matrix is globular (Fig. 4.9.A), confirming that the mineralized matrix is formed by the integration of numerous recently grown foci. The boundary of the globules has lower grey values in the backscattered electron images in comparison to the inner voxels of each globule, owing to the lower degree of mineralization of these boundaries. This effect might be the result of NCPs accumulation, which were

deposited by osteoblasts in the matrix for various functions such as regulation of mineralization, matrix organization, or cell-matrix interactions [14]. This globular microstructure is similar to what was previously observed by Barragan *et al.*, who studied the microstructure of mineralizing bone *in vitro* [18]. Seemingly, the globular microstructure is tessellated, which can contribute to enhancing the toughness of bone along with the contribution of its lamellar- and nanostructure to the mechanical properties.

The increase in the degree of mineralization of globules happens in the secondary stage of mineralization in which the LCN might play an essential role in transporting mineral precursors through the mineralized matrix [73]. By looking at PDD graphs with respect to the distance from the Haversian canal (Fig. 4.10), a gentle slope was also observed in seven out of nine datasets (for instance Fig. 4.9.B, between ~8 – 17 µm) that can be attributed to the secondary stage of mineralization. In the other two datasets, mineralization degree is constant with distance, which might be due to the less dense LCN in these two datasets that causes lower transport rates of mineral precursors, and consequently results in the constant mineralization degree with distance to the Haversian canal.

5.6 Possible models for the early stage of mineralization in forming osteons

Two models can be introduced based on this study that might explain the early stage of mineralization in bone remodeling. In the first one, the LCN plays an active role in transporting the mineral precursors. This mechanism is particularly important if the matrix is not sufficiently saturated with the mineral precursors and if diffusion of ions cannot happen from the Haversian canal toward the mineralization front. For diffusion, a gradient in the calcium and phosphate concentration is needed. However, Christoffersen *et al.* calculated the calcium concentration near the mineralization front and the osteoblasts, and found out that no ion gradient exists [182]. They used Fick's first law of diffusion and derived the following equation:

$$C_{\text{surf}} = C_b - \frac{x v_{\perp} \rho_m 10}{M_{HAP} D} = 2.5mM - 2.1 \times 10^{-3} mM \cong C_b$$

where C_{surf} is calcium concentration at the mineralization front, C_b is calcium concentration near the osteoblasts, x = 10 µm is the thickness of the osteoid seam, $v_{\perp} = 10^{-6}$ m/day is the velocity of mineralization front, $\rho_m \cong 1.8$ g/cm^3 is the density of mineral in bone, $M_{HAP} = 10^3$ g/mole is the molar mass of Hydroxyapatite, and $D \cong 10^{-5}$ cm^2/s is the diffusion coefficient of ions in the matrix.

Their calculation shows that $C_{\text{surf}} \cong C_b$ which means that calcium concentration at both the proximal and distal sides of the unmineralized matrix is almost equal. Therefore, they proposed that no bulk diffusion (from the osteoblast to the mineralization front) is happening, and diffusion might only occur locally for

short-range transports in the vicinity of the crystals [182]. In another study, mineralizing osteons were studied with a mathematical model. Martin *et al.* also found that because of the low diffusion coefficient of calcium ions in the unmineralized matrix, simple diffusion cannot be responsible for the transport of ions through the mineralizing matrix. They suggested that cells are responsible for mineral transport [86]. It was observed in the FIB-SEM datasets of this study that a dense network of canaliculi exists at the mineralization front connecting the Haversian canal to the mineralized matrix. It is known that the canalicular space is filled with fluid that contains mineral precursors [74]. Therefore, canaliculi can be considered as fast routes of ion transport to the sites of mineralization [201-203]. The lack of minerals near the canaliculi in this model can be owing to the formation of Liesegang rings or the diffusion of inhibitors near the surface of the canaliculi, as explained earlier.

In an alternative model, the matrix should be highly concentrated with calcium and phosphate ions during osteoid deposition, most probably as calcium polyphosphate complexes [14, 20], which can be secreted by osteoblasts. In this model, the calcium ions can either pass through the cells or percolate between cells to reach the tissue [14]. The promotion of mineralization in this scenario is explained by the existence of MVs or action of some types of NCPs known as promoters. The MVs, which are budded from the osteoblasts, can accumulate calcium and phosphate ions from the matrix and form the foci of mineralization [20]. It is suggested that the influx of ions occurs through annexins and Na^+/Pi co-transporters, which are located on the MVs. The nanocrystals formed in the lumen of MVs will grow until they rupture the MVs membrane and enter the intra- or interfibrillar space. The vesicles contain alkaline phosphatase to remove the inhibitory effect of pyrophosphate [88]. In the case of NCPs, they can have a "dual function" of inhibition and promotion of mineralization and can act as nucleation centers when it is needed. Dentin Matrix Protein 1 (DMP1) is known as an NCP that exhibit this dual effect. DMP1 has two separate sites for binding to calcium-phosphate clusters and collagen. It can temporarily stabilize calcium and phosphate, guide the complex to the collagen matrix, and subsequently initiate mineralization [117]. Some NCPs, such as bone sialoprotein [198] and osteopontin [204], are observed to be co-localized with the mineralization foci that strengthen the hypothesis that states NCPs act as promoters of mineralization.

This model is also consistent with a FIB-SEM dataset acquired in the present study, which shows a region as large as $25\times35\times40$ μm^3 with a few canaliculi (see chapter 8, Fig. 8.11), with a mineralization front similar to what is found in other datasets. Similarly, in anosteocytic fish bone such as swordfish, it is seen that bones are normally mineralized similar to human osteonal bone, although no osteocyte network exists [205] (Fig. 5.8). Backscattered electron images of the forming, anosteocytic osteons showed that osteoid is formed around the Haversian canal, through which transport of mineral precursors likely happens. In another study of anosteocytic bone, Ofer *et al.* showed that osteogenesis happens in anosteocytic bones by

osteoblasts, which are trapped in the osteoid. The osteoblasts will undergo apoptosis and get mineralized during mineralization of the matrix and no osteocyte network forms [206].

Although this model can explain the early stage of mineralization independent of the LCN, it has several limitations. First, the concentration of ions in the unmineralized matrix would need to be 1000-fold above the saturation limit. This large amount of mineral precursors in the unmineralized matrix can only be stable with a substantial amount of inhibitors. However, the backscattered electron images of the FIB-SEM datasets of the current study and cryo-microscopy investigations of other works, e.g. a chicken embryo bone study [207], do not show high concentration of mineral precursors or inhibitors in the unmineralized matrix. Second, if the matrix would be highly concentrated with the ions, it is expected that mineralization starts immediately after secretion of the osteoid, but, no preferential nucleation was observed close to the osteoblasts (adjacent to the Haversian canal). Third, it was shown that around the canaliculi, there is a halo zone free of mineral, most probably due to the presence of inhibitors. However, in this model, the matrix already has a large amount of inhibitors everywhere to bind the ions, and therefore the presence of the halo zone is hard to explain. Fourth, preosteocyte cells would be directly exposed to a highly concentrated fluid in this model. If there would be an ion concentration in the molar range in the non-mineralized tissue, it would immediately cause cell death.

While there are ways to explain the issues mentioned above, many aspects remain unaddressed, for which further studies are needed (see chapter 7). For the first issue, one can imagine that due to the sample preparation procedure, which includes freezing, dehydrating, and embedding of the bone tissue, the mineral precursors, ions, and inhibitors were eliminated. If this is the case, the only way to be sure that the classical sample preparation does not introduce any artifact would be using cryo approaches. However, high-pressure freezing of human bone is not something that can be easily achieved. Regarding the second issue, the slow kinetics of mineralization via MVs might be an acceptable explanation: While the minerals are being formed via the vesicles (this process includes cleavage of inhibitors, the influx of the ions inside the vesicles, the formation of ACP, and crystallization in the extracellular matrix [88]), the osteoblasts have already deposited the new collagenous matrix, and therefore, they are far away from the mineralization front. For the third issue, one can speculate that if MVs are the triggers of the mineralization, a lack of MVs near the canaliculi can account for the absence of minerals in the halo zone. It is difficult to imagine, though, why MVs should be preferentially excluded from the canalicular surroundings. Finally, regarding the toxicity effect of high concentrations of calcium ions on the cells, it is suggested that sequestration of calcium ions by binding proteins [14] might reduce the toxicity since the concentration of cytosolic free calcium is kept very low (less than 1 μM [14]). Due to these open questions, the very early mineralization processes is still a highly debated topic.

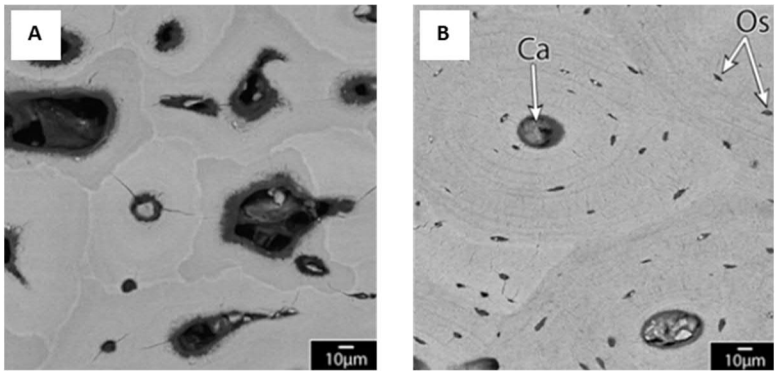

Fig. 5.8. Backscattered electron images of anosteocytic osteonal tissue of swordfish (A) in comparison to the Horse osteons with osteocyte network (B). Ca and Os indicate the Haversian canal and the osteocyte lacunae, respectively. The anosteocytic tissue shows some forming osteons with an unmineralized matrix around the Haversian canal, similar to what has been observed in this work for human osteonal bone. The existence of such forming osteons strengthens the hypothesis of primary mineralization by MVs or NCPs without the help of the osteocyte network. Adapted with permission from [205].

Chapter 6

Conclusion

This study aimed at understanding the mechanisms laying behind the early stage of mineralization in the forming osteonal tissue where osteocytes create a dense network. To achieve this aim, different 2D and 3D characterization and imaging techniques, such as FIB-SEM, CLSM, ESEM, and EDX, were used to measure the lacuno-canalicular network (LCN) in unmineralized and mineralized human bone tissues. A 3D imaging routine was established based on FIB-SEM to image bone structure (mineralized and unmineralized) with a pixel resolution of 40 nm. To visualize the unmineralized collagenous matrix, samples were stained with iodine vapor. To maximize the information content, minimize the contribution of artifacts and therefore ease the segmentation, FIB-SEM volumes were pre-processed and analyzed with custom-developed image processing and analytical tools.

FIB-SEM imaging allowed for 3D datasets where all of the following features could be observed in each volume: (i) mineralized and unmineralized tissues, (ii) osteocyte network in both of mineralized and unmineralized regions and (iii) early mineralization foci. Hence, a fully developed osteocyte network was identified in the unmineralized matrix, whereby individually separated mineralization foci develop close to the mineralization front buried in the osteoid perfused by osteocyte canaliculi. The presence of such a dense network with high surface to volume ratio, with access to the bone matrix buried deep inside bone, suggests that the osteocyte network might play an essential role in the transport of mineral precursors from the Haversian canal to the mineralization front.

More importantly, it was observed, for the first time based on current literature, that mineral does not precipitate in the immediate vicinity of the canaliculi as an unmineralized region was found around canaliculi. This phenomenon was also confirmed quantitatively with probability density distribution (PDD) graphs in which it is systematically observed that the probability of finding unmineralized voxels adjacent to the canaliculi surface was substantially higher than for mineralized voxels. Considering the widespread presence and different functions of non-collagenous proteins (NCPs) in bone, it is proposed that the action of these proteins as mineralization inhibitors might be responsible for the existence of this mineral-free "halo zone" around the canaliculi which can suggest that the canaliculi are involved in this process by local transport and release of NCPs. One possible advantage of preserving an unmineralized region around the canaliculi might be that mineral precursors can diffuse more easily through the matrix, as they are not blocked immediately by a mineralized matrix at the canaliculi surface.

Moreover, the degree of mineralization, the size, the location, and the orientation of mineralization foci, which are the early components of the mineralization process, were measured. This is of particular importance as their organization with respect to the Haversian canal, the LCN, and collagen fibrils can explain the primary mineralization phase, where formation and growth of foci occur until a dense mineralized matrix is formed. The PDD graphs revealed that the mineralization degree of the foci was constant with distance to the canaliculi surface, which was consistent with preliminary results of the foci

size distribution that showed that foci size was almost constant with distance to the canaliculi. The fact that minerals form at a certain distance to the canaliculi not adjacent to their surface shows that simple diffusion of mineral precursors cannot be responsible for transport and deposition of minerals. It was also observed that foci are elongated parallel to the collagen fibrils long axis, which can be a key observation for the understanding of the mechanisms governing foci formation. In general, the observation of foci at the mineralization front is consistent with the studies that reported two stages of mineralization, namely primary and secondary mineralization phases [17]. In the former, formation and growth of foci dictate the rate of mineralization, while in the latter, mineral crystal growth is the dominant parameter of mineralization kinetics.

Thanks to the high-resolution 3D FIB-SEM images, a new "mineralization front-like structure" was discovered at the canaliculi surface that revealed the course of mineralization is occurring at different scales; i) At micro-scale, near the Haversian canal, where a ~3.67 µm wide front is visible and ii) at the nanoscale, near the canaliculi where a few hundred nanometer wide front is seen. Differences between these fronts, such as absence/lack of mineralized matrix close to the canals, formation/no formation of new matrix, and well-defined/ill-defined shape of the fronts, indicate different cellular activities in the early stage of mineralization. At the Haversian canal front, osteoblasts have been widely studied, and their functions for deposition of the unmineralized collagen matrix, secretion of NCPs, and production of matrix vesicles (MVs) are well documented. However, at the canaliculus front, osteocytes might take action by secreting inhibitors, a function that is mostly unknown and needs further studies for gaining more in-depth insights.

From a methodological point of view, in order to obtain the results mentioned above, new experimental approaches were established for this work. For the visualization of soft tissues, an iodine staining method was developed in which the iodine was used to infiltrate the samples from the vapor phase, and the protocol was optimized in terms of time and amount of iodine to enhance Z contrast of the unmineralized matrix homogeneously and deeply below the sample surface. The efficacy of the staining method was evaluated with ESEM and FIB-SEM, which were used to assess respectively the surface and staining depth inside samples. The visual criterion for this was to stain the unmineralized matrix until it became brighter than the embedding material (PMMA) but remained darker than the mineralized matrix. Owing to the reaction between the iodine and the carbon-carbon double bonds in the biological tissues such as collagen, the protocol can be used in future studies for other bone/soft tissue visualization, particularly where discernible contrast between unmineralized tissue and embedding material is needed. Moreover, iodine staining from the vapor phase can be conducted on the embedded samples what might be a great advantage to study permanently preserved/archival samples.

Finally, an analytical tool was developed to realize the involvement of the canalicular network in the mineralization process. Based on the calculated distance values from the LCN and the Haversian canal, and the grey values of the mineralized and the unmineralized voxels, a grey value-distance correlation was generated that provided PDD graphs of voxels with different degree of mineralization at different distances. In this process, the effect of geometry (i.e., the issue of the increasing number of voxels with distance from the canaliculi surface) on the density distribution of voxels was corrected for, which could be otherwise misleading in the interpretation of 3D datasets. Therefore, PDD graphs can be useful in future works for the evaluation of 3D nanometric resolution images such as FIB-SEM and nano-CT datasets.

Chapter 7

Outlook

In order to study the early stage of mineralization, visualization and characterization of the soft tissue where the foci are formed are essential. The developed iodine staining procedure was a valuable method for visualization of the unmineralized matrix. However, it was not selective in the staining of different organic components, and therefore, presence or absence of matrix vesicles (MVs) or non-collagenous proteins (NCPs) could not be confirmed. Nonetheless, the absence of these organic components can be due to the dehydration of the samples with ethanol during sample preparation. Hence, new staining protocols should be considered for future work that can be used solely or be combined with iodine staining protocol to uncover new compartments of the unmineralized matrix that are potentially playing a role in the mineralization. Many staining protocols have been documented for enhancing the contrast of soft tissue by electron microscopy, such as osmium tetroxide and uranyl acetate, which can be used for a more selective outcome. Besides, cryogenic microscopy is also beneficial in this regard as it provides images of the samples in near-native conditions and eliminates artifacts generated because of the ion diffusion and mineral dissolution/crystallization during sample preparation [19]. High-pressure freezing, which is commonly used for cryo-microscopy, can keep the supersaturation state of the matrix and might preserve calcium-bound complexes. It is not straightforward to prepare cryo-samples of human bone tissue, and therefore, probably working on animal models such as chicken embryo, turkey tendon, and zebra fish can provide new findings of the phase, shape, and size of mineral precursors.

To study mineralization foci in more detail, methods with higher imaging resolution are required (down to a few nanometers), especially those that can be conducted with FIB-SEM, stimulated emission depletion (STED) microscopy and transmission electron microscopy (TEM). With FIB-SEM, obtaining higher resolution datasets in comparison to what was acquired in this work for a large field of view (20×25×40 μm^3), might take long acquisition times. However, that can be compensated with the selection of a small field of view (e.g., 1×1×1 μm^3) in which several foci are still imaged during reasonable acquisition times. STED, the recently developed technology of the CLSM technique that also provides 3D datasets, might be useful for imaging the small compartments such as mineralization foci. The sample needs to be stained with chemicals such as calcein and Fluorescein-Dextran, which are used for staining of minerals [99]. Another high-resolution technique, such as TEM, provides images with a few angstrom resolution and can reveal the morphology of foci and their interaction with the collagen fibrils. The main drawback of this technique is that commonly 2D images of the samples are obtained, and the TEM lamellae are not usually thicker than a few hundred nanometers for tomography. Hence, a combination of the methods mentioned above would be worthwhile for a deeper understanding of the foci formation and growth as they can provide information about the intrafibrillar and interfibrillar mineralization, differences between smaller foci and

larger ones in terms of the degree of mineralization, morphology, and orientation and it might also help to unveil where the foci are originated from (such as MVs and NCPs).

The halo zone around the canaliculi at the mineralization front in human bone was observed in this work for the first time. However, it could not be determined if NCPs exist there or not. For further investigation of this phenomenon, immunostaining of forming bone samples might be helpful to observe the potential role of NCPs in inhibition of mineralization. Boukpessi *et al.* compared normal bone with those who had X-linked hypophosphatemia (XLH) that causes hypomineralization of bone and found out that osteopontin is localized around osteocyte lacunae and canaliculi where lack of mineralization is clearly observed (Fig. 7.1) [132].

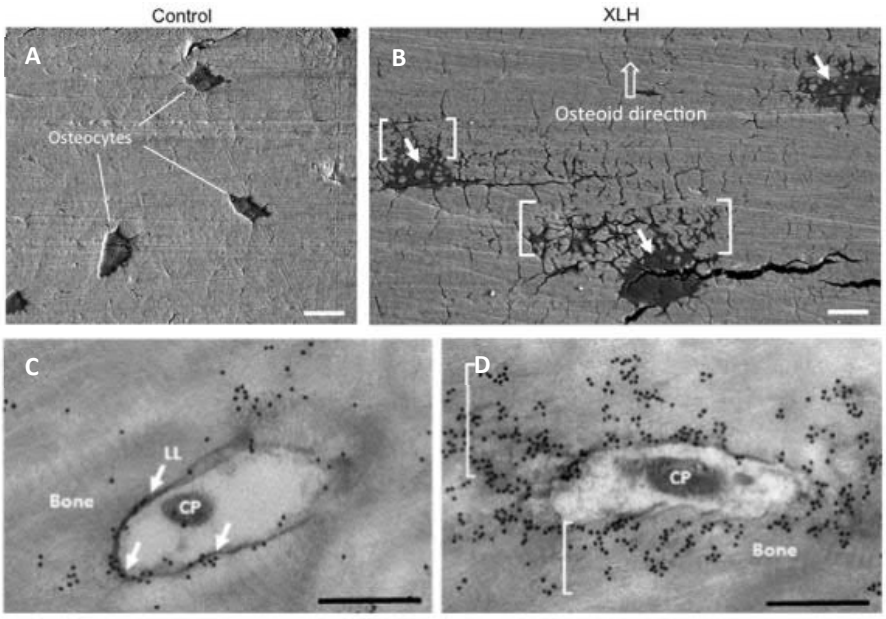

Fig. 7.1. Backscattered electron images of normally mineralized bone (A) and XLH bone that causes hypomineralization, the so-called periosteocytic "halos" (B). Transmission electron microscopy images of the canaliculi immunostained with gold nanoparticles for normal (C) and XLH bone (D) that reveals localization of osteopontin around canaliculi in the latter. Scale bars for A and B = 10 μm, for C and D = 0.5 μm. Adapted with permission from [132].

Later stages of mineralization also plays a role in the mechanical properties of bone as it makes the bone tissue mature by increasing the calcium content to its maximum level (from 70% to 100% [17]). It has been suggested that this happens with the aid of the lacuno-canalicular network (LCN) as transport routes for mineral precursors [73]. Studying this stage of mineralization was not the focus of this study, however, with the correlation analytical tool (PDD graphs), it can be investigated to comprehend what mechanisms are behind the progression of mineralization. One hypothesis is the diffusion of mineral precursors from the

LCN into the collagen matrix [23]. The preliminary results, however, show that it is not always the case as the PDD is constant with the distance from the canaliculi (see chapter 8, Fig. 8.12). If diffusion was the only mechanism for transport of mineral precursors, a higher concentration at the surface of the LCN was expected that would result in a downward PDD with distance. The constant PDD might be explained by the existence of secondary channels similar to what is observed in mineralizing turkey leg tendon [199], which can have the function of transporting mineral precursors further away from the LCN.

As a final point, by working with different imaging techniques, correlative imaging with CLSM and FIB-SEM was found to be practical and informative to visualize the LCN in bone. When analyzing the LCN in the vicinity of mineralized osteocyte lacunae, structures likely corresponding to the mineralized LCN regions were detected (Fig. 7.2.A). It was hypothesized that these are regions where the LCN is not visible after rhodamine staining, as reported by Repp *et al.* [9] (Fig. 7.2.B). The results gained with FIB-SEM will be valuable for the interpretation of the CLSM investigation and will shed light on the presence of LCN-free regions that might not be available for mechanosensing or endocrine purposes. Using CLSM, regions where canaliculi bridge the cement line can also be identified. They can be considered for FIB-SEM investigations to determine their morphology and compare them to the normal, non-bridging, canaliculi (Fig. 7.2.C).

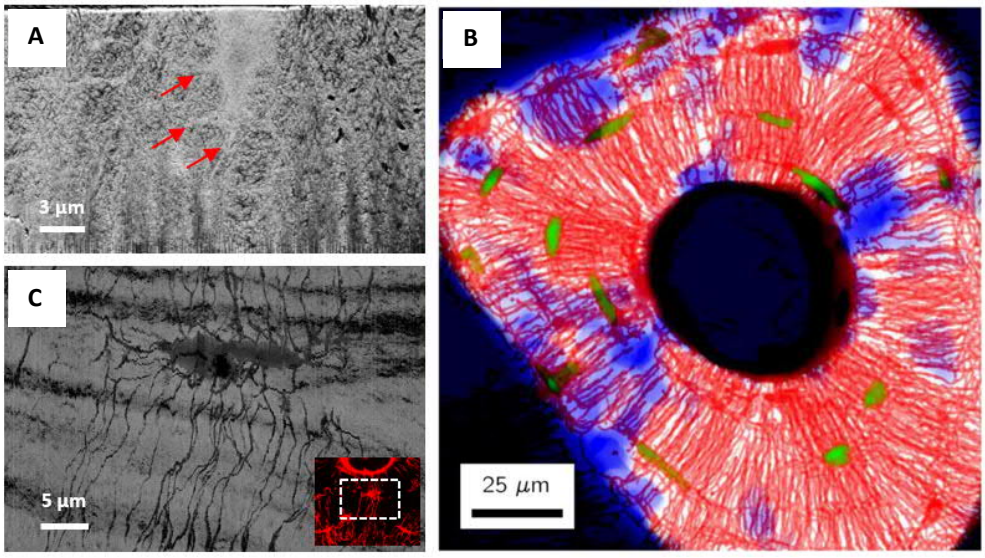

Fig. 7.2. A) A backscattered electron image of the mineralized LCN obtained by FIB-SEM (the arrows indicate the mineralized canaliculi). B) Free of network regions (marked with blue) in an osteonal canaliculi network. Adapted with permission from [9]. C) Bridging canaliculi at the cement line, which are shown by the projection of a FIB-SEM dataset. The inset shows the CLSM image of the bridging canaliculi at the interface of two osteons.

Chapter 8

Appendix

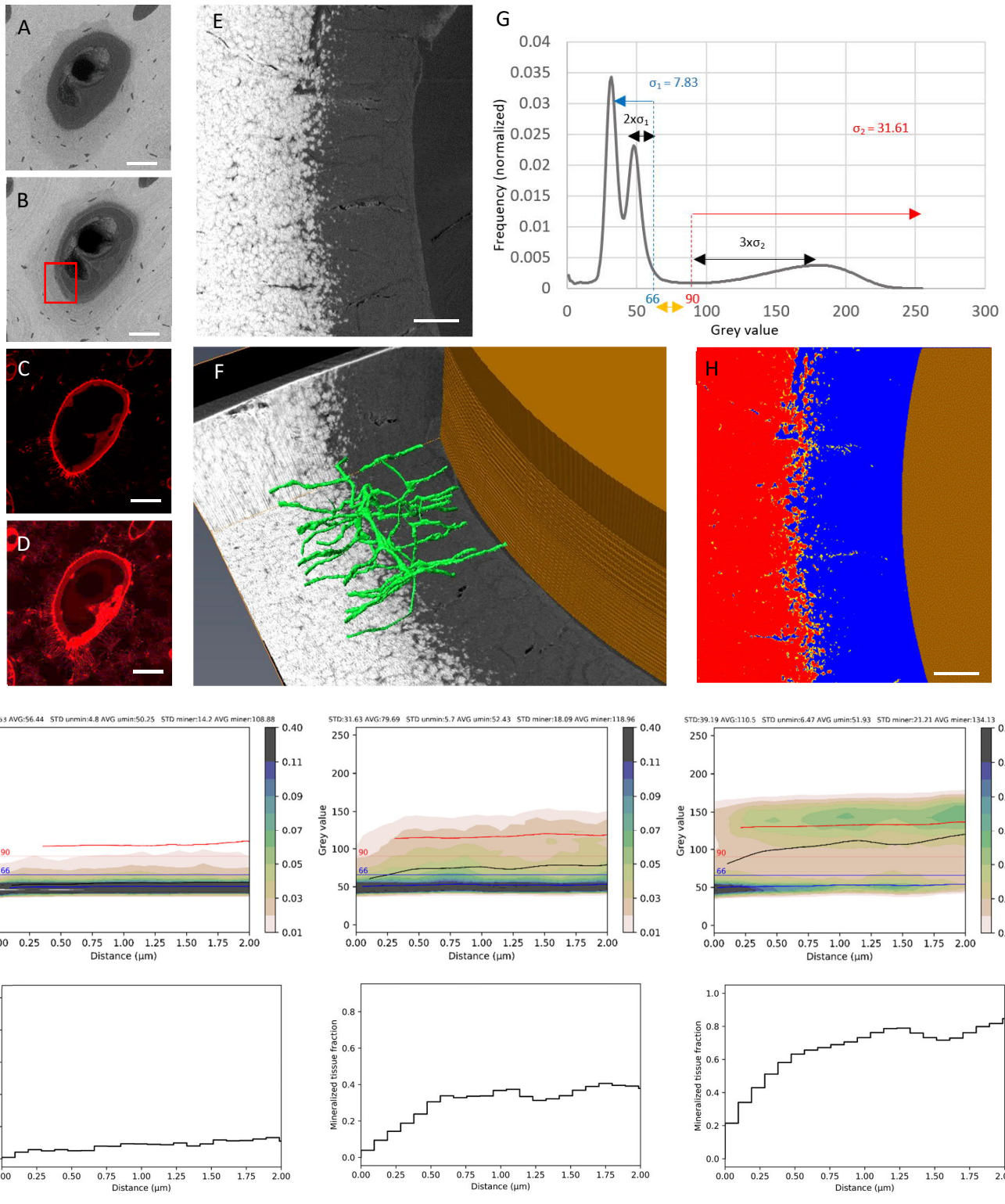
A
B
C
D
E
F
G
H
I
J
Frequency (normalized)
Grey value
σ1 = 7.83
2xσ1
σ2 = 31.61
3xσ2
66
90
Distance (µm)
Mineralized tissue fraction

Fig. 8.1. Individual FM38_Osteon #1. ESEM images A) before and B) after iodine staining (the red rectangle is the ROI considered for FIB-SEM imaging). CLSM images of C) the osteoid and D) the lacuno-canalicular network (LCN) at the mineralized matrix. E) A single BSE image acquired during FIB-SEM imaging of a volume of ~20×25×40 μm^3. F) 3D rendering of the LCN and Haversian canal. G) Histogram of the FIB-SEM dataset (BSE images) showing thresholds of mineralized (90) and unmineralized (66) matrices. These thresholds are calculated based on three and two times standard deviation (the black double arrows) from the maxima of the mineralized and the unmineralized peaks, respectively. The red arrow indicates the mineralized region (above grey value 90), while the blue arrow shows the unmineralized region (below grey value 66). The yellow double arrow shows the region that cannot be assigned to either the mineralized or to the unmineralized matrices. σ_1 and σ_2 are the standard deviations for the unmineralized and the mineralized peaks, respectively. H) The BSE image colored based on the thresholds calculated in the histogram. The red pixels are mineralized, the blue pixels are unmineralized, and the brown pixels are the Haversian canal (compare different regions with the BSE image shown in E). Note that the yellow pixels are not assigned to either mineralized or unmineralized matrix. I) Probability density distribution (PDD) of subvolumes with low, medium, and high VFMM. J) VFMM graphs of the corresponding subvolumes. Scale bars for A, B, C, and D = 40 µm, for E and H = 4 µm.

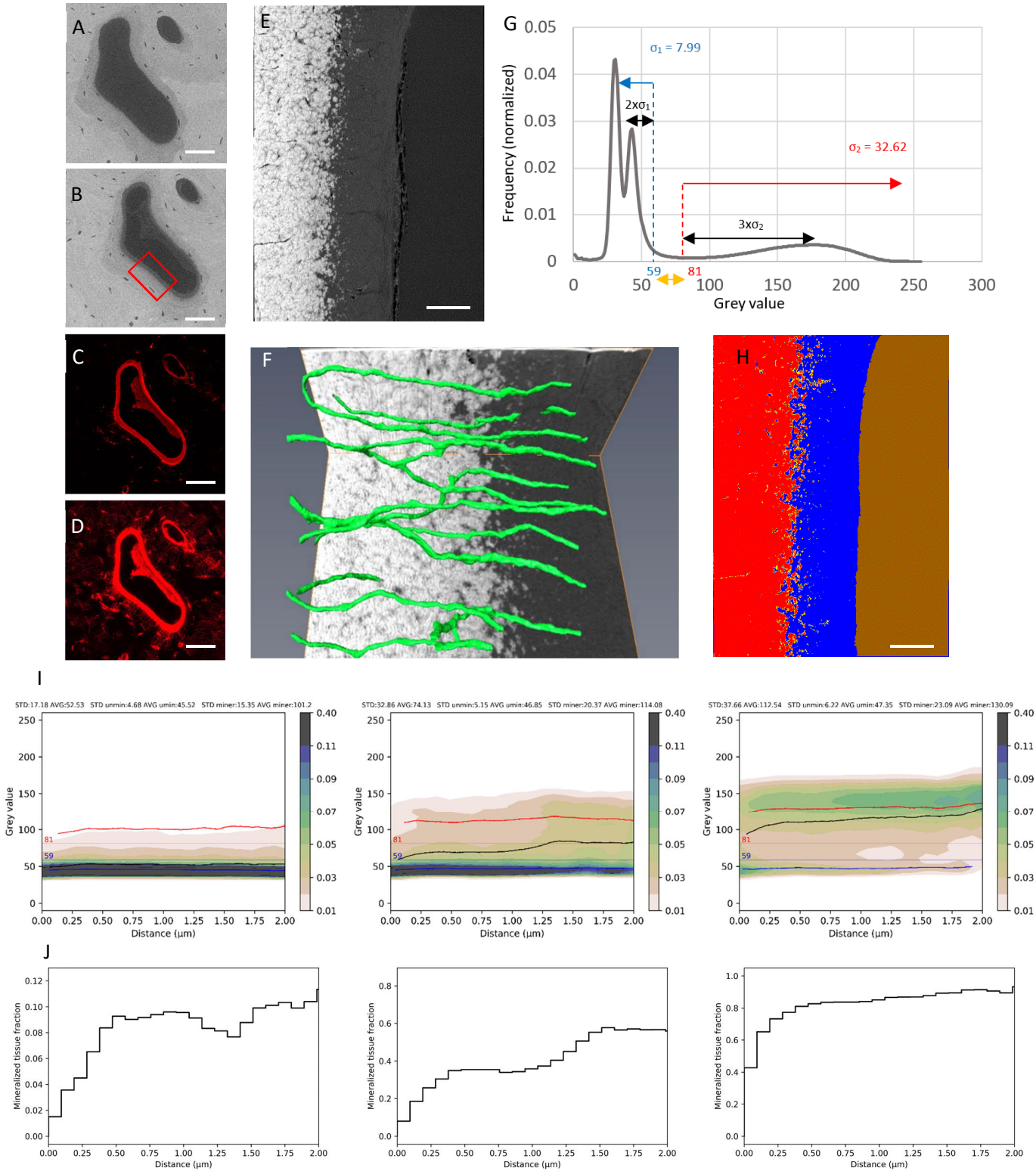

Fig. 8.2. Sample FM38_Osteon #2. The same type of data and analysis that were shown in Fig. 8.1 are presented. Scale bars for A, B, C, and D = 40 µm, for E and H = 4 µm.

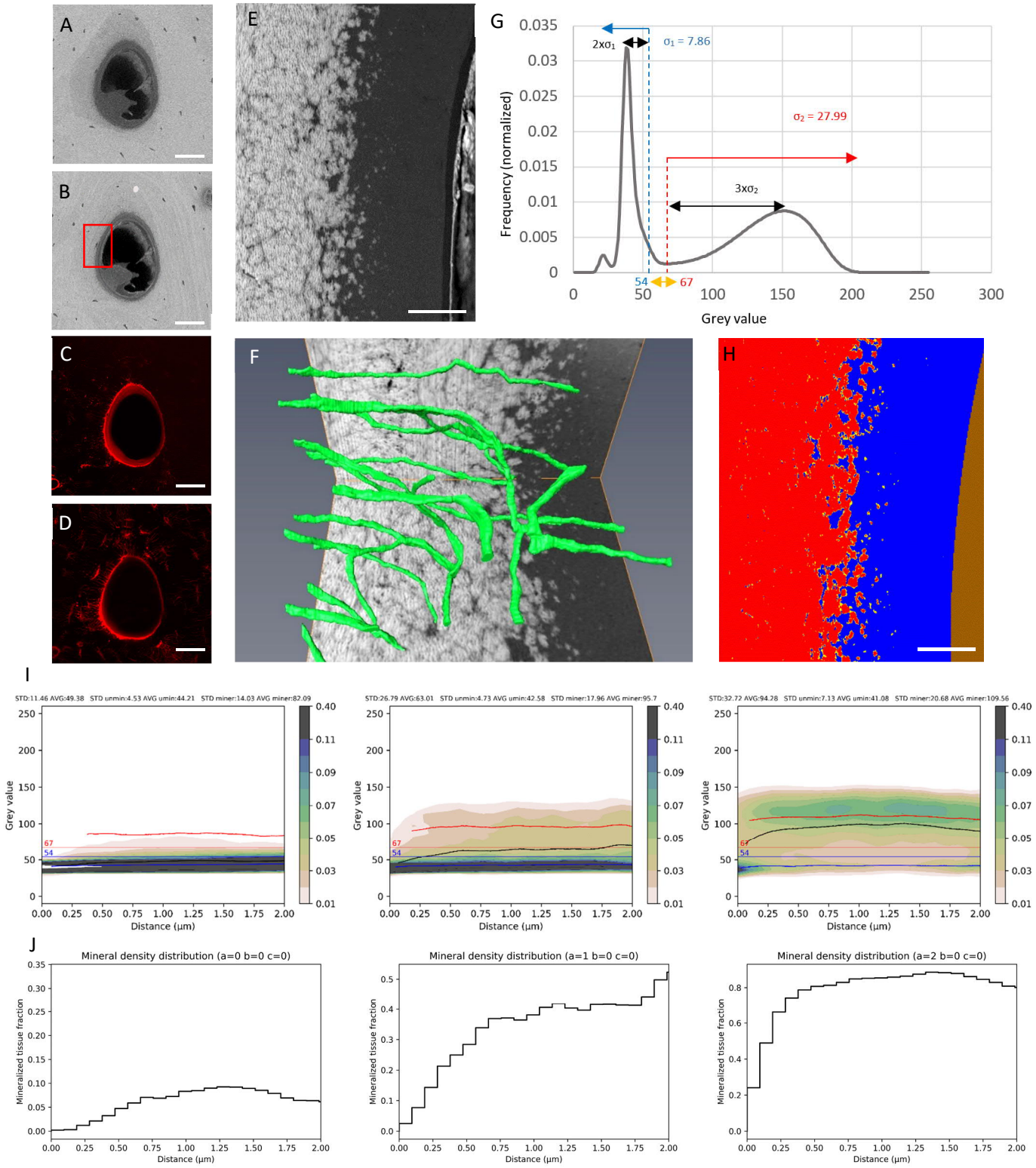

Fig. 8.3. Sample FM38_Osteon #3. The same type of data and analysis that were shown in Fig. 8.1 are presented. Scale bars for A, B, C, and D = 40 μm, for E and H = 4 μm.

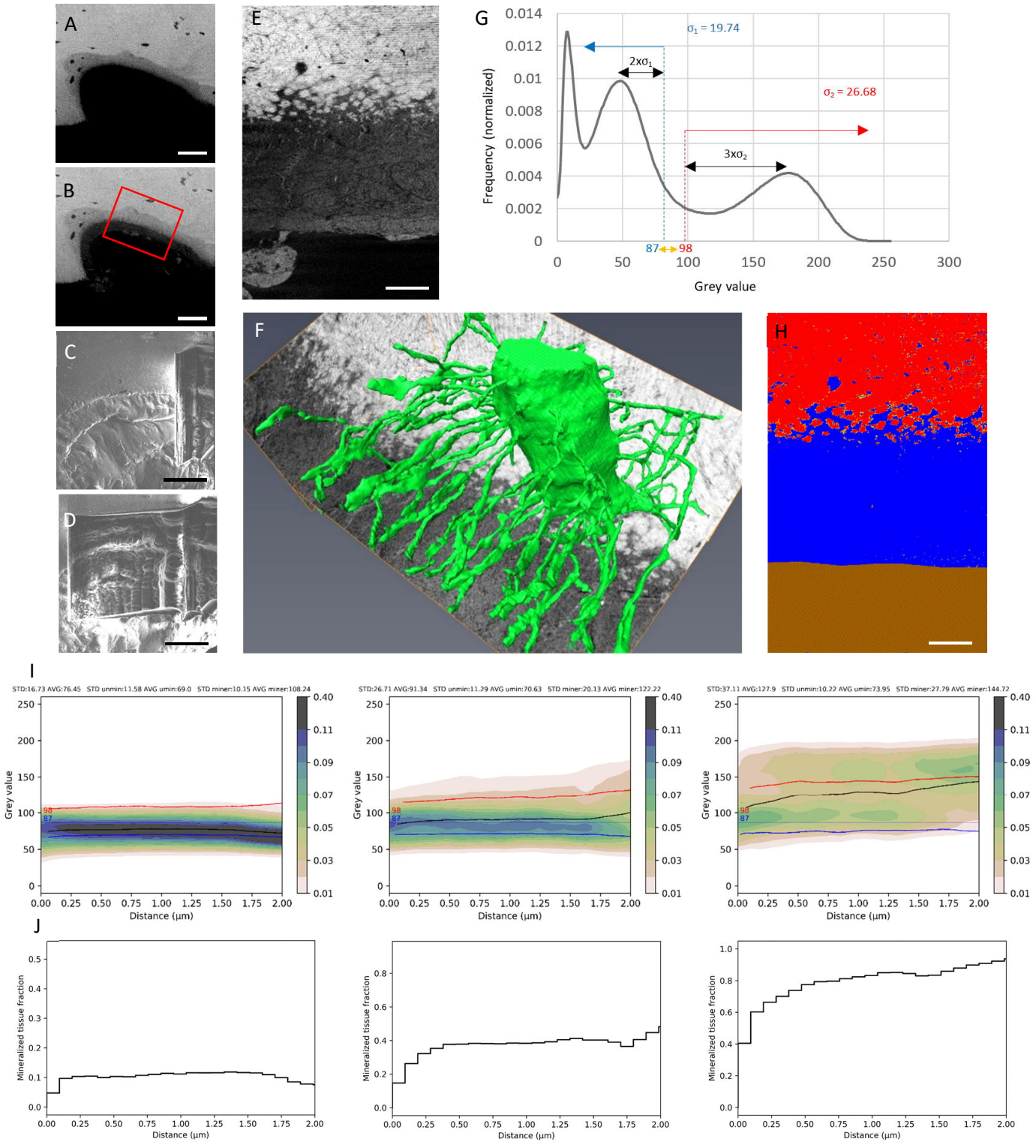

Fig. 8.4. Sample FM40_Osteon #1. The same type of data and analysis that were shown in Fig. 8.1 are presented (as CLSM images are not available for this sample, fib view of osteon before and after milling are substituted in C and D). Scale bars for A, B, C, and D = 40 µm, for E and H = 4 µm.

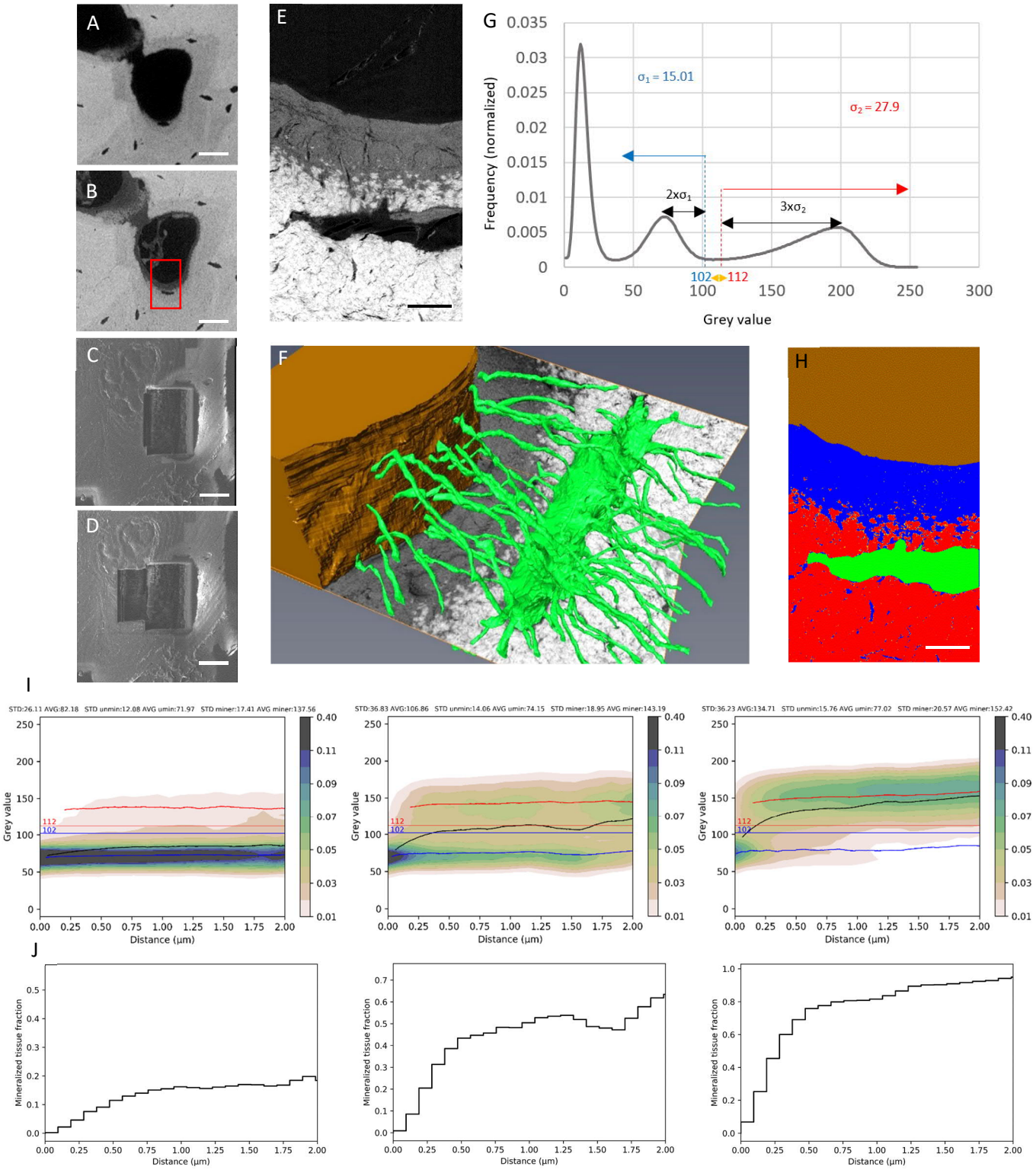

Fig. 8.5. Sample FM40_Osteon #2. The same type of data and analysis that were shown in Fig. 8.1 are presented (as CLSM images are not available for this sample, fib view of osteon before and after milling are substituted in C and D). Scale bars for A, B, C, and D = 40 µm, for E and H = 4 µm.

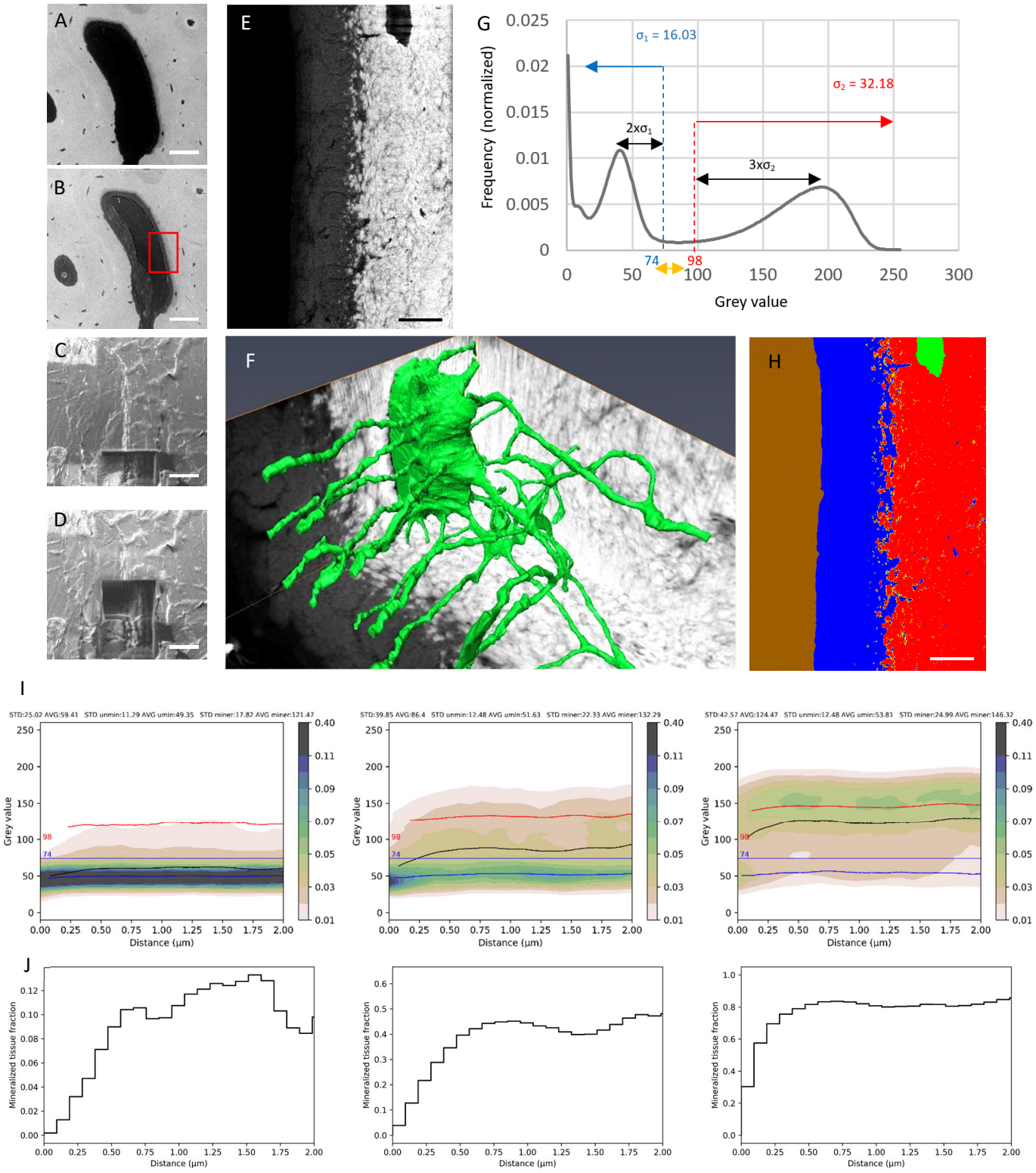

Fig. 8.6. Sample FM40_Osteon #3. The same type of data and analysis that were shown in Fig. 8.1 are presented (as CLSM images are not available for this sample, fib view of osteon before and after milling are substituted in C and D). Scale bars for A, B, C, and D = 40 µm, for E and H = 4 µm.

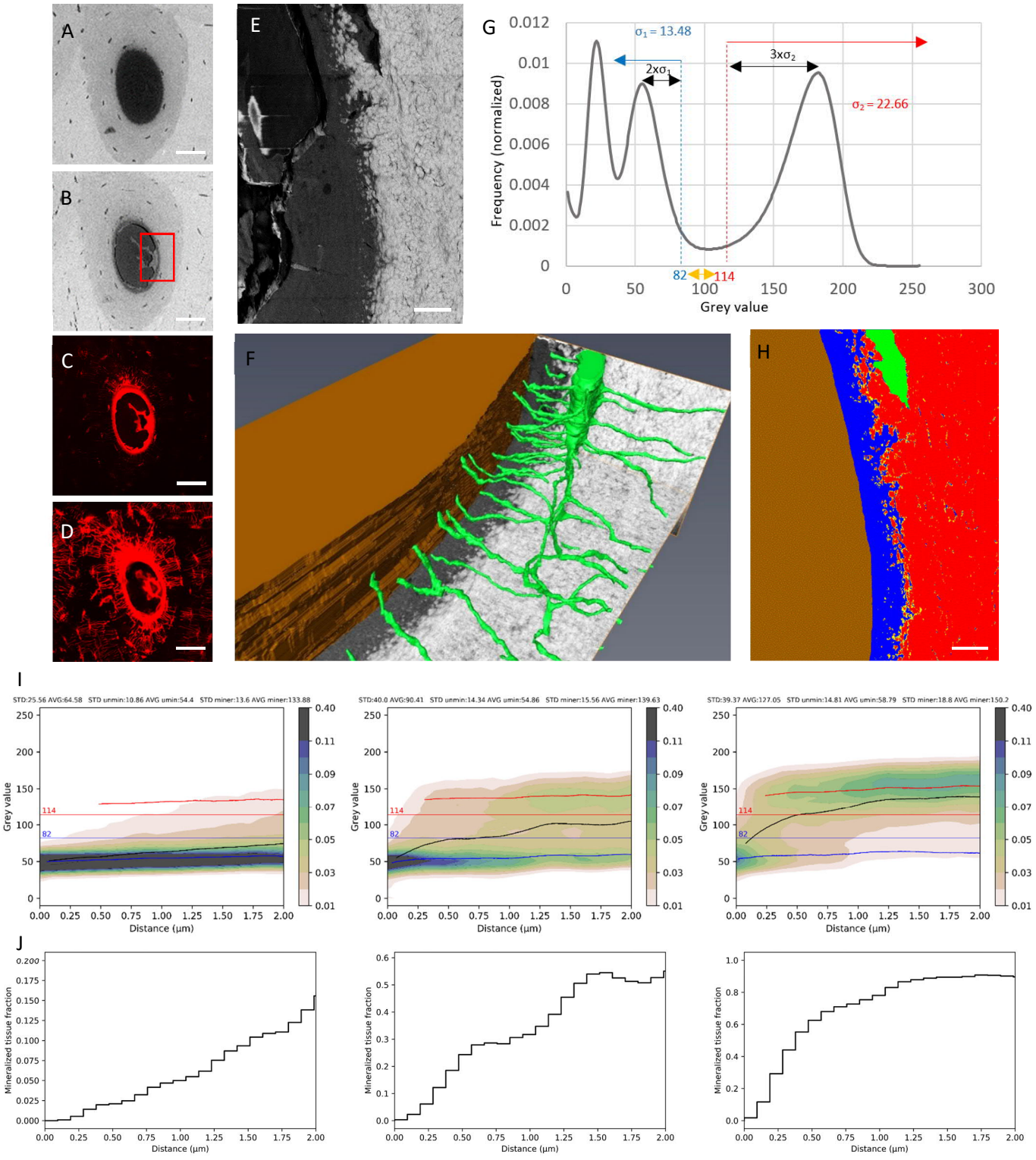

Fig. 8.7. Sample FM48_Osteon #1. The same type of data and analysis that were shown in Fig. 8.1 are presented. Scale bars for A, B, C, and D = 40 µm, for E and H = 4 µm.

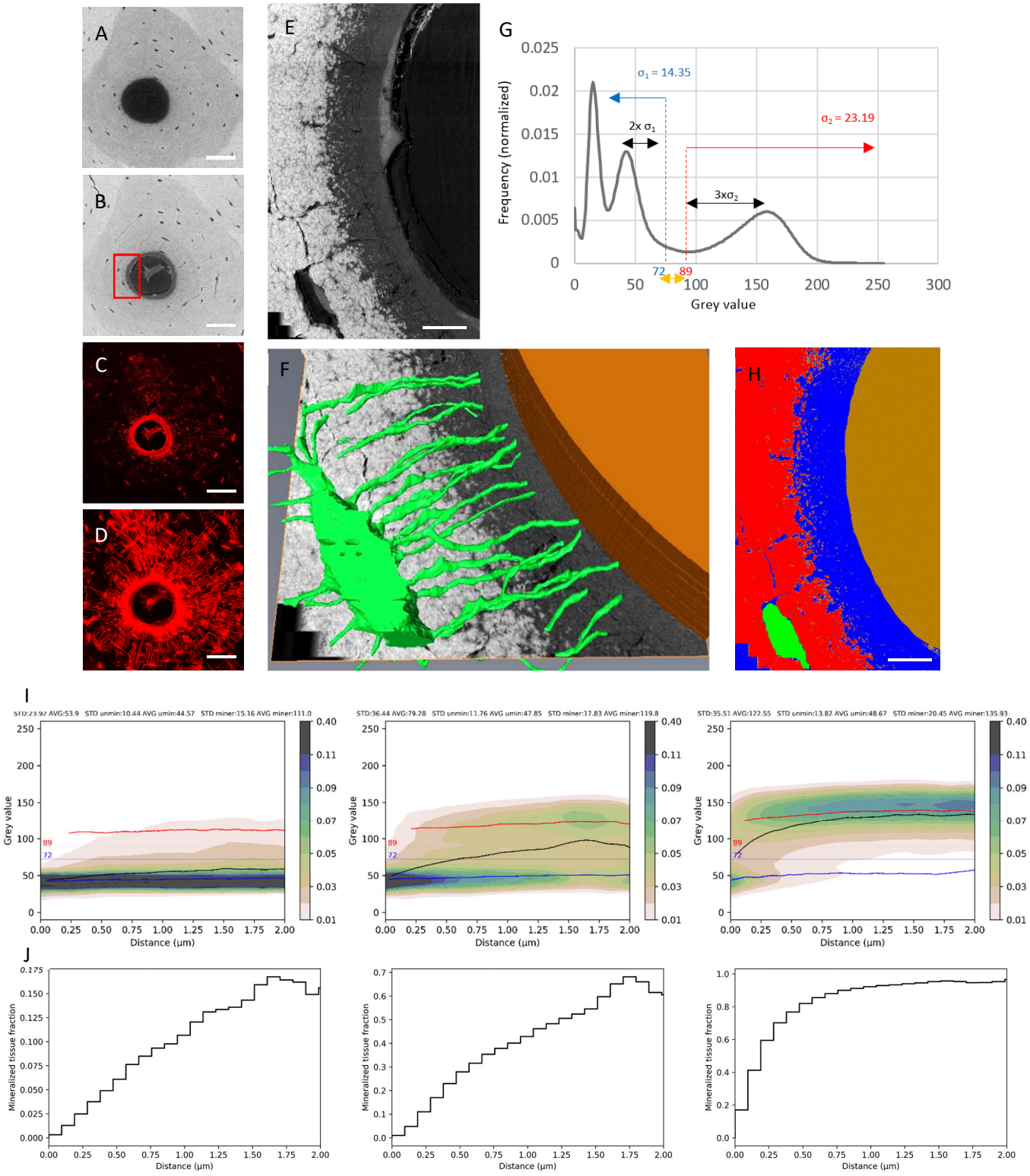

Fig. 8.8. Sample FM48_Osteon #2. The same type of data and analysis that were shown in Fig. 8.1 are presented. Scale bars for A, B, C, and D = 40 µm, for E and H = 4 µm.

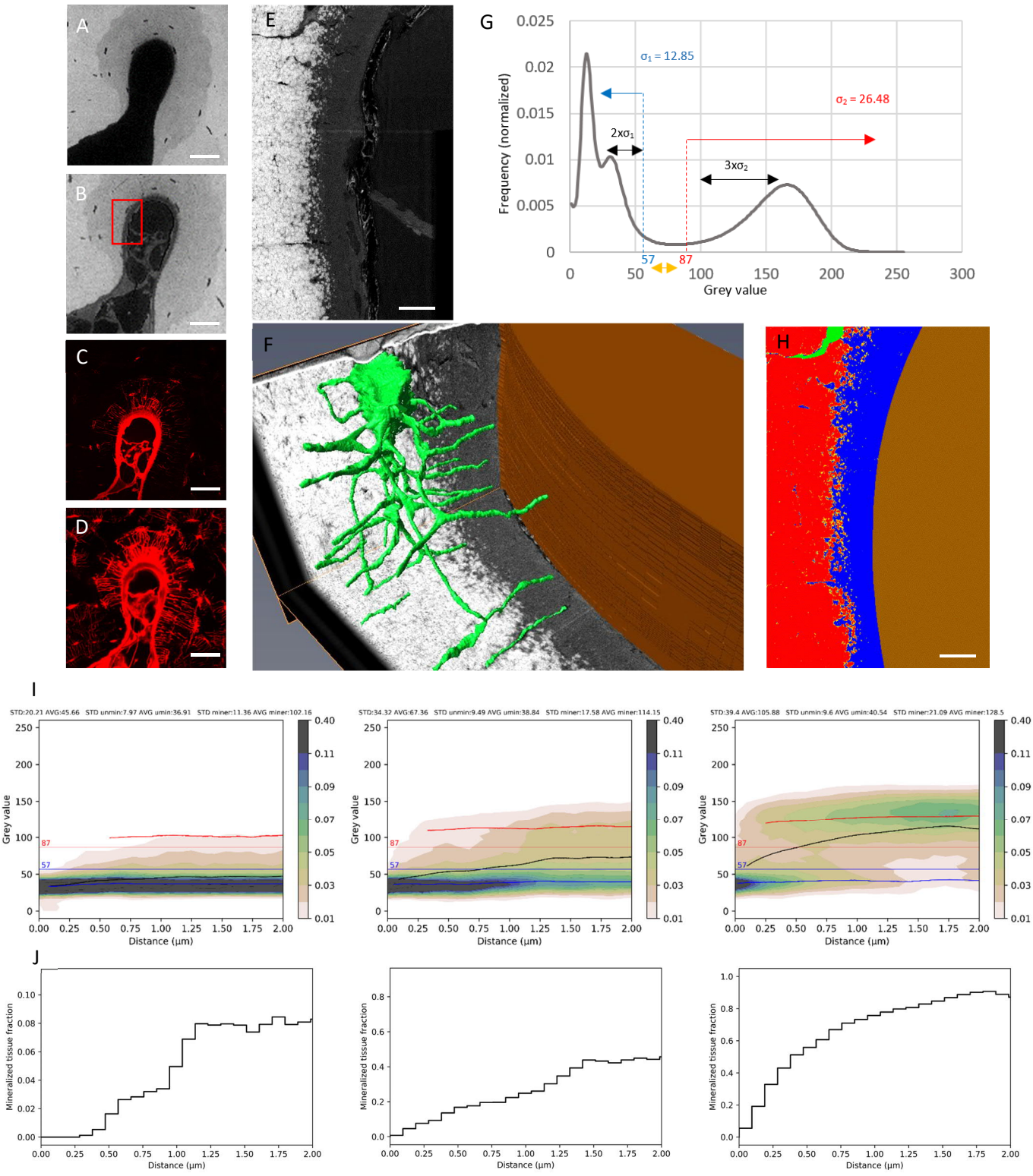

Fig. 8.9. Sample FM48_Osteon #3. The same type of data and analysis that were shown in Fig. 8.1 are presented. Scale bars for A, B, C, and D = 40 µm, for E and H = 4 µm.

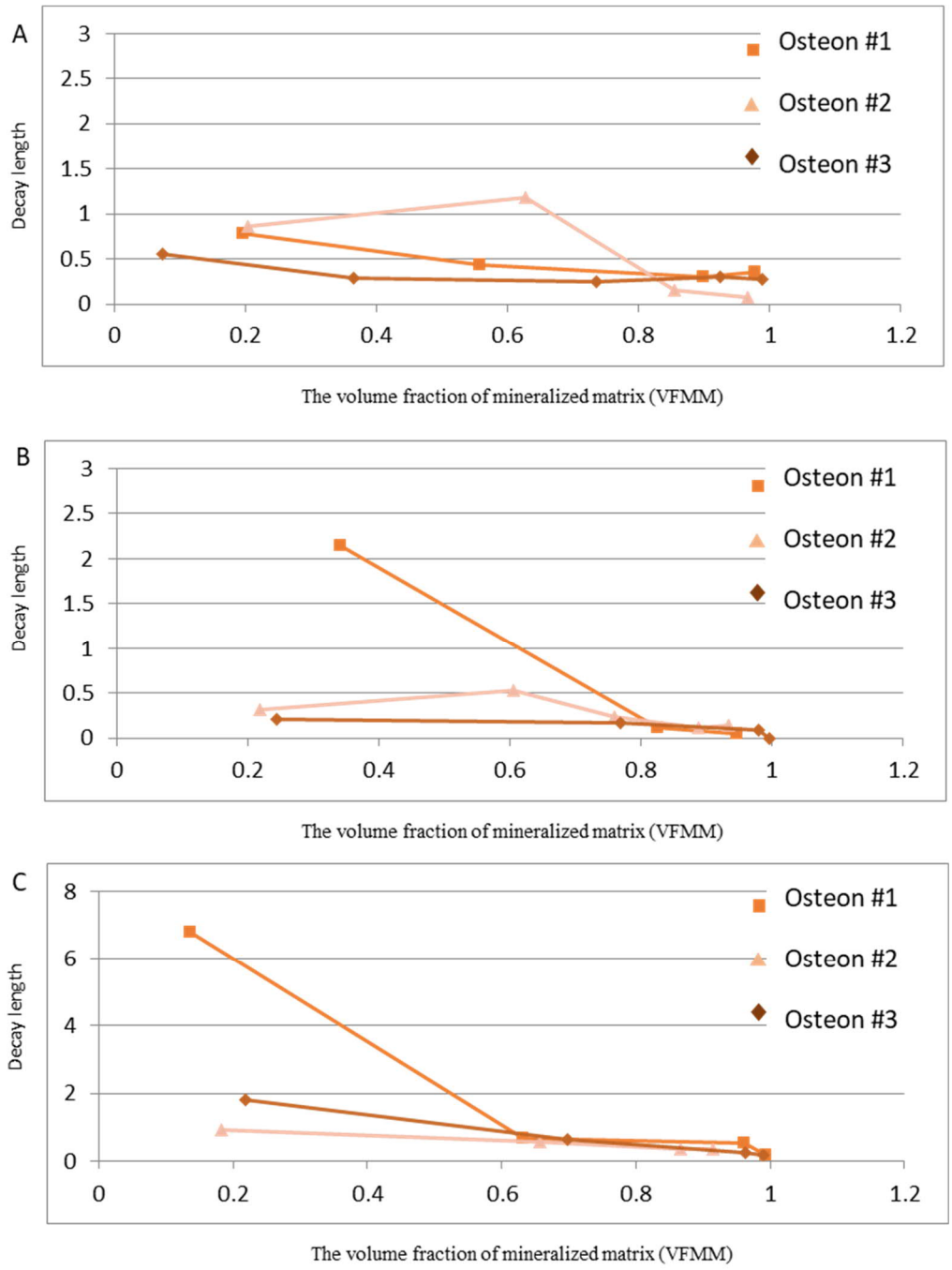

Fig. 8.10. Variation of decay length of exponential fits with the volume fraction of mineralized tissue for different samples, A) FM38, B) FM40, and C) FM48. As it was explained in section 4.4.3, the black curves in the probability density distribution (PDD) were fitted with exponential curves with formula $y = y_0 - A\exp(-\frac{x}{d})$ in which "d" is the decay length. The curves were used until 2 µm where the exponential fits reached a plateau.

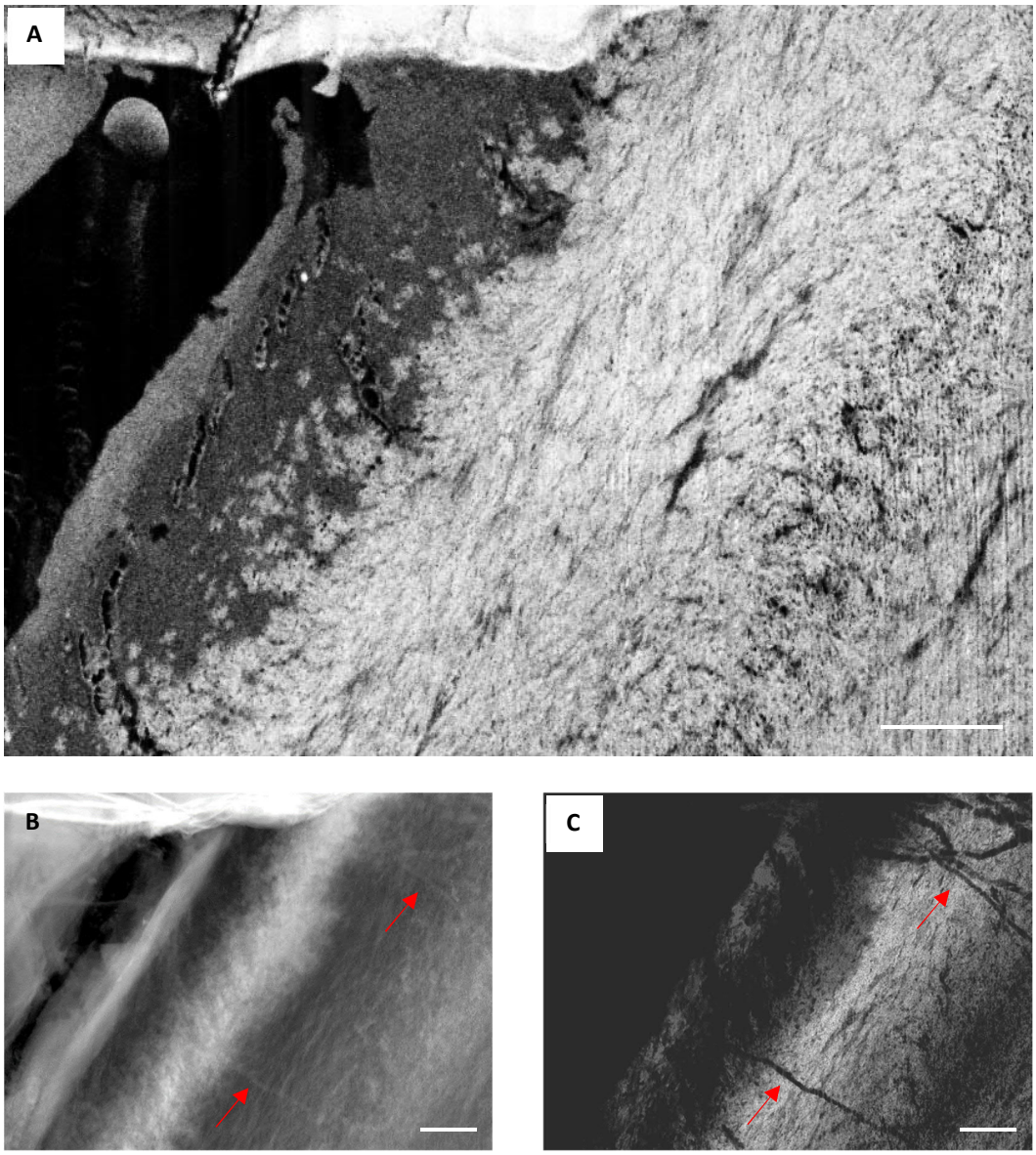

Fig. 8.11. A) A backscattered electron image of a FIB-SEM dataset of a forming osteon that contains the mineralized matrix, the mineralization front, osteoid, and the Haversian canal (PMMA black phase). The size of the dataset is 25×35×40 μm^3. Projection of the images of the dataset based on B) the standard deviation and C) the average. The arrows indicate a few canaliculi located within this region. Scale bars = 4 µm.

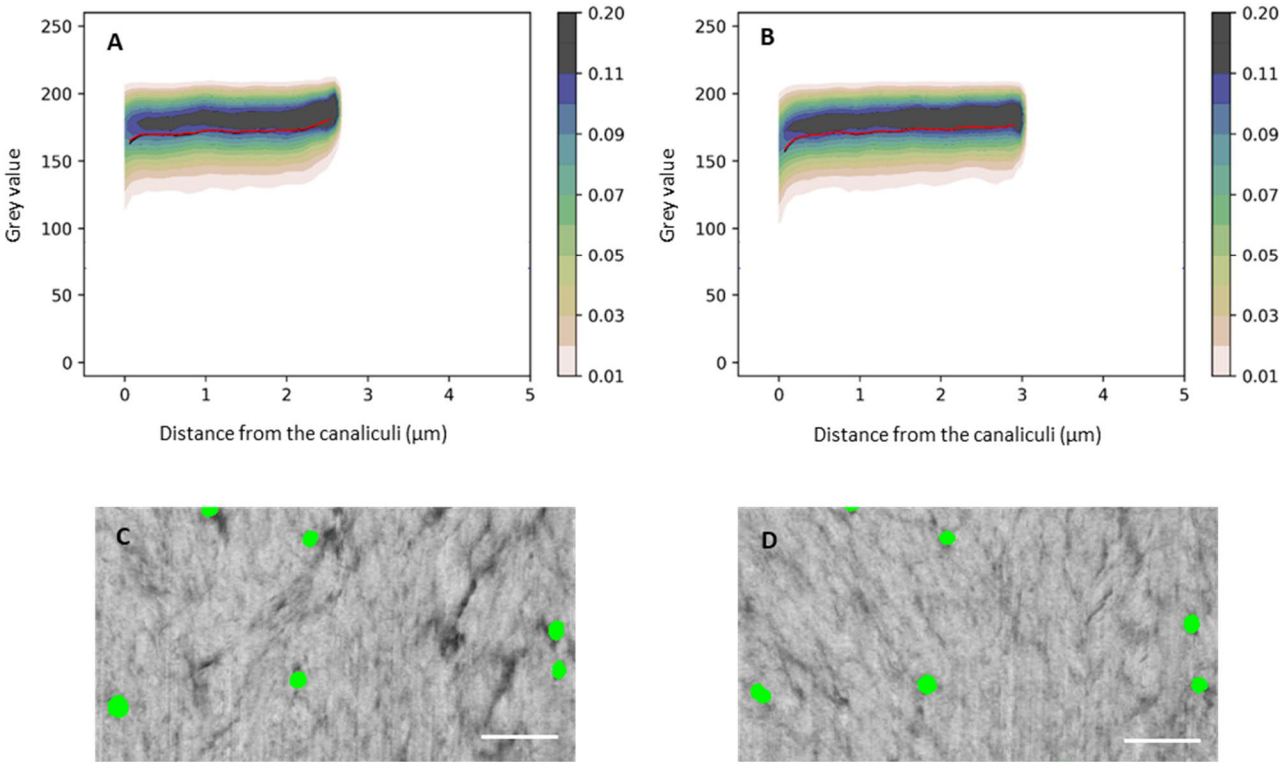

Fig. 8.12. A and B) PDD graphs of two subvolumes (from sample FM48_osteon #1) from almost fully mineralized regions (A: 98.43% and B: 99.39% VFMM) with respect to the distance to the canaliculi. C and D) Cross-sections of the canaliculi in the backscattered electron images of the corresponding FIB-SEM dataset. Scale bars = 2 µm.

Bibliography

1. Havers, C., *1691. Osteologia Nova.* Samuel Smith, London.
2. Fratzl, P. and R. Weinkamer, *Nature's hierarchical materials.* Progress in Materials Science, 2007. **52**(8): p. 1263-1334.
3. Marieb, E.N. and K. Hoehn, *Human anatomy & physiology*. 2007: Pearson Education.
4. Weiner, S. and H.D. Wagner, *The material bone: structure-mechanical function relations.* Annual Review of Materials Science, 1998. **28**(1): p. 271-298.
5. Schnitzler, C.M., *Bone quality: a determinant for certain risk factors for bone fragility.* Calcified tissue international, 1993. **53**(1): p. S27-S31.
6. Bonewald, L.F., *The amazing osteocyte.* J Bone Miner Res, 2011. **26**(2): p. 229-38.
7. Fratzl, P. and R. Weinkamer, *Hierarchical structure and repair of bone: deformation, remodelling, healing*, in *Self healing materials*. 2007, Springer. p. 323-335.
8. Reznikov, N., et al., *Three-dimensional imaging of collagen fibril organization in rat circumferential lamellar bone using a dual beam electron microscope reveals ordered and disordered sub-lamellar structures.* Bone, 2013. **52**(2): p. 676-83.
9. Repp, F., et al., *Spatial heterogeneity in the canalicular density of the osteocyte network in human osteons.* Bone Rep, 2017. **6**: p. 101-108.
10. Buenzli, P.R. and N.A. Sims, *Quantifying the osteocyte network in the human skeleton.* Bone, 2015. **75**: p. 144-50.
11. Ren, Y. and J.Q. Feng, *Osteocytes play a key role in the formation and maintenance of mineralized bone.* The FASEB Journal, 2017. **31**(1_supplement): p. 7.1-7.1.
12. Boskey, A.L., *Biomineralization: conflicts, challenges, and opportunities.* Journal of cellular biochemistry, 1998. **72**(S30–31): p. 83-91.
13. Wagermaier, W. and P. Fratzl, *Collagen*, in *Polymer Science: A Comprehensive Reference*. 2012. p. 35-55.
14. Nanci, A., *Ten Cate's Oral Histology-E-Book: Development, Structure, and Function*. 2017: Elsevier Health Sciences.
15. Gower, L.B., *Biomimetic model systems for investigating the amorphous precursor pathway and its role in biomineralization.* Chemical reviews, 2008. **108**(11): p. 4551-4627.
16. Combes, C., S. Cazalbou, and C. Rey, *Apatite Biominerals.* Minerals, 2016. **6**(2).
17. Roschger, P., et al., *Bone mineralization density distribution in health and disease.* Bone, 2008. **42**(3): p. 456-66.
18. Barragan-Adjemian, C., et al., *Mechanism by which MLO-A5 late osteoblasts/early osteocytes mineralize in culture: similarities with mineralization of lamellar bone.* Calcif Tissue Int, 2006. **79**(5): p. 340-53.
19. Mahamid, J., et al., *Bone mineralization proceeds through intracellular calcium phosphate loaded vesicles: a cryo-electron microscopy study.* J Struct Biol, 2011. **174**(3): p. 527-35.
20. Boonrungsiman, S., et al., *The role of intracellular calcium phosphate in osteoblast-mediated bone apatite formation.* Proc Natl Acad Sci U S A, 2012. **109**(35): p. 14170-5.
21. Reznikov, N., et al., *Fractal-like hierarchical organization of bone begins at the nanoscale.* Science, 2018. **360**(6388).

22. Hasegawa, T., et al., *Three-dimensional ultrastructure of osteocytes assessed by focused ion beam-scanning electron microscopy (FIB-SEM).* Histochem Cell Biol, 2018. **149**(4): p. 423-432.
23. Hesse, B., et al., *Canalicular network morphology is the major determinant of the spatial distribution of mass density in human bone tissue: evidence by means of synchrotron radiation phase-contrast nano-CT.* J Bone Miner Res, 2015. **30**(2): p. 346-56.
24. Kerschnitzki, M., et al., *Bone mineralization pathways during the rapid growth of embryonic chicken long bones.* J Struct Biol, 2016. **195**(1): p. 82-92.
25. Mahamid, J., L. Addadi, and S. Weiner, *Crystallization pathways in bone.* Cells Tissues Organs, 2011. **194**(2-4): p. 92-7.
26. Landis, W.J. and R. Jacquet, *Association of calcium and phosphate ions with collagen in the mineralization of vertebrate tissues.* Calcif Tissue Int, 2013. **93**(4): p. 329-37.
27. Lu, Y., et al., *A novel image registration approach via combining local features and geometric invariants.* PLoS One, 2018. **13**(1): p. e0190383.
28. Loeber, T.H., et al., *Reducing curtaining effects in FIB/SEM applications by a goniometer stage and an image processing method.* Journal of Vacuum Science & Technology B, Nanotechnology and Microelectronics: Materials, Processing, Measurement, and Phenomena, 2017. **35**(6).
29. Peterlik, H., et al., *From brittle to ductile fracture of bone.* Nat Mater, 2006. **5**(1): p. 52-5.
30. Currey, J.D., *Bones: structure and mechanics*. 2006: Princeton university press.
31. Roschger, P., B.M. Misof, and K. Klaushofer, *Basic Aspects of Bone Mineralization*, in *Osteoporosis*. 2020. p. 89-113.
32. Kim, S.W., et al., *Intermittent parathyroid hormone administration converts quiescent lining cells to active osteoblasts.* J Bone Miner Res, 2012. **27**(10): p. 2075-84.
33. Miller, S.C., B. Bowman, and W. Jee, *Bone lining cells: structure and function.* Scanning microscopy, 1989. **3**(3): p. 953-60; discussion 960-1.
34. Nango, N., et al., *Osteocyte-directed bone demineralization along canaliculi.* Bone, 2016. **84**: p. 279-288.
35. Gay, C., V. Gilman, and T. Sugiyama, *Perspectives on osteoblast and osteoclast function.* Poultry science, 2000. **79**(7): p. 1005-1008.
36. Dallas, S.L., M. Prideaux, and L.F. Bonewald, *The osteocyte: an endocrine cell ... and more.* Endocr Rev, 2013. **34**(5): p. 658-90.
37. Kato, Y., et al., *Establishment of an osteoid preosteocyte-like cell MLO-A5 that spontaneously mineralizes in culture.* Journal of Bone and Mineral Research, 2001. **16**(9): p. 1622-1633.
38. Klein-Nulend, J. and L.F. Bonewald, *The osteocyte*, in *Principles of Bone Biology*. 2020. p. 133-162.
39. Rehfeld, A., M. Nylander, and K. Karnov, *Bone Tissue*, in *Compendium of Histology*. 2017, Springer. p. 157-185.
40. Fratzl, P., *Collagen: structure and mechanics, an introduction*, in *Collagen*. 2008, Springer. p. 1-13.
41. Fratzl, P., et al., *Fibrillar structure and mechanical properties of collagen.* Journal of structural biology, 1998. **122**(1-2): p. 119-122.
42. Radhakrishnan, S., et al., *Collagen Based Biomaterials for Tissue Engineering Applications: A Review*, in *Processes and Phenomena on the Boundary Between Biogenic and Abiogenic Nature*. 2020, Springer. p. 3-22.
43. Ricard-Blum, S., *The collagen family.* Cold Spring Harbor perspectives in biology, 2011. **3**(1): p. a004978.
44. Eyre, D.R., *Collagen: molecular diversity in the body's protein scaffold.* Science, 1980. **207**(4437): p. 1315-1322.
45. Daneault, A., et al., *Biological effect of hydrolyzed collagen on bone metabolism.* Critical Reviews in Food Science and Nutrition, 2017. **57**(9): p. 1922-1937.

46. Bella, J., *Collagen structure: new tricks from a very old dog.* Biochemical Journal, 2016. **473**(8): p. 1001-1025.
47. Baum, J. and B. Brodsky, *Folding of peptide models of collagen and misfolding in disease.* Current opinion in structural biology, 1999. **9**(1): p. 122-128.
48. Petruska, J.A. and A.J. Hodge, *A subunit model for the tropocollagen macromolecule.* Proceedings of the National Academy of Sciences of the United States of America, 1964. **51**(5): p. 871.
49. Álvarez, J., et al., *Different bone growth rates are associated with changes in the expression pattern of types II and X collagens and collagenase 3 in proximal growth plates of the rat tibia.* Journal of Bone and Mineral Research, 2000. **15**(1): p. 82-94.
50. Keene, D.R., L.Y. Sakai, and R.E. Burgeson, *Human bone contains type III collagen, type VI collagen, and fibrillin: type III collagen is present on specific fibers that may mediate attachment of tendons, ligaments, and periosteum to calcified bone cortex.* Journal of Histochemistry & Cytochemistry, 1991. **39**(1): p. 59-69.
51. Hjorten, R., et al., *Type XXVII collagen at the transition of cartilage to bone during skeletogenesis.* Bone, 2007. **41**(4): p. 535-542.
52. Weiner, S. and L. Addadi, *Crystallization Pathways in Biomineralization.* Annual Review of Materials Research, 2011. **41**(1): p. 21-40.
53. Reznikov, N., et al., *A materials science vision of extracellular matrix mineralization.* Nature Reviews Materials, 2016. **1**(8).
54. Glimcher, M., *Recent studies of the mineral phase in bone and its possible linkage to the organic matrix by protein-bound phosphate bonds.* Philosophical Transactions of the Royal Society of London. B, Biological Sciences, 1984. **304**(1121): p. 479-508.
55. Omelon, S., et al., *A review of phosphate mineral nucleation in biology and geobiology.* Calcified tissue international, 2013. **93**(4): p. 382-396.
56. Mahamid, J., et al., *Mapping amorphous calcium phosphate transformation into crystalline mineral from the cell to the bone in zebrafish fin rays.* Proc Natl Acad Sci U S A, 2010. **107**(14): p. 6316-21.
57. Wang, Y., et al., *Water-mediated structuring of bone apatite.* Nature materials, 2013. **12**(12): p. 1144-1153.
58. Rey, C., et al., *Bone mineral: update on chemical composition and structure.* Osteoporosis International, 2009. **20**(6): p. 1013-1021.
59. Glimcher, M.J., *Bone: nature of the calcium phosphate crystals and cellular, structural, and physical chemical mechanisms in their formation.* Reviews in mineralogy and geochemistry, 2006. **64**(1): p. 223-282.
60. Rey, C., et al., *The carbonate environment in bone mineral: a resolution-enhanced Fourier transform infrared spectroscopy study.* Calcified tissue international, 1989. **45**(3): p. 157-164.
61. LeGeros, R.Z., *Calcium phosphates in oral biology and medicine.* Monographs in oral sciences, 1991. **15**: p. 109-111.
62. Redey, S.A., et al., *Behavior of human osteoblastic cells on stoichiometric hydroxyapatite and type A carbonate apatite: role of surface energy.* Journal of Biomedical Materials Research: An Official Journal of The Society for Biomaterials, The Japanese Society for Biomaterials, and The Australian Society for Biomaterials and the Korean Society for Biomaterials, 2000. **50**(3): p. 353-364.
63. Penel, G., et al., *MicroRaman spectral study of the PO 4 and CO 3 vibrational modes in synthetic and biological apatites.* Calcified tissue international, 1998. **63**(6): p. 475-481.
64. Rey, C. and C. Combes, *Physical chemistry of biological apatites*, in *Biomineralization and Biomaterials*. 2016, Elsevier. p. 95-127.
65. Pasteris, J.D., et al., *Lack of OH in nanocrystalline apatite as a function of degree of atomic order: implications for bone and biomaterials.* Biomaterials, 2004. **25**(2): p. 229-238.

66. Rey, C., et al., *Fourier transform infrared spectroscopic study of the carbonate ions in bone mineral during aging.* Calcified tissue international, 1991. **49**(4): p. 251-258.
67. Pemmer, B., et al., *Spatial distribution of the trace elements zinc, strontium and lead in human bone tissue.* Bone, 2013. **57**(1): p. 184-193.
68. Blumenthal, N., F. Betts, and A. Posner, *Stabilization of amorphous calcium phosphate by Mg and ATP.* Calcified tissue research, 1977. **23**(1): p. 245-250.
69. Roschger, A., et al., *Newly formed and remodeled human bone exhibits differences in the mineralization process.* Acta Biomater, 2020.
70. Boivin, G. and P.J. Meunier, *Fluoride and Bone*, in *Therapeutic uses of trace elements*. 1996, Springer. p. 283-295.
71. Li, C., et al., *Strontium is incorporated into mineral crystals only in newly formed bone during strontium ranelate treatment.* Journal of Bone and Mineral Research, 2010. **25**(5): p. 968-975.
72. Weinkamer, R., P. Kollmannsberger, and P. Fratzl, *Towards a Connectomic Description of the Osteocyte Lacunocanalicular Network in Bone.* Curr Osteoporos Rep, 2019. **17**(4): p. 186-194.
73. Roschger, A., et al., *The contribution of the pericanalicular matrix to mineral content in human osteonal bone.* Bone, 2019. **123**: p. 76-85.
74. Teti, A. and A. Zallone, *Do osteocytes contribute to bone mineral homeostasis? Osteocytic osteolysis revisited.* Bone, 2009. **44**(1): p. 11-6.
75. van Tol, A.F., et al., *Network architecture strongly influences the fluid flow pattern through the lacunocanalicular network in human osteons.* Biomech Model Mechanobiol, 2019.
76. Verborgt, O., et al., *Spatial distribution of Bax and Bcl-2 in osteocytes after bone fatigue: complementary roles in bone remodeling regulation?* Journal of bone and mineral research, 2002. **17**(5): p. 907-914.
77. Raheja, L.F., D.C. Genetos, and C.E. Yellowley, *Hypoxic osteocytes recruit human MSCs through an OPN/CD44-mediated pathway.* Biochemical and biophysical research communications, 2008. **366**(4): p. 1061-1066.
78. Wysolmerski, J.J., *Osteocytic osteolysis: time for a second look?* Bonekey Rep, 2012. **1**: p. 229.
79. Liu, Y., D. Luo, and T. Wang, *Hierarchical Structures of Bone and Bioinspired Bone Tissue Engineering.* Small, 2016. **12**(34): p. 4611-32.
80. Gorski, J.P., *Biomineralization of bone: a fresh view of the roles of non-collagenous proteins.* Frontiers in bioscience (Landmark edition), 2011. **16**: p. 2598.
81. Kjellén, L. and U. Lindahl, *Proteoglycans: structures and interactions.* Annual review of biochemistry, 1991. **60**(1): p. 443-475.
82. Lamoureux, F., et al., *Proteoglycans: key partners in bone cell biology.* Bioessays, 2007. **29**(8): p. 758-71.
83. Thompson, W.R., et al., *Perlecan/Hspg2 deficiency alters the pericellular space of the lacunocanalicular system surrounding osteocytic processes in cortical bone.* J Bone Miner Res, 2011. **26**(3): p. 618-29.
84. Ozawa, H., K. Hoshi, and N. Amizuka, *Current Concepts of Bone Biomineralization.* Journal of Oral Biosciences, 2008. **50**(1): p. 1-14.
85. Ruffoni, D., et al., *The bone mineralization density distribution as a fingerprint of the mineralization process.* Bone, 2007. **40**(5): p. 1308-19.
86. Martin, B., *Mathematical model for the mineralization of bone.* Journal of orthopaedic research, 1994. **12**(3): p. 375-383.
87. Veis, A. and J.R. Dorvee, *Biomineralization mechanisms: a new paradigm for crystal nucleation in organic matrices.* Calcif Tissue Int, 2013. **93**(4): p. 307-15.
88. Kirsch, T., *Biomineralization--an active or passive process?* Connect Tissue Res, 2012. **53**(6): p. 438-45.

89. Mann, S., *Mineralization in biological systems*, in *Inorganic elements in biochemistry*. 1983, Springer. p. 125-174.
90. Olszta, M.J., et al., *Bone structure and formation: A new perspective.* Materials Science and Engineering: R: Reports, 2007. **58**(3-5): p. 77-116.
91. Beniash, E., et al., *Transient amorphous calcium phosphate in forming enamel.* J Struct Biol, 2009. **166**(2): p. 133-43.
92. Brown, W.E., *Octacalcium phosphate and hydroxyapatite.* Nature, 1962. **196**: p. 1048-1411.
93. Brown, W., N. Eidelman, and B. Tomazic, *Octacalcium phosphate as a precursor in biomineral formation.* Advances in dental research, 1987. **1**(2): p. 306-313.
94. Grynpas, M.D. and S. Omelon, *Transient precursor strategy or very small biological apatite crystals?* Bone, 2007. **41**(2): p. 162-4.
95. Rodriguez, D.E., et al., *Multifunctional role of osteopontin in directing intrafibrillar mineralization of collagen and activation of osteoclasts.* Acta Biomater, 2014. **10**(1): p. 494-507.
96. Colfen, H., *Biomineralization: A crystal-clear view.* Nat Mater, 2010. **9**(12): p. 960-1.
97. Dey, A., et al., *The role of prenucleation clusters in surface-induced calcium phosphate crystallization.* Nat Mater, 2010. **9**(12): p. 1010-4.
98. Silver, F.H. and W.J. Landis, *Deposition of apatite in mineralizing vertebrate extracellular matrices: A model of possible nucleation sites on type I collagen.* Connect Tissue Res, 2011. **52**(3): p. 242-54.
99. Akiva, A., et al., *Intercellular pathways from the vasculature to the forming bone in the zebrafish larval caudal fin: Possible role in bone formation.* J Struct Biol, 2019. **206**(2): p. 139-148.
100. Sanders, D., C. Brownlee, and J.F. Harper, *Communicating with calcium.* The Plant Cell, 1999. **11**(4): p. 691-706.
101. Voet, D., J.G. Voet, and C.W. Pratt, *Fundamentals of biochemistry: life at the molecular level*. 2016: John Wiley & Sons.
102. Golub, E.E., *Biomineralization and matrix vesicles in biology and pathology.* Semin Immunopathol, 2011. **33**(5): p. 409-17.
103. Kerschnitzki, M., et al., *Transport of membrane-bound mineral particles in blood vessels during chicken embryonic bone development.* Bone, 2016. **83**: p. 65-72.
104. Lehninger, A.L., *Mitochondria and calcium ion transport.* Biochemical Journal, 1970. **119**(2): p. 129.
105. Rohde, M. and H. Mayer, *Exocytotic process as a novel model for mineralization by osteoblasts in vitro and in vivo determined by electron microscopic analysis.* Calcif Tissue Int, 2007. **80**(5): p. 323-36.
106. Golub, E.E., *Role of matrix vesicles in biomineralization.* Biochim Biophys Acta, 2009. **1790**(12): p. 1592-8.
107. Landis, W.J. and A.L. Arsenault, *Vesicle- and collagen-mediated calcification in the turkey leg tendon.* Connect Tissue Res, 1989. **22**(1-4): p. 35-42; discussion 53-61.
108. Holt, C., et al., *Mineralisation of soft and hard tissues and the stability of biofluids.* J Struct Biol, 2014. **185**(3): p. 383-96.
109. Martin, D.L. and H.F. Deluca, *Calcium transport and the role of vitamin D.* Archives of biochemistry and biophysics, 1969. **134**(1): p. 139-148.
110. Traub, W., et al., *Dentin Phosphophoryn Binding to Collagen Fibrils.* Matrix, 1992. **12**(3): p. 197-201.
111. Landis, W.J., J. Moradian-oldak, and S. Weiner, *Topographic imaging of mineral and collagen in the calcifying turkey tendon.* Connective tissue research, 1991. **25**(3-4): p. 181-196.

112. Landis, W.J. and M.J. Song, *Early mineral deposition in calcifying tendon characterized by high voltage electron microscopy and three-dimensional graphic imaging.* Journal of structural biology, 1991. **107**(2): p. 116-127.
113. Price, P.A., D. Toroian, and J.E. Lim, *Mineralization by inhibitor exclusion: the calcification of collagen with fetuin.* J Biol Chem, 2009. **284**(25): p. 17092-101.
114. Nudelman, F., et al., *The role of collagen in bone apatite formation in the presence of hydroxyapatite nucleation inhibitors.* Nat Mater, 2010. **9**(12): p. 1004-9.
115. Hasegawa, T., et al., *Sclerostin is differently immunolocalized in metaphyseal trabecules and cortical bones of mouse tibiae.* Biomedical Research, 2013. **34**(3): p. 153-159.
116. Ganss, B., R.H. Kim, and J. Sodek, *Bone sialoprotein.* Critical Reviews in Oral Biology & Medicine, 1999. **10**(1): p. 79-98.
117. George, A. and A. Veis, *Phosphorylated proteins and control over apatite nucleation, crystal growth, and inhibition.* Chemical reviews, 2008. **108**(11): p. 4670-4693.
118. Morinobu, M., et al., *Osteopontin expression in osteoblasts and osteocytes during bone formation under mechanical stress in the calvarial suture in vivo.* Journal of Bone and Mineral Research, 2003. **18**(9): p. 1706-1715.
119. Chen, L., et al., *Refinement of collagen-mineral interaction: a possible role for osteocalcin in apatite crystal nucleation, growth and development.* Bone, 2015. **71**: p. 7-16.
120. Murshed, M., et al., *Extracellular matrix mineralization is regulated locally; different roles of two gla-containing proteins.* J Cell Biol, 2004. **165**(5): p. 625-30.
121. Heiss, A., et al., *Structural basis of calcification inhibition by alpha 2-HS glycoprotein/fetuin-A. Formation of colloidal calciprotein particles.* J Biol Chem, 2003. **278**(15): p. 13333-41.
122. Holt, C., E.S. Sorensen, and R.A. Clegg, *Role of calcium phosphate nanoclusters in the control of calcification.* FEBS J, 2009. **276**(8): p. 2308-23.
123. Addison, W.N., et al., *Pyrophosphate inhibits mineralization of osteoblast cultures by binding to mineral, up-regulating osteopontin, and inhibiting alkaline phosphatase activity.* Journal of Biological Chemistry, 2007. **282**(21): p. 15872-15883.
124. Orriss, I.R., T.R. Arnett, and R.G.G. Russell, *Pyrophosphate: a key inhibitor of mineralisation.* Current opinion in pharmacology, 2016. **28**: p. 57-68.
125. Bisaz, S., R. Russell, and H. Fleisch, *Isolation of inorganic pyrophosphate from bovine and human teeth.* Archives of oral biology, 1968. **13**(6): p. 683-696.
126. Graff, R.D., et al., *ATP release by mechanically loaded porcine chondrons in pellet culture.* Arthritis & Rheumatism: Official Journal of the American College of Rheumatology, 2000. **43**(7): p. 1571-1579.
127. Mikuni-Takagaki, Y., et al., *Matrix mineralization and the differentiation of osteocyte-like cells in culture.* Journal of Bone and Mineral Research, 1995. **10**(2): p. 231-242.
128. Palumbo, C., *A three-dimensional ultrastructural study of osteoid-osteocytes in the tibia of chick embryos.* Cell and tissue research, 1986. **246**(1): p. 125-131.
129. Kerschnitzki, M., et al., *Architecture of the osteocyte network correlates with bone material quality.* J Bone Miner Res, 2013. **28**(8): p. 1837-45.
130. Zhang, S., et al., *Nanostructure and mechanical properties of the osteocyte lacunar-canalicular network-associated bone matrix revealed by quantitative nanomechanical mapping.* Nano Research, 2015. **8**(10): p. 3250-3260.
131. Qing, H., et al., *Demonstration of osteocytic perilacunar/canalicular remodeling in mice during lactation.* J Bone Miner Res, 2012. **27**(5): p. 1018-29.
132. Boukpessi, T., et al., *Osteopontin and the dento-osseous pathobiology of X-linked hypophosphatemia.* Bone, 2017. **95**: p. 151-161.

133. Cheung, M., et al., *Cortical and trabecular bone density in X-linked hypophosphatemic rickets.* J Clin Endocrinol Metab, 2013. **98**(5): p. E954-61.
134. Kollmannsberger, P., et al., *The small world of osteocytes: connectomics of the lacuno-canalicular network in bone.* New Journal of Physics, 2017. **19**(7).
135. Goggin, P., et al., *Development of protocols for the first serial block-face scanning electron microscopy (SBF SEM) studies of bone tissue.* Bone, 2020. **131**: p. 115107.
136. Blouin, S., et al., *Confocal laser scanning microscopy-a powerful tool in bone research.* Wien Med Wochenschr, 2018. **168**(11-12): p. 314-321.
137. Gianuzzi, L.A. and F.A. Stevie, *Introduction to focused ion beams.* Instrumentation, Theory, Techniques and Practice: Springer, 2005.
138. Reyntjens, S. and R. Puers, *A review of focused ion beam applications in microsystem technology.* Journal of micromechanics and microengineering, 2001. **11**(4): p. 287.
139. Schneider, P., et al., *Towards quantitative 3D imaging of the osteocyte lacuno-canalicular network.* Bone, 2010. **47**(5): p. 848-58.
140. Reimer, L., *Scanning electron microscopy: physics of image formation and microanalysis*. Vol. 45. 2013: Springer.
141. Goldstein, J.I., et al., *Scanning electron microscopy and X-ray microanalysis*. 2017: Springer.
142. Wanner, A., M. Kirschmann, and C. Genoud, *Challenges of microtome-based serial block-face scanning electron microscopy in neuroscience.* Journal of microscopy, 2015. **259**(2): p. 137-142.
143. Eisenstein, M., *Putting neurons on the map.* Nature, 2009. **461**(7267): p. 1150-1152.
144. Jerome, W.G. and R.L. Price, *Basic confocal microscopy*. 2018: Springer.
145. Pawley, J., *Handbook of biological confocal microscopy*. 2010: Springer Science & Business Media.
146. Orhan, K., *Micro-computed Tomography (micro-CT) in Medicine and Engineering*. 2019, Springer.
147. Pacureanu, A., et al., *Nanoscale imaging of the bone cell network with synchrotron X-ray tomography: optimization of acquisition setup.* Med Phys, 2012. **39**(4): p. 2229-38.
148. Schneider, P., et al., *Serial FIB/SEM imaging for quantitative 3D assessment of the osteocyte lacuno-canalicular network.* Bone, 2011. **49**(2): p. 304-11.
149. Deguchi, T., et al. *Tomographic STED microscopy to study bone resorption*. in *Three-Dimensional and Multidimensional Microscopy: Image Acquisition and Processing XXII*. 2015. International Society for Optics and Photonics.
150. Wu, Y., et al., *Resonant Scanning with Large Field of View Reduces Photobleaching and Enhances Fluorescence Yield in STED Microscopy.* Sci Rep, 2015. **5**: p. 14766.
151. Langer, M., et al., *X-ray phase nanotomography resolves the 3D human bone ultrastructure.* PLoS One, 2012. **7**(8): p. e35691.
152. Arabi, H., A. KAMALIASL, and S. Aghamiri, *The effect of focal spot size on the spatial resolution of variable resolution X-ray CT scanner.* 2010.
153. Akiva, A., et al., *On the pathway of mineral deposition in larval zebrafish caudal fin bone.* Bone, 2015. **75**: p. 192-200.
154. De Bruijn, J., et al., *The ultrastructure of the bone-hydroxyapatite interface in vitro.* Journal of biomedical materials research, 1992. **26**(10): p. 1365-1382.
155. Boyde, A., et al., *Iodine vapor staining for atomic number contrast in backscattered electron and X-ray imaging.* Microsc Res Tech, 2014. **77**(12): p. 1044-51.
156. Bartl, R. and C. Bartl, *The Osteoporosis Manual: Prevention, Diagnosis and Management*. 2019: Springer.
157. Scimeca, M., et al., *Energy Dispersive X-ray (EDX) microanalysis: A powerful tool in biomedical research and diagnosis.* Eur J Histochem, 2018. **62**(1): p. 2841.
158. Thompson, A.C. and D. Vaughan, *X-ray data booklet*. Vol. 8. 2001: Lawrence Berkeley National Laboratory, University of California Berkeley, CA.

159. Stephensen, H.J.T., S. Darkner, and J. Sporring, *A Highly Accurate Model Based Registration Method for FIB-SEM Images of Neurons.* arXiv preprint arXiv:1810.01159, 2018.
160. Fehrenbach, J., P. Weiss, and C. Lorenzo, *Variational algorithms to remove stationary noise: applications to microscopy imaging.* IEEE Trans Image Process, 2012. **21**(10): p. 4420-30.
161. Roels, J., et al. *Noise analysis and removal in 3D electron microscopy*. in *International Symposium on Visual Computing*. 2014. Springer.
162. Chambolle, A., *An algorithm for total variation minimization and applications.* Journal of Mathematical imaging and vision, 2004. **20**(1-2): p. 89-97.
163. Srinivasan, R., M. Cannon, and J. White, *Landsat data destriping using power spectral filtering.* Optical Engineering, 1988. **27**(11): p. 271193.
164. Münch, B., et al., *Stripe and ring artifact removal with combined wavelet—Fourier filtering.* Optics express, 2009. **17**(10): p. 8567-8591.
165. Torres, J. and J. Favela. *Satellite image destriping: a wavelet-based approach*. in *Image Reconstruction and Restoration II*. 1997. International Society for Optics and Photonics.
166. Torelli, J.C., et al., *A High Performance 3d Exact Euclidean Distance Transform Algorithm for Distributed Computing.* International Journal of Pattern Recognition and Artificial Intelligence, 2011. **24**(06): p. 897-915.
167. Howell, P., K. Davy, and A. Boyde, *Mean atomic number and backscattered electron coefficient calculations for some materials with low mean atomic number.* Scanning: The Journal of Scanning Microscopies, 1998. **20**(1): p. 35-40.
168. Boyde, A., *Staining plastic blocks with triiodide to image cells and soft tissues in backscattered electron SEM of skeletal and dental tissues.* Eur Cell Mater, 2012. **24**: p. 154-60; discussion 160-1.
169. Gay, C. and H. Schraer, *Frozen thin-sections of rapidly forming bone: bone cell ultrastructure.* Calcified tissue research, 1975. **19**(1): p. 39-49.
170. Degenhardt, K., et al., *Rapid 3D phenotyping of cardiovascular development in mouse embryos by micro-CT with iodine staining.* Circ Cardiovasc Imaging, 2010. **3**(3): p. 314-22.
171. Jeffery, N.S., et al., *Micro-computed tomography with iodine staining resolves the arrangement of muscle fibres.* Journal of biomechanics, 2011. **44**(1): p. 189-192.
172. Vickerton, P., J. Jarvis, and N. Jeffery, *Concentration-dependent specimen shrinkage in iodine-enhanced microCT.* J Anat, 2013. **223**(2): p. 185-93.
173. Lower, S., *Chem1 virtual textbook*. 1999, Burnaby, Vancouver: Retrieved from http://www. chem1. com/acad/webtext ….
174. Gaskell, D.R. and D.E. Laughlin, *Introduction to the Thermodynamics of Materials*. 2017: CRC press.
175. Baxter, G.P., C.H. Hickey, and W.C. Holmes, *THE VAPOR PRESSURE OF IODINE.* Journal of the American Chemical Society, 1907. **29**(2): p. 127-136.
176. Wall, P., *Spray Reagents.* Chromatography: Thin-Layer (Planar)/Spray Reagents, 2000: p. 907-915.
177. Bachmann, L., et al., *Changes in chemical composition and collagen structure of dentine tissue after erbium laser irradiation.* Spectrochimica Acta Part A: Molecular and Biomolecular Spectroscopy, 2005. **61**(11-12): p. 2634-2639.
178. Murray, L.W., et al., *Crosslinking of extracellular matrix proteins: a preliminary report on a possible mechanism of argon laser welding.* Lasers in surgery and medicine, 1989. **9**(5): p. 490-496.
179. Soret, M., S.L. Bacharach, and I. Buvat, *Partial-volume effect in PET tumor imaging.* J Nucl Med, 2007. **48**(6): p. 932-45.
180. Marenzana, M. and T.R. Arnett, *The Key Role of the Blood Supply to Bone.* Bone Res, 2013. **1**(3): p. 203-15.
181. Schenk, R., E. Hunziker, and W. Herrmann, *Structural properties of cells related to tissue mineralization*, in *Biological Mineralization and Demineralization*. 1982, Springer. p. 143-160.

182. Christoffersen, J. and W. Landis, *A contribution with review to the description of mineralization of bone and other calcified tissues in vivo.* The Anatomical Record, 1991. **230**(4): p. 435-450.
183. Neuman, M.W., *Blood: bone equilibrium.* Calcif Tissue Int, 1982. **34**: p. 117-120.
184. Roberts, W.E. and C.M. Stanford, *Bone Physiology, Metabolism, and Biomechanics in Implant Therapy.* Principles and Practice of Single Implant and Restoration, 2013: p. 53.
185. Martin, R., *Does osteocyte formation cause the nonlinear refilling of osteons?* Bone, 2000. **26**(1): p. 71-78.
186. Metz, L.N., R.B. Martin, and A.S. Turner, *Histomorphometric analysis of the effects of osteocyte density on osteonal morphology and remodeling.* Bone, 2003. **33**(5): p. 753-759.
187. Villanueva, A., et al., *Identification of the mineralization front: Comparison of a modified toluldine blue stain with tetracycline fluorescence.* Metabolic Bone Disease and Related Research, 1983. **5**(1): p. 41-45.
188. Bordier, P.J., et al., *Lack of histological evidence of vitamin D abnormality in the bones of anephric patients.* Clinical Science and Molecular Medicine, 1973. **44**(1): p. 33-41.
189. Murray, J., *Mathematical biology. I An introduction, Interdisciplinary Applied Mathematics, 17 Springer Verlag, New York, 2002.* Mathematical Biology. II Spatial models and biomedical applications Third edition. Interdisciplinary Applied Mathematics. **18**.
190. Tsuji, K. and S.C. Müller, *Spirals and Vortices*. 2019: Springer.
191. Liesegang, R., *Ueber einige eigenschaften von gallerten.* Naturwissenschaftliche Wochenschrift, 1896. **10**(30): p. 353-362.
192. Ostwald, W., *A-Linieu von RE liesegang.* Z. phys. Chem., 1897. **27**: p. 265.
193. Stern, K.H., *The Liesegang Phenomenon.* Chemical Reviews, 1954. **54**(1): p. 79-99.
194. Tuur, S.M., et al., *Liesegang rings in tissue. How to distinguish Liesegang rings from the giant kidney worm, Dioctophyma renale.* The American journal of surgical pathology, 1987. **11**(8): p. 598-605.
195. Henisch, H.K., *Crystal growth in gels*. 1996: Courier Corporation.
196. Kemp, N.E. and S.K. Westrin, *Ultrastructure of calcified cartilage in the endoskeletal tesserae of sharks.* Journal of Morphology, 1979. **160**(1): p. 75-101.
197. Slootweg, P.J., *Dental and Oral Pathology*. 2016: Springer Reference.
198. Bianco, P., et al., *Localization of bone sialoprotein (BSP) to Golgi and post-Golgi secretory structures in osteoblasts and to discrete sites in early bone matrix.* Journal of Histochemistry & Cytochemistry, 1993. **41**(2): p. 193-203.
199. Zou, Z., et al., *Three-dimensional Structural Interrelations between Cells, Extracellular Matrix and Mineral in Vertebrate Mineralization.* BioRxiv, 2019: p. 803007.
200. Reznikov, N., R. Shahar, and S. Weiner, *Three-dimensional structure of human lamellar bone: the presence of two different materials and new insights into the hierarchical organization.* Bone, 2014. **59**: p. 93-104.
201. Piekarski, K. and M. Munro, *Transport mechanism operating between blood supply and osteocytes in long bones.* Nature, 1977. **269**(5623): p. 80.
202. Fritton, S.P. and S. Weinbaum, *Fluid and Solute Transport in Bone: Flow-Induced Mechanotransduction.* Annu Rev Fluid Mech, 2009. **41**: p. 347-374.
203. Price, C., et al., *Real-time measurement of solute transport within the lacunar-canalicular system of mechanically loaded bone: direct evidence for load-induced fluid flow.* J Bone Miner Res, 2011. **26**(2): p. 277-85.
204. McKee, M., et al., *Developmental appearance and ultrastructural immunolocalization of a major 66 kDa phosphoprotein in embryonic and post-natal chicken bone.* The Anatomical Record, 1990. **228**(1): p. 77-92.

205. Atkins, A., et al., *Remodeling in bone without osteocytes: billfish challenge bone structure-function paradigms.* Proc Natl Acad Sci U S A, 2014. **111**(45): p. 16047-52.
206. Ofer, L., et al., *New insights into the process of osteogenesis of anosteocytic bone.* Bone, 2019. **125**: p. 61-73.
207. Shahar, R. and S. Weiner, *Open questions on the 3D structures of collagen containing vertebrate mineralized tissues: A perspective.* Journal of structural biology, 2018. **201**(3): p. 187-198.